

DarkSide-20k Intermediate Design Report

C. E. Aalseth,¹ S. Abdelhakim,² F. Acerbi,^{3,4} P. Agnes,⁵ I. F. M. Albuquerque,⁶
 T. Alexander,¹ A. Alici,^{7,8} A. K. Alton,⁹ P. Amaudruz,¹⁰ F. Ameli,¹¹ P. Antonioli,⁸
 S. Arcelli,^{7,8} R. Ardito,^{12,13} I. J. Arnquist,¹ P. Arpaia,^{14,15} D. M. Asner,¹⁶ A. Asunskis,¹⁷
 M. Ave,⁶ H. O. Back,¹ A. Barrado Olmedo,¹⁸ G. Batignani,^{19,20} M. G. Bisogni,^{19,20} V. Bocci,¹¹
 A. Bondar,^{21,22} G. Bonfini,²³ W. Bonivento,²⁴ B. Bottino,^{25,26} M. G. Boulay,²⁷ R. Bunker,¹
 S. Bussino,^{28,29} A. Buzulutskov,^{21,22} M. Cadeddu,^{30,24} M. Cadoni,^{30,24} A. Caminata,²⁶
 N. Canci,^{5,23} A. Candela,²³ C. Cantini,³¹ M. Caravati,²⁴ M. Cariello,²⁶ M. Carpinelli,^{32,33}
 A. Castellani,^{12,13} P. Castello,^{34,24} S. Catalanotti,^{35,15} V. Cataudella,^{35,15} P. Cavalcante,^{36,23}
 S. Cavuoti,^{35,15} S. Cebrian,³⁷ B. Celano,¹⁵ R. Cereseto,²⁶ W. Cheng,^{38,39} A. Chepurnov,⁴⁰
 C. Ciccalò,²⁴ L. Cifarelli,^{7,8} M. Citterio,¹³ A. G. Cocco,¹⁵ M. Colocci,^{7,8} L. Consiglio,⁴¹
 F. Cossio,^{38,39} G. Covone,^{35,15} P. Crivelli,³¹ I. D'Antone,⁸ M. D'Incecco,²³ D. D'Urso,^{32,33}
 M. D. Da Rocha Rolo,³⁸ M. Daniel,¹⁸ S. Davini,²⁶ A. De Candia,^{35,15} S. De Cecco,^{11,42}
 M. De Deo,²³ A. De Falco,^{24,30} G. De Filippis,^{35,15} D. De Gruttola,⁴³ G. De Guido,^{44,13}
 G. De Rosa,^{35,15} G. Dellacasa,³⁸ P. Demontis,^{32,33,45} S. DePaquale,⁴³ A. V. Derbin,⁴⁶
 A. Devoto,^{30,24} F. Di Eusanio,^{47,23} G. Di Pietro,^{23,13} P. Di Stefano,⁴⁸ C. Dionisi,^{11,42}
 F. Dordei,²⁴ M. Downing,⁴⁹ F. Edalatfar,¹⁰ A. Empl,⁵ M. Fernandez Diaz,¹⁸ A. Ferri,^{3,4}
 C. Filip,⁵⁰ G. Fiorillo,^{35,15} K. Fomenko,⁵¹ A. Franceschi,⁵² D. Franco,⁵³ G. E. Froudakis,⁵⁴
 F. Gabriele,²³ A. Gabrieli,^{32,33} C. Galbiati,^{47,41} P. Garcia Abia,¹⁸ D. Gascón Fora,⁵⁵
 A. Gendotti,³¹ C. Ghiano,²³ A. Ghisi,^{12,13} S. Giagu,^{11,42} P. Giampa,¹⁰ R. A. Giampaolo,³⁸
 C. Giganti,⁵⁶ M. A. Giorgi,^{20,19} G. K. Giovanetti,⁴⁷ M. L. Gligan,⁵⁰ A. Gola,^{3,4} O. Gorchakov,⁵¹
 M. Grab,⁵⁷ R. Graciani Diaz,⁵⁵ F. Granato,⁵⁸ M. Grassi,¹⁹ J. W. Grate,¹ G. Y. Grigoriev,⁵⁹
 A. Grobov,⁵⁹ M. Gromov,⁴⁰ M. Guan,⁶⁰ M. B. B. Guerra,¹⁷ M. Guerzoni,⁸ M. Gulino,^{61,33}
 R. K. Haaland,⁶² B. R. Hackett,⁶³ A. Hallin,⁶⁴ B. Harrop,⁴⁷ E. W. Hoppe,¹ S. Horikawa,^{41,23}
 B. Hosseini,²⁴ F. Hubaut,⁶⁵ P. Humble,¹ E. V. Hungerford,⁵ An. Ianni,^{47,23} V. Ippolito,¹¹
 C. Jillings,^{66,67} S. Jimenez Cabre,¹⁸ K. Keeter,¹⁷ C. L. Kendziora,⁶⁸ S. Kim,⁵⁸ I. Kochanek,²³
 K. Kondo,⁴¹ G. Kopp,⁴⁷ D. Korablev,⁵¹ G. Korga,^{5,23} A. Kubankin,⁶⁹ R. Kugathasan,^{38,39}
 M. Kuss,¹⁹ M. Kuzniak,²⁷ M. La Commara,^{70,15} M. Lai,^{30,24} S. Langrock,^{66,67} M. Lebois,²
 B. Lehnert,⁶⁴ X. Li,⁴⁷ Q. Liqiang,² M. Lissia,²⁴ G. U. Lodi,^{44,13} G. Longo,^{35,15} R. Lussana,^{71,13}
 L. Luzzi,^{72,13} A. A. Machado,⁷³ I. N. Machulin,^{59,74} A. Mandarano,^{41,23} L. Mapelli,⁴⁷
 M. Marcante,^{75,4,3} A. Margotti,⁸ S. M. Mari,^{28,29} M. Mariani,^{72,13} J. Maricic,⁶³ M. Marinelli,^{25,26}
 D. Marras,²⁴ A. D. Martinez Rojas,^{38,39} C. J. Martoff,⁵⁸ M. Mascia,^{76,24} A. Masoni,²⁴
 A. Mazzi,^{3,4} A. B. McDonald,⁴⁸ A. Messina,^{11,42} P. D. Meyers,⁴⁷ T. Miletic,⁶³ R. Milincic,⁶³
 A. Moggi,¹⁹ S. Moioli,^{44,13} J. Monroe,⁷⁷ M. Morrocchi,¹⁹ T. Mroz,⁵⁷ W. Mu,³¹ V. N. Muratova,⁴⁶
 S. Murphy,³¹ C. Muscas,^{34,24} P. Musico,²⁶ R. Nania,⁸ T. Napolitano,⁵² A. Navrer Agasson,⁵⁶
 M. Nessi,⁷⁸ I. Nikulin,⁶⁹ A. O. Nozdrina,^{59,74} N. N. Nurakhov,⁵⁹ A. Oleinik,⁶⁹ V. Oleynikov,^{21,22}
 M. Orsini,²³ F. Ortica,^{79,80} L. Pagani,⁸¹ M. Pallavicini,^{25,26} S. Palmas,^{76,24} L. Pandola,³³
 E. Pantic,⁸¹ E. Paoloni,^{19,20} G. Paternoster,^{3,4} V. Pavletcov,⁴⁰ F. Pazzona,^{32,33} S. Peeters,⁸²
 P. A. Pegoraro,^{34,24} K. Pelczar,²³ L. A. Pellegrini,^{44,13} N. Pelliccia,^{79,80} F. Perotti,^{12,13}
 V. Pesudo,¹⁸ E. Picciau,^{30,24} C. Piemonte,^{3,4} F. Pietropaolo,⁷⁸ A. Pocar,⁴⁹ T. Pollman,⁸³
 D. Portaluppi,^{71,13} S. S. Poudel,⁵ P. Pralavorio,⁶⁵ D. Price,⁸⁴ D. A. Pugachev,⁵⁹ B. Radics,³¹
 F. Raffaelli,¹⁹ F. Ragusa,^{85,13} M. Razeti,²⁴ A. Razeto,²³ V. Regazzoni,^{75,4,3} C. Regenfus,³¹
 A. L. Renshaw,⁵ S. Rescia,¹⁶ M. Rescigno,¹¹ F. Retiere,¹⁰ Q. Riffard,⁵³ A. Rivetti,³⁸
 A. Romani,^{79,80} L. Romero,¹⁸ N. Rossi,^{11,23} A. Rubbia,³¹ D. Sablone,^{58,23} P. Sala,⁷⁸
 P. Salatino,^{86,15} O. Samoylov,⁵¹ E. Sánchez García,¹⁸ S. Sanfilippo,^{29,28} M. Sant,^{32,33}
 D. Santone,⁷⁷ R. Santorelli,¹⁸ C. Savarese,⁴⁷ E. Scapparone,⁸ B. Schlitzer,⁸¹ G. Scioli,^{7,8}
 E. Segreto,⁷³ A. Seifert,¹ D. A. Semenov,⁴⁶ A. Shchagin,⁶⁹ E. Shemyakina,^{21,22} A. Sheshukov,⁵¹
 S. Siddhanta,²⁴ M. Simeone,^{86,15} P. N. Singh,⁵ P. Skensved,⁴⁸ M. D. Skorokhvatov,^{59,74}

- 52 O. Smirnov,⁵¹ G. Sobrero,²⁶ A. Sokolov,^{21,22} A. Sotnikov,⁵¹ R. Stainforth,²⁷ S. Stracka,¹⁹
 53 G. B. Suffritti,^{32,33,45} S. Sulis,^{34,24} Y. Suvorov,^{35,15,59} A.M. Szlc,⁸⁴ R. Tartaglia,²³
 54 G. Testera,²⁶ T. Thorpe,^{41,23} A. Tonazzo,⁵³ A. Tosi,^{71,13} E. V. Unzhakov,⁴⁶ G. Usai,^{24,30}
 55 A. Vacca,^{76,24} E. Vázquez-Jáuregui,⁸⁷ M. Verducci,^{11,42} T. Viant,³¹ S. Viel,²⁷
 56 F. Villa,^{71,13} A. Vishneva,⁵¹ R. B. Vogelaar,³⁶ M. Wada,²⁴ J. Wahl,¹ J. J. Walding,⁷⁷
 57 H. Wang,⁸⁸ Y. Wang,⁸⁸ S. Westerdale,²⁷ R. J. Wheadon,³⁸ R. Williams,¹ J. Wilson,²
 58 Marcin Wojcik,⁵⁷ Mariusz Wojcik,⁸⁹ S. Wu,³¹ X. Xiao,⁸⁸ C. Yang,⁶⁰ Z. Ye,⁵ and G. Zuzel⁵⁷
 59
 60 ¹Pacific Northwest National Laboratory, Richland, WA 99352, USA
 61 ²Institut de Physique Nucléaire d'Orsay, 91406, Orsay, France
 62 ³Fondazione Bruno Kessler, Povo 38123, Italy
 63 ⁴Trento Institute for Fundamental Physics and Applications, Povo 38123, Italy
 64 ⁵Department of Physics, University of Houston, Houston, TX 77204, USA
 65 ⁶Instituto de Física, Universidade de São Paulo, São Paulo 05508-090, Brazil
 66 ⁷Physics Department, Università degli Studi di Bologna, Bologna 40126, Italy
 67 ⁸INFN Bologna, Bologna 40126, Italy
 68 ⁹Physics Department, Augustana University, Sioux Falls, SD 57197, USA
 69 ¹⁰TRIUMF, 4004 Wesbrook Mall, Vancouver, BC V6T 2A3, Canada
 70 ¹¹INFN Sezione di Roma, Roma 00185, Italy
 71 ¹²Civil and Environmental Engineering Department, Politecnico di Milano, Milano 20133, Italy
 72 ¹³INFN Milano, Milano 20133, Italy
 73 ¹⁴Department of Electrical Engineering and Information Technology,
 74 Università degli Studi "Federico II" di Napoli, Napoli 80125, Italy
 75 ¹⁵INFN Napoli, Napoli 80126, Italy
 76 ¹⁶Brookhaven National Laboratory, Upton, NY 11973, USA
 77 ¹⁷School of Natural Sciences, Black Hills State University, Spearfish, SD 57799, USA
 78 ¹⁸CIEMAT, Centro de Investigaciones Energéticas, Medioambientales y Tecnológicas, Madrid 28040, Spain
 79 ¹⁹INFN Pisa, Pisa 56127, Italy
 80 ²⁰Physics Department, Università degli Studi di Pisa, Pisa 56127, Italy
 81 ²¹Budker Institute of Nuclear Physics, Novosibirsk 630090, Russia
 82 ²²Novosibirsk State University, Novosibirsk 630090, Russia
 83 ²³INFN Laboratori Nazionali del Gran Sasso, Assergi (AQ) 67100, Italy
 84 ²⁴INFN Cagliari, Cagliari 09042, Italy
 85 ²⁵Physics Department, Università degli Studi di Genova, Genova 16146, Italy
 86 ²⁶INFN Genova, Genova 16146, Italy
 87 ²⁷Department of Physics, Carleton University, Ottawa, ON K1S 5B6, Canada
 88 ²⁸INFN Roma Tre, Roma 00146, Italy
 89 ²⁹Mathematics and Physics Department, Università degli Studi Roma Tre, Roma 00146, Italy
 90 ³⁰Physics Department, Università degli Studi di Cagliari, Cagliari 09042, Italy
 91 ³¹Institute for Particle Physics, ETH Zürich, Zürich 8093, Switzerland
 92 ³²Chemistry and Pharmacy Department, Università degli Studi di Sassari, Sassari 07100, Italy
 93 ³³INFN Laboratori Nazionali del Sud, Catania 95123, Italy
 94 ³⁴Department of Electrical and Electronic Engineering
 95 Engineering, Università degli Studi, Cagliari 09042, Italy
 96 ³⁵Physics Department, Università degli Studi "Federico II" di Napoli, Napoli 80126, Italy
 97 ³⁶Virginia Tech, Blacksburg, VA 24061, USA
 98 ³⁷Laboratorio de Física Nuclear y Astropartículas, Universidad de Zaragoza, Zaragoza 50009, Spain
 99 ³⁸INFN Torino, Torino 10125, Italy
 100 ³⁹Department of Electronics and Communications, Politecnico di Torino, Torino 10129, Italy
 101 ⁴⁰Skobeltsyn Institute of Nuclear Physics, Lomonosov Moscow State University, Moscow 119234, Russia
 102 ⁴¹Gran Sasso Science Institute, L'Aquila 67100, Italy
 103 ⁴²Physics Department, Sapienza Università di Roma, Roma 00185, Italy
 104 ⁴³INFN Salerno, Salerno 84084, Italy
 105 ⁴⁴Chemistry, Materials and Chemical Engineering Department
 106 "G. Natta", Politecnico di Milano, Milano 20133, Italy
 107 ⁴⁵Interuniversity Consortium for Science and Technology of Materials, Firenze 50121, Italy
 108 ⁴⁶Saint Petersburg Nuclear Physics Institute, Gatchina 188350, Russia
⁴⁷Physics Department, Princeton University, Princeton, NJ 08544, USA

- 109 ⁴⁸*Department of Physics, Engineering Physics and Astronomy,
 110 Queen's University, Kingston, ON K7L 3N6, Canada*
 111 ⁴⁹*Amherst Center for Fundamental Interactions and Physics
 112 Department, University of Massachusetts, Amherst, MA 01003, USA*
 113 ⁵⁰*National Institute for R&D of Isotopic and Molecular Technologies, Cluj-Napoca, 400293, Romania*
 114 ⁵¹*Joint Institute for Nuclear Research, Dubna 141980, Russia*
 115 ⁵²*INFN Laboratori Nazionali di Frascati, Frascati 00044, Italy*
 116 ⁵³*APC, Université Paris Diderot, CNRS/IN2P3, CEA/Irfu, Obs de Paris, USPC, Paris 75205, France*
 117 ⁵⁴*Department of Chemistry, University of Crete, P.O. Box 2208, 71003 Heraklion, Crete, Greece*
 118 ⁵⁵*Universitat de Barcelona, Barcelona E-08028, Catalonia, Spain*
 119 ⁵⁶*LPNHE, CNRS/IN2P3, Sorbonne Université, Université Paris Diderot, Paris 75252, France*
 120 ⁵⁷*M. Smoluchowski Institute of Physics, Jagiellonian University, 30-348 Krakow, Poland*
 121 ⁵⁸*Physics Department, Temple University, Philadelphia, PA 19122, USA*
 122 ⁵⁹*National Research Centre Kurchatov Institute, Moscow 123182, Russia*
 123 ⁶⁰*Institute of High Energy Physics, Beijing 100049, China*
 124 ⁶¹*Engineering and Architecture Faculty, Università di Enna Kore, Enna 94100, Italy*
 125 ⁶²*Department of Physics and Engineering, Fort Lewis College, Durango, CO 81301, USA*
 126 ⁶³*Department of Physics and Astronomy, University of Hawai'i, Honolulu, HI 96822, USA*
 127 ⁶⁴*Department of Physics, University of Alberta, Edmonton, AB T6G 2R3, Canada*
 128 ⁶⁵*Centre de Physique des Particules de Marseille, Aix
 129 Marseille Univ, CNRS/IN2P3, CPPM, Marseille, France*
 130 ⁶⁶*Department of Physics and Astronomy, Laurentian University, Sudbury, ON P3E 2C6, Canada*
 131 ⁶⁷*SNOLAB, Lively, ON P3Y 1N2, Canada*
 132 ⁶⁸*Fermi National Accelerator Laboratory, Batavia, IL 60510, USA*
 133 ⁶⁹*Radiation Physics Laboratory, Belgorod National Research University, Belgorod 308007, Russia*
 134 ⁷⁰*Pharmacy Department, Università degli Studi "Federico II" di Napoli, Napoli 80131, Italy*
 135 ⁷¹*Electronics, Information, and Bioengineering Department, Politecnico di Milano, Milano 20133, Italy*
 136 ⁷²*Energy Department, Politecnico di Milano, Milano 20133, Italy*
 137 ⁷³*Physics Institute, Universidade Estadual de Campinas, Campinas 13083, Brazil*
 138 ⁷⁴*National Research Nuclear University MEPhI, Moscow 115409, Russia*
 139 ⁷⁵*Physics Department, Università degli Studi di Trento, Povo 38123, Italy*
 140 ⁷⁶*Department of Mechanical, Chemical, and Materials
 141 Engineering, Università degli Studi, Cagliari 09042, Italy*
 142 ⁷⁷*Department of Physics, Royal Holloway University of London, Egham TW20 0EX, UK*
 143 ⁷⁸*CERN, European Organization for Nuclear Research 1211 Geneve 23, Switzerland, CERN*
 144 ⁷⁹*Chemistry, Biology and Biotechnology Department, Università degli Studi di Perugia, Perugia 06123, Italy*
 145 ⁸⁰*INFN Perugia, Perugia 06123, Italy*
 146 ⁸¹*Department of Physics, University of California, Davis, CA 95616, USA*
 147 ⁸²*Physics and Astronomy, University of Sussex, Brighton BN1 9QH, UK*
 148 ⁸³*Physik Department, Technische Universität München, Munich 80333, Germany*
 149 ⁸⁴*The University of Manchester, Manchester M13 9PL, United Kingdom*
 150 ⁸⁵*Physics Department, Università degli Studi di Milano, Milano 20133, Italy*
 151 ⁸⁶*Chemical, Materials, and Industrial Production Engineering Department,
 152 Università degli Studi "Federico II" di Napoli, Napoli 80126, Italy*
 153 ⁸⁷*Instituto de Física, Universidad Nacional Autónoma de México (UNAM), México 01000, Mexico*
 154 ⁸⁸*Physics and Astronomy Department, University of California, Los Angeles, CA 90095, USA*
 155 ⁸⁹*Institute of Applied Radiation Chemistry, Lodz University of Technology, 93-590 Lodz, Poland*

CONTENTS

157	List of Figures	v
158	List of Tables	vi
159	Executive Summary	1
160	Physics Case	1
161	DarkSide-20k: The High-Mass Search Program	2
162	DarkSide-LowMass: The Low-Mass Search Program	4
163	Ago	5
164	Comparison with Xenon-Based Experiments and the “Neutrino Floor”	5
165	Completed R&D for DS-20kProgram	6
166	Ongoing R&D for DS-20kProgram	7
167	Project Overview	7
168	Photoelectronics	10
169	PhotoDetector Modules (PDM)	11
170	Signal Transmission	12
171	PBM Fabrication and Characterization	12
172	Motherboard Assembly	14
173	Mass Production	15
174	Inner Detector and Cryogenics System	15
175	DS-20k LAr TPC	15
176	Cryogenics	21
177	Material Assays	27
178	Radio-purity database	28
179	Managing Assay Capabilities	29
180	Radioactive budget	29
181	Calibration	30
182	Distributed Gas Sources	30
183	Gamma Sources	31
184	Neutron Sources	31
185	Guide Tube System	33
186	Veto Detector	34
187	Overall Design	34
188	Assembly	35
189	Background Rejection	36
190	Data Acquisition	38
191	General DAQ scheme	38
192	Digitizers	39
193	DAQ software	39
194	Computing	40
195	Computing systems and data workflow	40
196	Software Environment	41
197	Simulation	42

198	The ReD Experiment	42
199	DarkSide-Proto	45
200	P rototype Overview and Status	45
201	T he DS-Proto TPC	46
202	M aterials for DarkSide-Proto	49
203	V alidation tests and operation	49
204	A Ar Cryostat	49
205	M argon Procurement and Purification	53
206	U rania	53
207	M ia	58
208	D AFT	60
209	R efferences	62

LIST OF FIGURES

211	1	Artist rendering of the DS-20k detectors	2
212	2	Current DM limits and sensitivities for future experiments.....	3
213	3	5σ discovery potential of the leading future noble liquid dark matter searches.....	6
214	4	Artist rendering of the DS-20k experiment in Hall C of LNGS.....	8
215	5	The first PDM and first motherboard resulting from the assembly of PDMs.....	11
216	6	Schematic of the transimpedance amplified and summing circuits.....	12
217	7	Variance of impedance of SiPMs quenching resistors	13
218	8	SiPM <i>I-V</i> curves and SNR	14
219	9	SNR of the SiPMs tiles of the first motherboard	15
220	10	Artist rendering of the PMMA vessel and the TPC	17
221	11	PDM patterning scheme.....	18
222	12	DS-20k PDM motherboard designs	19
223	13	3D model of the full DS-20k LAr TPC reflector panels system.....	20
224	14	DS-20k LAr TPC anode and cathode regions	21
225	15	Simulated electric field mapping of the DS-20k LAr TPC	23
226	16	DS-20k cryogenics system P&ID	24
227	17	DS-20k condenser box	25
228	18	DS-20k materials database structure	28
229	19	Web interface of DS-20k materials database.....	29
230	20	Schematic of the sources insertion system.....	32
231	21	Pictures of the miniature $^{241}\text{AmBe}$ neutron source	33
232	22	Schematic and 3D cut-away view of the DS-20k veto detector	34
233	23	3D drawings of the DS-20k Veto detector.....	36
234	24	Picture of the LNS beamline in use for ReD	44
235	25	Preliminary data from the ReD experiment	45
236	26	The DS-Proto cryostat and components delivered at CERN	47
237	27	Conceptual design of the DS-Proto detector	48
238	28	Schematics of the setup for the optimization of the S2 signals	50
239	29	Details of the AAr cryostat	51
240	30	3D view of the large AAr cryostat	51
241	31	Cross-sectional view of the large AAr cryostat	52
242	32	Process Flow Diagram for the Urania UAr extraction plant	55
243	33	Screening test plant for the Urania PSA sorbent	56
244	34	Schematic view of UAr cryogenic shipping vessel	57
245	35	Block diagram of Aria	59
246	36	The Seruci-0 cryogenic distillation column	61

LIST OF TABLES

248 I	Radiogenic neutrons sourced by the detector construction materials and background 249 before and after cuts.	4
250 II	DS-20k LAr TPC detector parameters	16
251 III	DarkSide-20k cryogenics system parameters.....	22
252 IV	Summary of DS-20k assays performed.....	30
253 V	Summary of the assay capabilities available for DS-20k	30
254 VI	Radiogenic neutrons from detector materials and background before and after cuts. .	37
255 VII	Inlet argon purity required for operation of the DarkSide-20k getter	53

1. EXECUTIVE SUMMARY

257 **La parte iniziale del TDR riassume le motivazioni scientifiche e/o tecnologiche che
 258 hanno portato alla proposta per la realizzazione del progetto in questione, un'overview
 259 della soluzione proposta e l'evoluzione del progetto nel tempo. Si tratta di un som-
 260 mario esecutivo dalla lunghezza di 1-2 pagine, che include anche una descrizione som-
 261 maria dei contenuti del documento.**

2. PHYSICS CASE

263 **In questa parte viene riassunto inizialmente il lavoro svolto durante la fase di R&D
 264 del progetto, finanziata nella fase di CDR. Vengono descritti i risultati degli R&D ma
 265 anche i problemi trovati in questa fase, e le soluzioni proposte per risolverli o soluzioni
 266 alternative. Vengono anche elencati ulteriori R&D che si pensa di dover svolgere
 267 per finalizzare eventuali scelte tecniche Inoltre viene descritto il progetto nelle sue
 268 generalità e nel suo contesto. Vengono discusse le motivazioni scientifiche che hanno
 269 portato alla proposta in questione, con una chiara indicazione degli obiettivi e dei
 270 risultati attesi.**

271 There is strong evidence from astronomical and cosmological observations for the existence of
 272 dark matter in our Universe. Weakly Interacting Massive Particles (WIMPs) are a well-motivated
 273 dark matter candidate that may have been produced in the early Universe but are so massive and
 274 weakly interacting that they have yet to be observed in a terrestrial experiment. The observation
 275 of WIMPs with masses up to about $1 \text{ TeV}/c^2$ is a major objective of the experimental program at
 276 the High Luminosity Large Hadron Collider. Future high energy colliders like the FCC-*hh* (Future
 277 Circular Collider) will be able to extend these searches up to the $10 \text{ TeV}/c^2$ mass range [1]. Direct
 278 and indirect dark matter detection techniques allow for a search program complementary to future
 279 colliders. For example, the direct detection of dark matter via elastic scattering of galactic WIMPs
 280 from a liquid argon target is a demonstrated technique capable of probing masses well above the
 281 reach of the LHC.

282 Liquid argon (LAr) is a particularly favorable target for the detection of WIMPs thanks to its
 283 excellent event discrimination capabilities. Scintillation light initiated by particles recoiling from
 284 atomic electrons (ERs), the primary source of background in a WIMP direct detection experiment,
 285 has a time constant of approximately a microsecond. This is in stark contrast to the nanosecond
 286 time constant of scintillation light emitted during an expected WIMP-nuclear recoil event (NR).
 287 The DEAP-3600 experiment has exploited this effect via pulse shape discrimination (PSD) to
 288 achieve ER background rejection of 2.4×10^8 [2, 3]. Additional event discrimination in an argon-
 289 based detector was demonstrated by the DarkSide-50 (DS-50) experiment, which uses a two-phase
 290 time projection chamber to measure both the prompt argon scintillation light and the ionized
 291 electrons resulting from a particle interaction in the detector. This technique provides excellent
 292 position resolution and efficient detector fiducialization while maintaining PSD capabilities [4, 5].
 293 DS-50 has performed a blind analysis of their data and observed no background events over a run
 294 period in excess of two years [6]. In addition to sensitivity to WIMPs with masses above $30 \text{ GeV}/c^2$,
 295 the two-phase DS-50 detector has extended its reach to WIMP masses below $10 \text{ GeV}/c^2$ by detecting
 296 single ionizaton electrons extracted from the liquid argon volume [7, 8]. With careful control of ER
 297 background from local radioactivity and a reduction of the ^{39}Ar background, a 1 t LAr detector
 298 has the potential to reach the “neutrino floor” of solar neutrinos in this low-mass parameter space.

299 Given the potential reach of an argon-based detector, scientists from all of the major groups cur-
 300 rently using LAr to search for dark matter, including ArDM, DS-50, DEAP-3600, and MiniCLEAN,
 301 have joined to form the Global Argon Dark Matter Collaboration (GADMC) with a goal of building
 302 a series of future experiments that maximally exploit the advantages of LAr as a detector target.

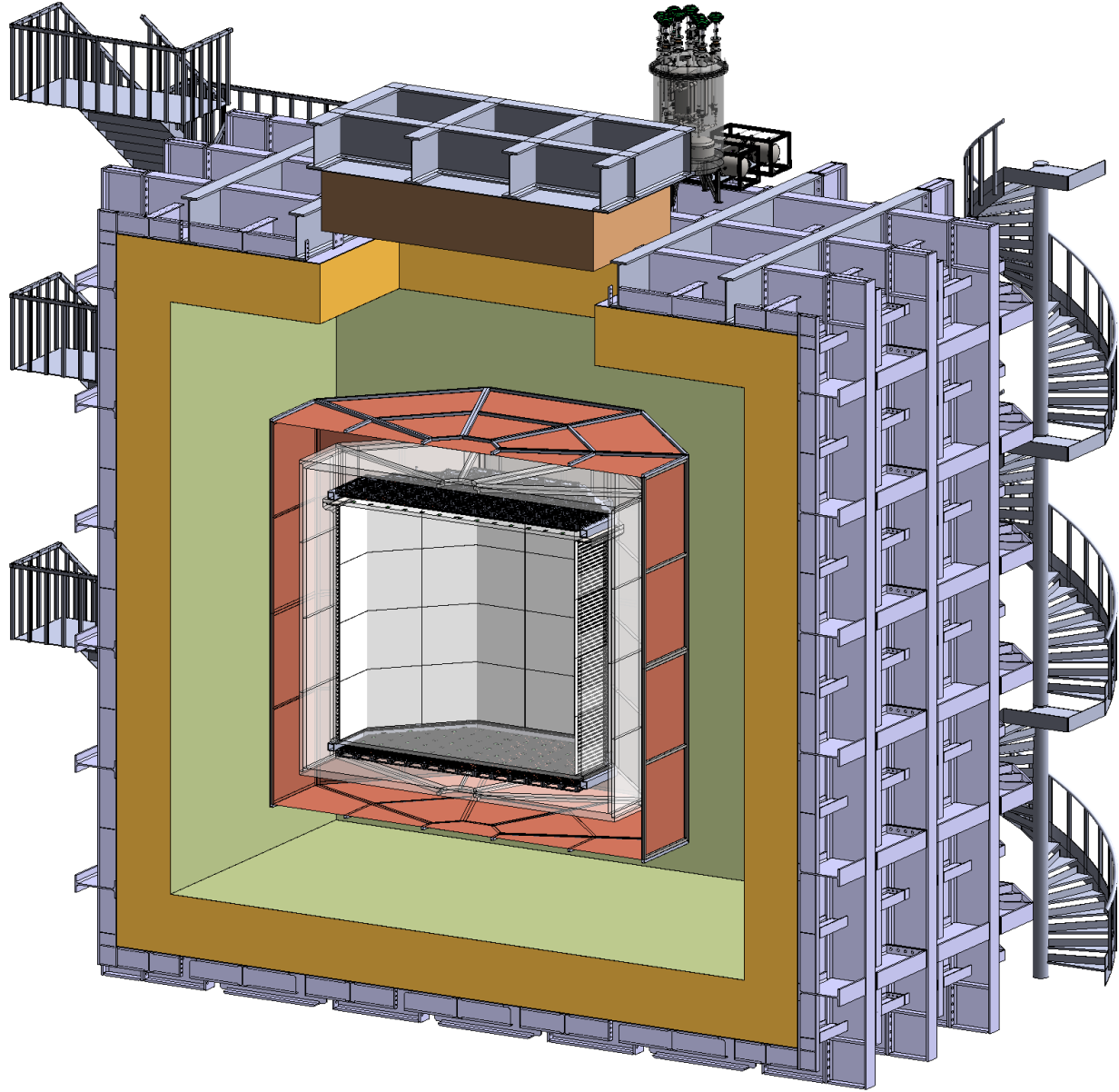


FIG. 1. Artist rendering of the DS-20k detectors, with many components omitted for clarity of presentation. The drawing shows the acrylic (PMMA) sealed TPC filled with UAr, surrounded by the veto detector consisting of a Gd-loaded acrylic Shell (GdAS) sandwiched between two atmospheric argon (AAr) active layers (the Inner Active Buffer, IAB and the Outer Active Buffer, OAB), all contained in the ProtoDUNE-like cryostat. The OAB is optically separated from the rest of the AAr by a copper vessel. Technical designs of the support structure of the TPC are already available, and intentionally omitted for clarity of presentation of the main elements.

303

2.1. DarkSide-20k: The High-Mass Search Program

304 The immediate objective of the GADMC is construction of the DS-20k two-phase LAr detector,
 305 which will operate in Hall-C of the Gran Sasso National Laboratory (LNGS). Fig. 1 shows a 3D
 306 schematic of the DS-20k detector. DS-20k detector consists of two nested detectors housed within
 307 a ProtoDUNE-style membrane cryostat [9, 10].

308 The inner detector is a dual-phase argon time projection chamber (LAr TPC) contained within
 309 a vessel made from ultra-pure acrylic (PMMA) and filled with UAr. The central active volume of

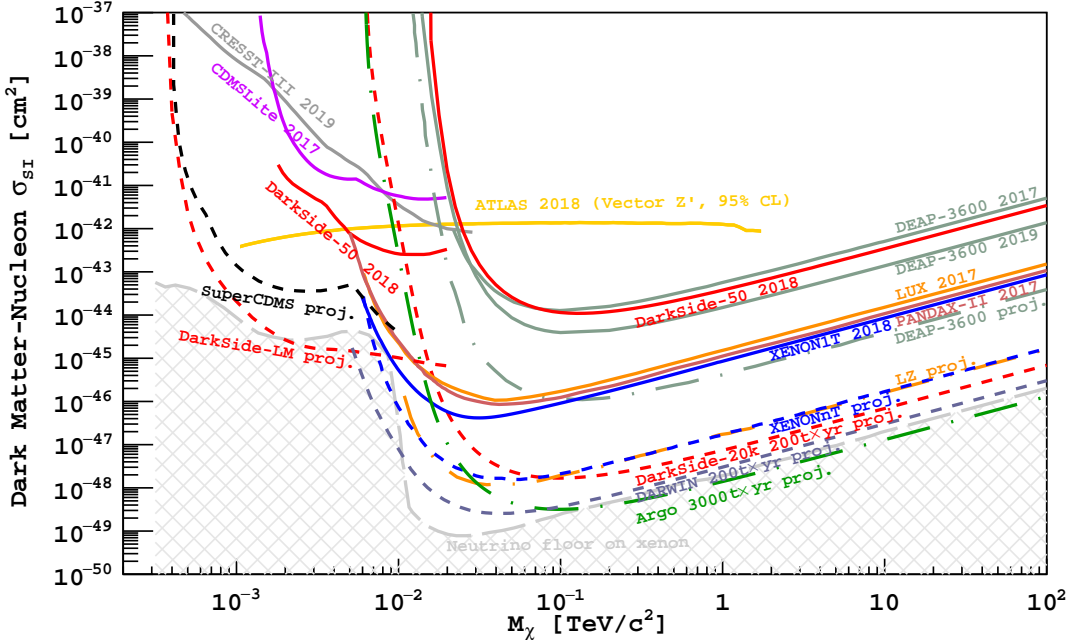


FIG. 2. 90 % C.L. exclusion limits showing leading results from direct (continuous lines, Ref. [6, 7, 12–15]) and accelerator-based dark matter searches (region above the yellow line [16]) compared with sensitivities of future germanium-, xenon-, and argon-based direct searches (dashed lines, Ref. [17–21] and this work). The “neutrino floor” curve follows the definition of Ref. [22]. The 95% C.L. limit from the ATLAS Experiment is shown for a benchmark model in which Dirac-fermion WIMPs interact with ordinary matter via a vector mediator with coupling strengths to quarks, leptons and WIMPs of 0.25, 0.01, and 1, respectively [23].

310 the TPC is defined by eight vertical reflector panels and the top and bottom windows of the acrylic
 311 vessel. Instead of the traditional copper field cage rings and Indium-Tin-Oxide (ITO) cathode
 312 and anode, DS-20k will use poly(3,4-ethylenedioxothiophene) polystyrene sulfonate (also known
 313 as PEDOT:PSS and commercialized under the name Clevios™ [11]). All the TPC surfaces in
 314 contact with the active argon volume will be coated with wavelength shifter tetraphenylbutadiene
 315 (TPB) to convert LAr scintillation light to a wavelength detectable by SiPMs. 8280 SiPM-based
 316 PhotoDetector Modules (PDM) arrays will view the argon volume through the top and bottom
 317 windows of the acrylic vessel. The height of the TPC is 350 cm. The total mass of LAr in the
 318 active volume is 49.7 t.

319 The outer veto detector is made of a passive Gd-loaded PMMA shell surrounding the inner
 320 detector and between two active AAr layers. The Gd-loaded PMMA shell moderates
 321 neutrons emitted from the LAr TPC until they capture on Gd, resulting in the emission of multiple
 322 γ -rays. The γ -rays interact in the AAr layers and cause scintillation light that is detected by
 323 photodetectors, thereby providing an efficient veto of radiogenic neutrons that could result in a
 324 NR in the TPC. The ProtoDUNE-like cryostat will be surrounded by layers of plastic to moderate
 325 cosmogenic and radiogenic neutrons from the rocks surrounding Hall C.

326 The DS-20k detector will have ultra-low backgrounds and the ability to measure its backgrounds
 327 *in situ*, resulting in an expected sensitivity to WIMP-nucleon cross sections of $1.2 \times 10^{-47} \text{ cm}^2$
 328 ($1.1 \times 10^{-46} \text{ cm}^2$) for $1 \text{ TeV}/c^2$ ($10 \text{ TeV}/c^2$) WIMPs following a five years run. This projected
 329 sensitivity is a factor of >50 better than currently-published results above $1 \text{ TeV}/c^2$ and covers a
 330 large fraction of the parameter space currently preferred by supersymmetric models.

331 The sensitivity would further improve to $7.4 \times 10^{-48} \text{ cm}^2$ ($6.9 \times 10^{-47} \text{ cm}^2$) for $1 \text{ TeV}/c^2$ ($10 \text{ TeV}/c^2$)
 332 WIMPs for a ten years run with a 200 t yr exposure, see Fig. 2. During the 200 t yr exposure, 3.2
 333 NRs events are expected from the coherent scattering of atmospheric neutrinos, making DS-20k the

Material	Mass [tonne]	^{238}U [mBq/kg]	^{226}Ra [mBq/kg]	^{232}Th [mBq/kg]	Neutrons $[10 \text{ yr}]^{-1}$	+TPC $[200 \text{ t yr}]^{-1}$	+TPC+veto $[200 \text{ t yr}]^{-1}$
TPC Vessel	2.7	1.2×10^{-2}	10	4.1×10^{-3}	5.7×10^2	0.17	1.7×10^{-2}
TPC SiPMs	0.12	-	-	-	5.4×10^3	0.16	1.6×10^{-2}
TPC Electronics	1.0	-	-	-	1.2×10^4	0.36	3.6×10^{-2}
TPC Mechanics	1.1	3.9	3.9	1.9	9.0×10^2	1.8×10^{-2}	2.0×10^{-3}
Veto SiPMs+elec.	0.40	-	-	-	6.4×10^3	0.10	1.0×10^{-2}
Veto Acrylic	13	1.2×10^{-2}	10	4.1×10^{-3}	2.6×10^3	4.2×10^{-2}	4.0×10^{-3}
Veto Reflectors	1.0	1.2×10^{-2}	1.0	4.1×10^{-3}	2.0×10^2	2.4×10^{-2}	2.0×10^{-3}
Veto Steel	1.1	3.9	3.9	1.9	9.0×10^2	1.4×10^{-2}	1.0×10^{-3}
$\text{Gd}_2(\text{SO}_4)_3$ α 's on self	0.26	7.0	7.0	0.2	1.1×10^2	2.0×10^{-3}	$<1.0 \times 10^{-3}$
$\text{Gd}_2(\text{SO}_4)_3$ α 's on PMMA	0.26	7.0	7.0	0.2	3.6×10^2	6.0×10^{-3}	1.0×10^{-3}
Copper Cage	1.0	0.30	0.30	2.0×10^{-2}	6.0	$<1.0 \times 10^{-3}$	$<1.0 \times 10^{-3}$
Cryostat Steel	250	50	1.0×10^3	3.9	1.0×10^6	-	$<1.0 \times 10^{-3}$
Cryostat Insulation	40	3×10^3	8.0×10^3	3.0×10^3	8.0×10^7	-	$<1.0 \times 10^{-3}$
Total						0.9	0.09

TABLE I. Radiogenic neutrons sourced by the LAr TPC construction materials, veto and cryostat materials, with details of expected contamination levels, background after TPC cuts, and residual background after combined TPC and veto cuts, all relative to the full 10 yr run time and the full fiducial 200 t yr exposure. The number of neutrons source is calculated from the expected contamination levels and material composition. Note that no specific activity is reported for the TPC SiPMs and associated electronics: in this case the predicted neutron yield is the results of an extremely detailed calculation, accounting for the cumulative contribution of several tens of components, individually assayed. The same consideration holds for the veto SiPMs and electronics, whose contribution is reported in combination. For neutrons due to (α, n) reactions from α 's from impurities in $\text{Gd}_2(\text{SO}_4)_3$, the contribution is broken down between those due reactions on Gd sulfate itself and those due to reactions in the PMMA matrix containing the Gd sulfate; the mass fraction of Gd in the GdAS 1%, for the anticipated 2% concentration by mass of $\text{Gd}_2(\text{SO}_4)_3$. (For ease of conversion: 1 ppt(^{238}U) $\simeq 1.2 \times 10^{-2}$ mBq/kg; 1 ppt(^{232}Th) $\simeq 4.1 \times 10^{-3}$ mBq/kg.)

334 first ever direct dark matter detection experiment to reach this milestone. The DS-20k experiment
 335 is foreseen to begin operating in 2022 and will either detect WIMP dark matter or exclude a large
 336 fraction of favored WIMP parameter space.

337 DS-20k is designed to operate with zero backgrounds, meaning that all sources of instrumental
 338 background are reduced to <0.1 events over a 200 t yr exposure. All background from minimum-
 339 ionizing radiation sources will be completely removed thanks to the combined action of PSD of the
 340 primary scintillation pulse and comparison of the primary and secondary scintillation (see Sec. 22.4
 341 for details on the suppression of background from pp scatters on electrons and Ref. [24] for that
 342 from ^{222}Rn , ^{220}Rn , and progenies). Table VI shows the expected radiogenic neutron background
 343 contributions of the various detector components following all TPC and veto cuts for the full DS-20k
 344 exposure. The only remaining background for WIMP searches will be the signal from the coherent
 345 scattering of atmospheric neutrinos on argon nuclei, with an expected 3.2 events over the 200 t yr
 346 exposure. DS-20k will thus be the first experiment in a position to detect this important signal.

347 This outstanding sensitivity to coherent nuclear recoils will enable DS-20k to detect a supernova
 348 neutrino burst coming from anywhere in the Milky Way Galaxy and, for a majority of the galaxy,
 349 clearly identify the neutronization burst. DS-20k would perform a flavor-blind measurement of
 350 the total neutrino flux and average energy, setting an overall normalization that is not affected
 351 by neutrino oscillations. When combined with a flavor-specific measurement from a detector like
 352 Super-Kamiokande or DUNE, this observation could have sensitivity to the neutrino mass hierarchy.

353 2.2. DarkSide-LowMass: The Low-Mass Search Program

354 In parallel to DS-20k detector, the GADMC will pursue the development of an approximately
 355 1 t detector specifically optimized for the detection of low-mass dark matter, DarkSide-LowMass
 356 (DS-LM). DS-LM will achieve a lower energy threshold than DS-20k by triggering on the electro-

357 luminescence signal from ionization electrons, thereby adding sensitivity to WIMP masses below
358 $10 \text{ GeV}/c^2$ at the expense of the PSD power afforded by argon prompt scintillation light. Without
359 PSD, contributors to the ER background in DS-LM must be reduced beyond the requirements of
360 DS-20k through careful detector design and material selection. While the DS-LM experiment is
361 outside the scope of this proposal, the implementation of DarkSide-20k project will have direct
362 impacts on the technological advancements required to enable DS-LM and the goal of reaching the
363 neutrino floor for WIMP masses between $1 \text{ GeV}/c^2$ and $10 \text{ GeV}/c^2$, see Fig. 2. Among these are the
364 development of low-background PDMs [25, 26] and the construction of the Aria cryogenic distilla-
365 tion column, which will completely remove ^{85}Kr and reduce ^{39}Ar levels to the level of $1 \mu\text{Bq}/\text{kg}$.
366 The development of DS-LM may exploit components of the DS-Proto detector under development
367 at CERN. Funding for the development, construction, commissioning, and operation of DS-LM
368 will be separately requested via alternative funding programs.

369 **2.3. Argo**

370 The ultimate objective of the GADMC is the construction of the Argo detector, which will have
371 a 300 t fiducial mass and will push the experimental sensitivity to the point at which the coherent
372 scattering of atmospheric neutrinos becomes a limiting background. The excellent ER rejection
373 possible in argon will eliminate backgrounds from solar neutrinos, which will extend the sensitivity
374 of Argo beyond that of technologies with more limited ER discrimination. The throughput of the
375 Urania plant and Aria facility will enable 400 t of UAr to be extracted and purified over a period
376 of about 6 yr. In addition to dark matter detection, such a large detector would also have excellent
377 sensitivity to a neutrino burst associated with a galactic supernova. If located at SNOLAB or at
378 similar depth, Argo will also have the potential to observe CNO neutrinos for the first time and
379 solve the Solar Metallicity Problem [27]. While the construction of Argo is not within the scope of
380 this proposal, the implementation of DarkSide-20k project will pave the way for the development
381 of Argo towards the end of the next decade.

382 Combined DS-20k, DS-LM, and Argo, will completely cover the spin-independent WIMP hy-
383 pothesis parameter space down to the neutrino floor for WIMP masses from $1 \text{ GeV}/c^2$ to several
384 hundreds of TeV/c^2 .

385 **2.4. Comparison with Xenon-Based Experiments and the “Neutrino Floor”**

386 Next generation dark matter experiments will be sensitive to several sources of neutrinos via $\nu - e$
387 elastic scattering and coherent elastic neutrino scattering ($\text{CE}\nu\text{NS}$) on nuclei (NR). Atmospheric
388 and diffuse supernovae neutrinos, which due to their high energies can produce NRs in excess of
389 $20 \text{ keV}_{\text{nr}}$, will be the dominant $\text{CE}\nu\text{NS}$ background contributor for WIMP masses above $30 \text{ GeV}/c^2$.
390 Solar neutrinos are the main $\text{CE}\nu\text{NS}$ background for dark matter masses below $10 \text{ GeV}/c^2$. With
391 argon’s ability to discriminate ER from NR to better than a part in 2.4×10^8 , $\text{CE}\nu\text{NS}$ represents
392 the only irreducible background for a large exposure argon dark matter search. The neutrino
393 background is exacerbated in liquid xenon detectors, which, due to their limited ER rejection
394 power, accept a non-negligible number of $\nu - e$ elastic scatters as signal.

395 When calculating the discovery sensitivity of a large dark matter search experiment, one must
396 fully account for the presence of neutrino-induced backgrounds. We note that the position of the
397 “neutrino floor”, initially conceived as indicative of the maximum sensitivity attainable by an ex-
398 periment in the presence of $\text{CE}\nu\text{NS}$ background, is critically dependent on the target, experimental
399 technique, statistical analysis, neutrino flux uncertainty and theoretical cross section uncertainty.
400 We therefore include a detailed accounting of the $\text{CE}\nu\text{NS}$ and $\nu - e$ backgrounds in the sensitivity
401 and discovery potential curves shown in Fig. 2 and Fig. 3. We conservatively estimate a 20 % un-
402 certainty on the neutrino background for high-mass ($30 \text{ GeV}/c^2$) searches with Argo. This accounts
403 for a 15 % uncertainty on the atmospheric neutrino flux at mid-latitude locations, such as SNOLAB

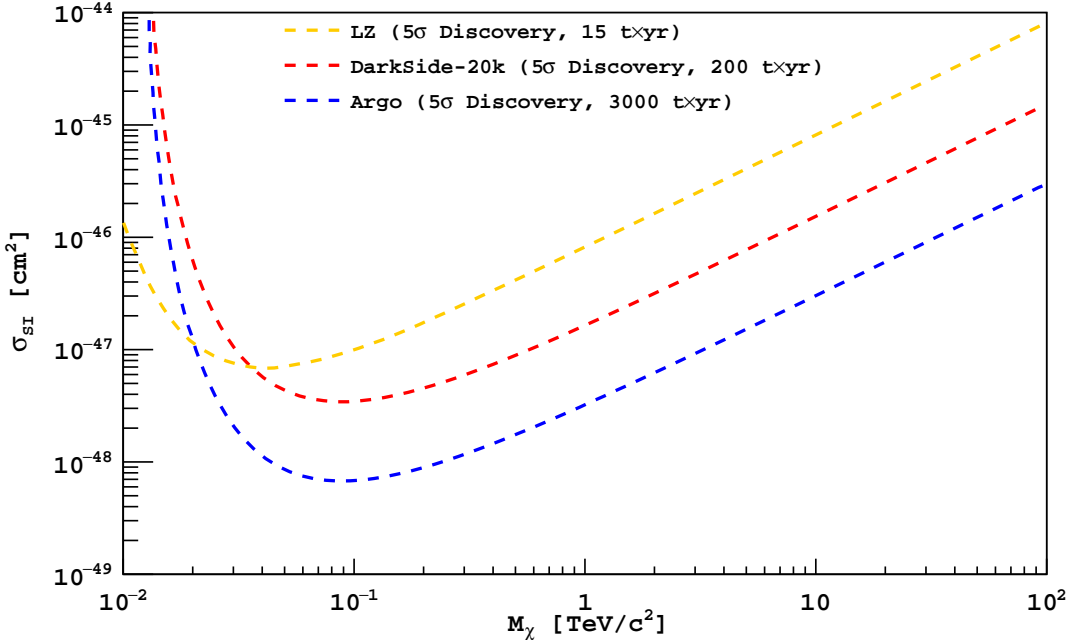


FIG. 3. 5σ discovery potential of the leading future noble liquid dark matter searches.

or LNGS, based on the latest data-driven models of cosmic primaries [28] as well as models of solar cycle, seasonal, geographic, and geomagnetic dependence of the neutrino flux [29, 30]. Additionally, we account for a 5 % theoretical uncertainty on the Standard Model interaction cross-section, driven by uncertainties on the nuclear form factor and the expected constraints that the COHERENT collaboration will place on non-Standard Model contributions using a LAr target [31], which in turn is driven by their current 10 % uncertainty on neutrino flux [32] and a 6 % uncertainty on the LAr response as measured by SCENE [33, 34] and ARIS [35]. Planned improvements of COHERENT, including a sharper characterization of the neutrino flux and a measurement with a LAr target, would further reduce the uncertainty on the neutrino background below 10 %, strongly benefiting the DS-20k, and Argo experiments.

Within this framework, we calculate the 5σ discovery potential for DS-20k and Argo and compare it with that of the near-future LXe experiment LZ [36]. As seen from Fig. 3, DS-20k has significantly greater discovery potential than that of LZ.

417

2.5. Completed R&D for DS-20k Program

418 The following technologies are key to the success of DarkSide-20k project and the long term
 419 scientific goals of the GADMC. Their development will also have potentially wide-reaching effects
 420 within the physics community.

421 **Low-Radioactivity Underground Argon with Urania** [24]: The DS-50 experiment estab-
 422 lished that UAr is depleted of ^{39}Ar by a factor of approximately 1400, a sufficiently low rate to be
 423 deployed in a detector the size of DS-20k. However, constructing DS-20k will require that large
 424 amounts of UAr be procured in a timely fashion. This will be accomplished by Urania, an argon
 425 extraction and purification plant capable of extracting 250 kg/d of UAr. The Urania plant is fully
 426 funded by the INFN and will be built by a contracted vendor following specifications established
 427 by the Urania Project team. The tender process for the plant's final design, construction, and
 428 shipment to the installation site in Cortez, Colorado, is underway and will conclude by the end

429 of July 2019 with the selection of a contractor. The preparation of the extraction site, as well
430 as the installation and commissioning of the plant, falls under the responsibility of the U.S. NSF-
431 supported groups. The Urania UAr extraction plant is projected to collect approximately 60 t of
432 argon for use in DS-20k detector by 2022 and could continue to produce underground argon for
433 Argo and other interested particle physics experiments that require UAr to achieve their scientific
434 objectives.

435 **Purification and Active Depletion with Aria [24]:** The Aria plant is a 350 m tall cryogenic
436 distillation column that was designed to explore the possibility of chemically separating argon iso-
437 topes. The construction of Aria is fully supported by INFN and Regione Autonoma della Sardegna.

438 **SiPM-based Cryogenic Photosensors [24–26]:** The development of low-background, large-
439 area, cryogenic silicon photomultiplier (SiPM) detectors capable of replacing conventional photo-
440 multiplier tubes is critically important for achieving the desired sensitivity of DS-20k and other
441 large-scale LAr-based experiments, including DUNE, and LXe-based detectors, such as nEXO [37]
442 and NEXT [38–40]. The DS-20k photodetector modules will be assembled at the Nuova Offi-
443 cina Assergi (NOA), a dedicated cleanroom packaging facility that will have future utility for any
444 experiment needing large volume silicon detector production.

445 **ProtoDUNE Liquid Argon Cryostat [9, 10]:** DS-20k detector will operate within a mem-
446 brane cryostat filled with liquefied atmospheric argon, a technology initially developed at CERN
447 for ProtoDUNE. Eliminating the organic liquid scintillator veto used in DS-50 for the AAr veto
448 has several advantages. With the the DS-20k LAr TPC directly immersed in AAr, the massive
449 stainless steel vacuum cryostat necessary for DS-50, and its correspondingly large contribution of
450 background events, can be replaced with a transparent, radio-pure PMMA vessel. Photodetector
451 modules can then be mounted outside of the PMMA vessel, reducing their contribution to the
452 background rate and simplifying their assembly strategy. The ProtoDUNE cryostat has the added
453 advantage that it is scalable, making it a technology appropriate for Argo.

454 **Sealed PMMA TPC [2, 41, 42]:** The DEAP-3600 collaboration has extensive experience
455 developing large, radio-pure sealed PMMA vessels. This technology will be used to build the vessel
456 for the DS-20k LAr TPC, eliminating the need for some of the most problematic radiogenic neutron
457 contributors in DS-50, most notably the stainless steel cryostat. The PMMA vessel will also reduce
458 the complexity of the TPC assembly.

459 2.6. Ongoing R&D for DS-20kProgram

460 All the major technologies needed for the design and construction are proven and do not neces-
461 sitate further R&D by the collaboration as discussed in the preceding paragraph. Some limited
462 developments are only needed in order to finalize the mass production for SiPM and the production
463 of the Gd loaded acrylic panels for the construction of the neutron veto. In both cases the R&D is
464 actively on-going and will be finalized by 2020.

465 3. PROJECT OVERVIEW

466 Many fundamental design parameters for the DarkSide-20k (DS-20k) experiment are based on
467 the successful experience of the DarkSide Collaboration in constructing, commissioning, and oper-
468 ating the DarkSide-50 (DS-50) detector in a background-free mode. The many technical details of
469 DarkSide-50 can be found in [4–8, 35, 43–50]. The DS-20k liquid argon time projection chamber
470 (LAr TPC) will, too, be deployed at LNGS in the underground Hall C, at the center of a newly
471 constructed active veto system. Fig. 4 shows the rendering of the future installation of DS-20k in
472 the underground Hall C of LNGSand Fig. 1 shows an overview of the detailed arrangement of the
473 LAr TPC and its anti-coincidence veto detector. The DS-20k experiment is designed to operate for
474 a minimum of 10 yr while maintaining an irreducible background level in the WIMP search region
475 of less than <0.1 events for the total exposure. To achieve this goal, the design parameters of the

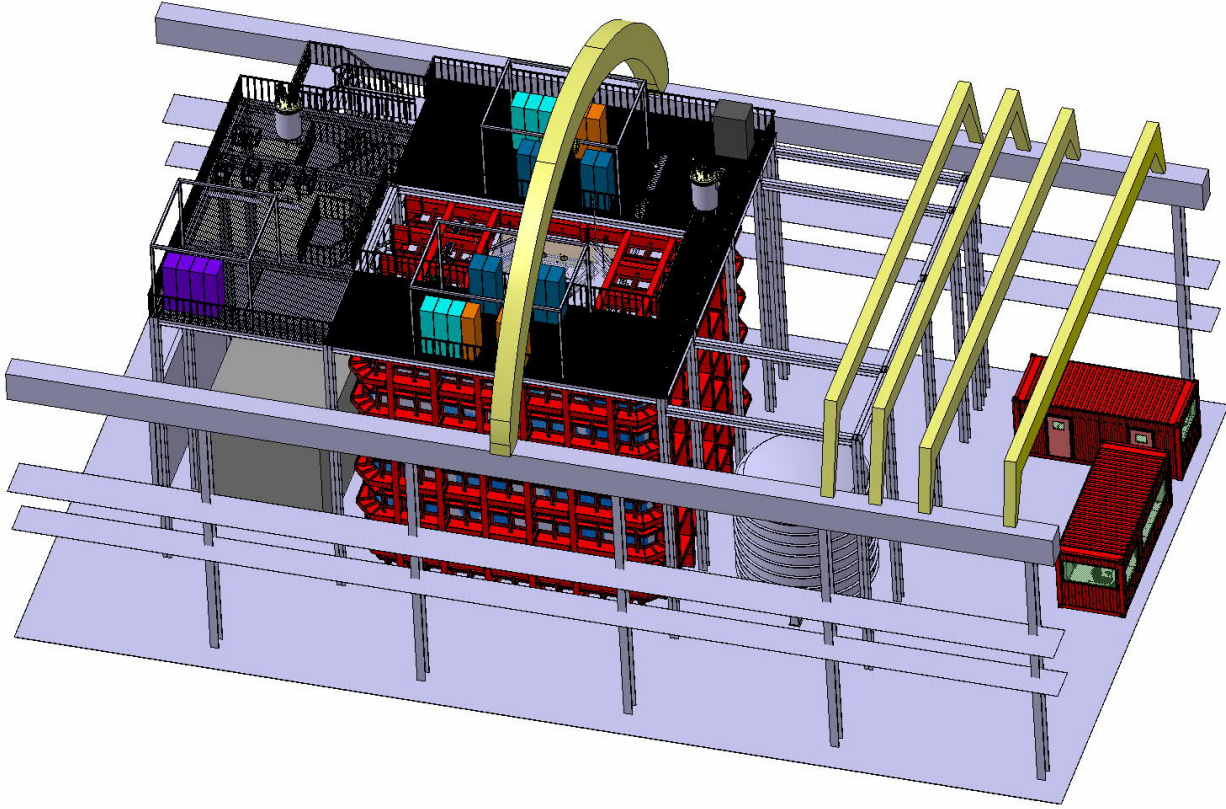


FIG. 4. Artist rendering of the DS-20k experiment in Hall C of LNGS.

476 DS-20k experiment have been taken directly from DS-50, where possible. Design changes have been
 477 made where needed in order to accommodate for the much larger size of DS-20k and to allow the
 478 experimental design to be scalable to a detector at the multi-hundred tonne scale. In building this
 479 preliminary design, issues that have arisen because of design choices or materials selections have
 480 been dealt with by limited design modifications, and further optimization will continue as the final
 481 development work is completed and a full technical design is made.

482 DS-20k will be built by the Global Argon Dark Matter Collaboration (GADM) and will consist
 483 of two detectors: the inner detector and the veto detector, both hosted in a ProtoDUNE-like
 484 cryostat [9, 10]. The inner detector is a LAr TPC filled with underground argon (UAr). The veto
 485 detector is made of a plastic shell, loaded with Gd, surrounding the inner detector, sandwiched
 486 between two active atmospheric argon (AAr) layers.

487 The decision to abandon an organic liquid scintillator veto and to host DS-20k within a
 488 ProtoDUNE-like cryostat was originally motivated by the need of minimizing the environmen-
 489 tial impact on underground LNGS operations, but carries significant performance advantages.
 490 Indeed, operating the TPC directly in the ProtoDUNE-like cryostat eliminates the need of a cryo-
 491 stat in the immediate proximity of the UAr target, which would significantly contribute to the
 492 residual background. We therefore adopted a new design, with the UAr-filled TPC immersed in a
 493 bath of liquefied AAr held at the same temperature and pressure. This then allows for the use of
 494 a TPC vessel fabricated from the same ultra-pure poly(methyl methacrylate) (acrylic or PMMA)
 495 developed for the DEAP-3600 experiment, and thus eliminating the need for a dedicated cryostat
 496 or UAr containment vessel. The outer walls of the TPC will sit approximately 2 m away from inner
 497 wall of the cryostat. The ProtoDUNE-like cryostat may be surrounded by layers of plastic for
 498 moderation of cosmogenic and radiogenic neutrons from the rocks surrounding the LNGS Hall C,
 499 this option is being investigated.

500 While this overview section gives a general outline of the project and introduces the major

501 features of the experiment as they stand in the current preliminary design, the real details are
502 given in the subsequent sections. The development of the SiPM photosensors, the LAr TPC and
503 its cryogenics and gas handling system, and the materials screening plan that will ensure the radio
504 purity of the experiment, are detailed in Sec. 4, Sec. 5 and Sec. 6, respectively. The plan for the
505 calibration of the experiment is given in Sec. 7, the design of the veto detector is presented in
506 Sec. 8, and the details about the data acquisition system and the plan for offline computing are
507 given in Sec. 9 and Sec. 10, respectively. The two ancillary detectors, ReD and DarkSide-Proto,
508 are described in Sec. 11 and Sec. 12. Finally, the design and use of the atmospheric argon cryostat,
509 modeled after the ones deployed for ProtoDUNE, are given in Sec. 13, while the procurement of the
510 underground argon (UAr) target is detailed in the final section, Sec. 14. Note that the following
511 forms a preliminary design for an experiment capable of the stated physics goals, but may change
512 as the technical details evolve in the final engineering stages. DS-20k will be built to operate for a
513 minimum of 10 yr, providing the best sensitivity to high-mass WIMP dark matter.

514 Energy deposits in the LAr target result in the production of excited and ionized argon atoms,
515 according to the underlying process for recoiling electrons or nuclei. Excited argon atoms, which
516 can also be produced by recombining ionization charge, lead to an efficient formation of argon
517 excimers decaying via the emission of scintillation light characterized by two decay time constants.
518 Both of the components are combine to yield an instant light signal, called S1. Due to the deep UV
519 nature (around 128 nm) of this scintillation light, which is absorbed by most materials, a thin layer
520 of wavelength shifter, tetraphenyl butadiene (TPB), must cover all exposed surfaces to convert the
521 photons to those of optical wavelengths for detection by photosensors. Ionization electrons escaping
522 recombination are drifted to the top of the LAr by an applied electric field, where an electric field
523 stronger than the field applied to drift the electrons, extracts the electrons into the gas pocket
524 above the liquid. Here the strong field accelerates the electrons, enough for them to excite (but not
525 ionize) the argon gas, producing a secondary scintillation signal S2, proportional to the ionization
526 charge. Photosensors placed behind the wavelength shifter-coated windows at the top and bottom
527 of the TPC, read out both scintillation signals (S1 and S2) of each event. S1 is used for energy
528 determination, as well as for pulse shape discrimination (PSD). The latter is derived from the ratio
529 of the prompt and delayed light fractions. S2 is used for energy and 3D position measurements
530 of the event, the vertical coordinate is measured from the drift time between S1 and S2, and the
531 horizontal coordinates from the light pattern resulting in the top photosensors from S2.

532 The octagonal LAr TPC will have a height of 350 cm and a distance between parallel walls of
533 355 cm. It will be instrumented with a new kind of photosensors, arrays of SiPMs, arranged in
534 assemblies called photodetector modules (PDMs). Each PDM has an area comparable to that of
535 a 3" photomultiplier tube (PMT), with the LAr TPC containing 8280 PDMs in total. Substantial
536 effort was put into the development of this technology, since SiPMs promise a higher effective
537 quantum efficiency, higher reliability at LAr temperature, and a much higher radiopurity than
538 PMTs. All of these properties are crucial for DS-20k since the PSD, which is the most important
539 mechanism for background discrimination in LAr, depends critically on the light yield. Additionally,
540 the large material budget of PMTs is often a limiting factor for neutron- and gamma-induced
541 backgrounds. The LAr TPC will be equipped with arrays of SiPMs, totaling 21 m² in area.

542 In comparison to DS-50, where a full digitization and recording of the waveform of each PMT
543 could be achieved, a custom scheme for the sampling of the two-orders-of-magnitude higher channel
544 count of the DS-20k SiPM PDMs has to be developed. Design parameters for the data acquisition
545 (DAQ) system are driven by rates and occupancies, as well as leading edge timing and limited
546 charge information from each channel, while compromising as little as possible on energy resolution
547 and pulse-shape discrimination.

548 All components of the detector, especially the inner components, like the LAr TPC, the SiPM
549 arrays, and cables, must be made from materials of the highest radiopurity to keep backgrounds as
550 small as possible.

551 The veto detector consists of three separate volumes:

- 552 • An inner volume of active liquid AAr, called the Inner Argon Buffer (IAB), surrounding the
553 TPC;

- 554 • A passive shell of acrylic loaded with Gd, called the Gd-loaded Acrylic Shell (GdAS), of octagonal
 555 shape mounted around the IAB. The GdAS surrounds the TPC in all directions (lateral, top
 556 and bottom, with exceptions due to the signal and utility service holes).
 557 • An outer active volume of AAr, called the Outer Argon Buffer (OAB).

558 A copper cage which acts as a Faraday cage provides the optical insulation from the rest of the
 559 AAr external to OAB and, at the same time, it realizes the necessary electric shield for reducing
 560 external noise from contaminating the detector signals. The details of the veto design and expected
 561 performance are given in Sec. 8.

562 In order to demonstrate and test technological developments on a scale relevant to DS-20k,
 563 the collaboration will build and operate a $\sim 1\text{ t}$ prototype. The project is called DarkSide-Proto
 564 (DS-Proto) and is described in Sec. 12. DarkSide-Proto will be at an intermediate scale between
 565 DS-50 and DS-20k, able to test a number of full size components intended for use in DS-20k. The
 566 size of DS-Proto was chosen to be able to validate detector and PDM components, including the
 567 readout system, both from the mechanical and performance aspects of the experiment. The full
 568 size cryogenic system will also be tested in this way, especially the argon condenser, the gas pump,
 569 and the heat recovery system. Functionality and stability control, as well as safety issues during
 570 power failures, purification flow rates and general controls are meant to be explored. DS-Proto also
 571 serves to validate the readiness of the various production lines in the different institutions of the
 572 collaboration to ensure quality control and assurance for the production of components for DS-20k.

573 For the DarkSide-20k detector to reach its physics goals, a comprehensive plan of calibrations for
 574 the LAr TPC and Veto detectors is necessary. The calibration equipment and techniques specific
 575 to the DS-20k experiment are described in detail in Sec. 7. In addition to this, it will be important
 576 to also utilize measurements taken with external calibration experiments placed within the line of
 577 sight of a neutron beam. In the SCENE experiment,[33, 34] a monochromatic, low energy, pulsed
 578 neutron beam at the Notre Dame Institute for Structure and Nuclear Astrophysics was used to
 579 study the scintillation light yield from recoiling nuclei in a small LAr TPC, but only down to
 580 $57.3\text{ keV}_{\text{nr}}$. The ARIS experiment was exposed to the highly collimated and quasimonoenergetic
 581 LICORNE neutron beam at the Institut de Physique Nucléaire d’Orsay (IPNO) in order to study
 582 the scintillation response to nuclear and electronic recoils [35].

583 The collaboration is now expanding this external calibration work with a new external calibration
 584 experiment, the Recoil Directionality (ReD) experiment, described in Sec. 11. The ReD detector
 585 is a small LAr TPC (similar in size to SCENE) equipped with the same SiPM tiles planned for use
 586 in DS-20k. ReD is designed to select and measure single neutron elastic scatters on argon nuclei,
 587 by means of a large acceptance neutron spectrometer, composed of an array of liquid scintillator
 588 detectors. Kinematic requirements of the neutron interactions will allow for the precise detection
 589 of nuclear recoils in the LAr, since the neutron energy, scattering angle, and drift field direction
 590 can all be precisely measured with the use of external neutron detectors.

591

4. PHOTOELECTRONICS

592 Silicon photomultipliers (SiPMs) are one of the key enabling technologies for large-scale LAr-
 593 based dark matter experiments. SiPMs will also play an important role in the next generation of
 594 LAr-based neutrino detectors, such as DUNE [10], and liquid xenon based detectors for neutrinoless
 595 double beta decay, such as nEXO [37]. SiPMs have a number of performance advantages over
 596 traditional PMTs, including higher photon detection efficiency (PDE) and much better single-
 597 photon resolution, all while operating at much lower bias voltage. SiPMs can also be efficiently
 598 integrated into tiles that cover large areas and feature better radio-purity than PMTs.

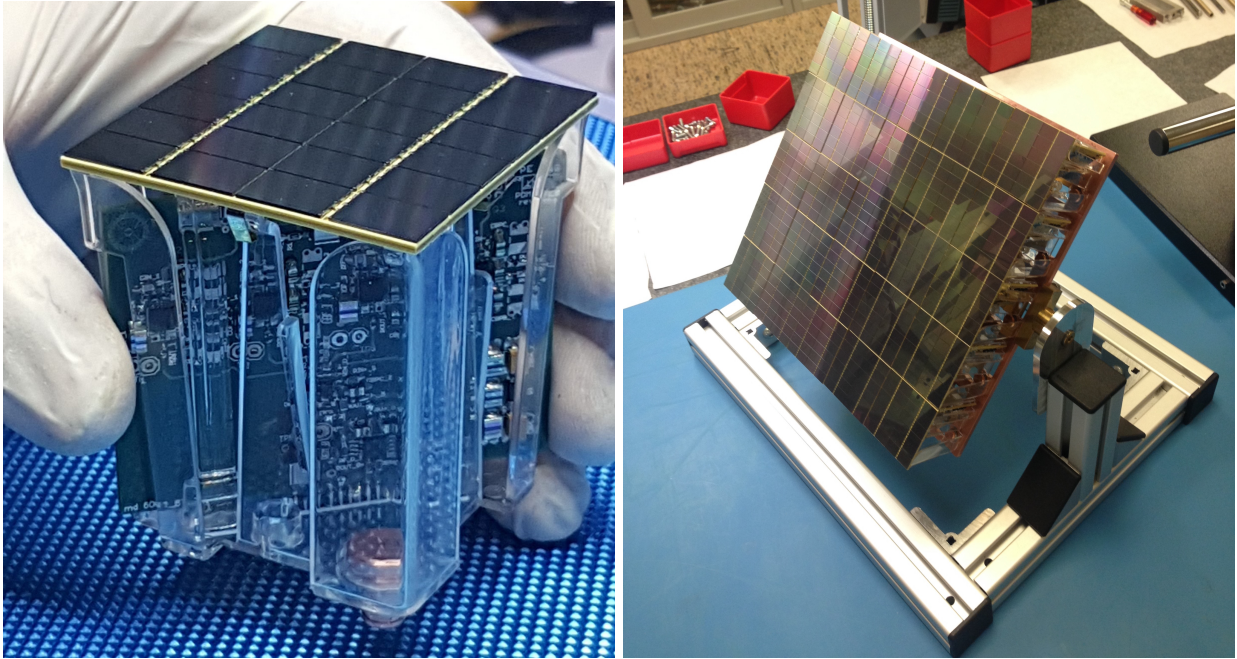


FIG. 5. **Left:** Single channel PhotoDetector Module (PDM) consisting of a $50 \times 50 \text{ mm}^2$ tile of 24 SiPMs and a front-end board. **Right:** The DS-20k motherboard assembled with 25 PDMs.

599

4.1. PhotoDetector Modules (PDM)

600 For DS-20k, the photosensing unit will be a “PhotoDetector Module” (PDM), consisting of a
 601 large tile of SiPMs covering a total area of $50 \times 50 \text{ mm}^2$ operating as a single detector (see the left
 602 panel of Figure 5). Besides the tile, each module will also contain a cryogenic preamplifier board
 603 that will amplify and shape the signal in the immediate proximity of the sensor. The output of
 604 the cryogenic amplifier will be passed on to a signal transmitter, also integrated into the PDM,
 605 and responsible for transmission of the signal through the cryostat penetration. Finally, the PDM
 606 will also include the mechanical structure required to assemble all components and to efficiently
 607 dissipate heat in the LAr target, minimizing the production of bubbles. An intelligent power
 608 distribution system is also foreseen, capable of disabling individual PDMs in case of failure.

609 The unique challenge in readout presented by SiPMs is mainly due to their capacitance. At
 610 50 pF/mm^2 , a single SiPM with a $5 \times 5 \text{ mm}^2$ surface area passes the nF scale for capacitance. Yet,
 611 the experiment foresees a photo-sensing area of 21 m^2 . The readout of a LAr calorimeter faced a
 612 similar challenge, with capacitance for the individual cells often passing the nF scale [51]. Early
 613 developments on LAr calorimeter readout [52–55] demonstrated that the use of a transimpedance
 614 amplifier (TIA) is preferable to a charge integration amplifier where the noise and rise time are
 615 very strongly affected by the large detector capacitance. With this in mind, the DarkSide Collab-
 616 oration has developed and optimized a TIA (schematic is shown in the left panel of Figure 6) with
 617 performance at 87 K in mind [25]. The specific goal was to maximize the amplification factor while
 618 preserving a stable signal bandwidth and SNR.

619 The SiPMs readout scheme strongly affects the PDM performance in terms both of SNR and
 620 bandwidth of the signal. A hybrid readout scheme, with parallel-series combination of SiPMs,
 621 first introduced for the MEG experiment [56, 57], solves at once these two problems. In this
 622 configuration, the output signal of an individual SiPM is reduced by a factor equal to the number
 623 of SiPMs put in series, but this disadvantage is offset by the attenuation of the noise gain due to
 624 the reduction in the input capacitance. Most importantly, a strong improvement of the bandwidth
 625 with respect to the parallel readout scheme is achieved, with six SiPMs easily readout by connecting
 626 in parallel three branches of two SiPMs put in series (known as the 2s3p configuration [26], see
 627 right panel of Figure 6) with a bandwidth comparable to the one achievable with a single SiPM in

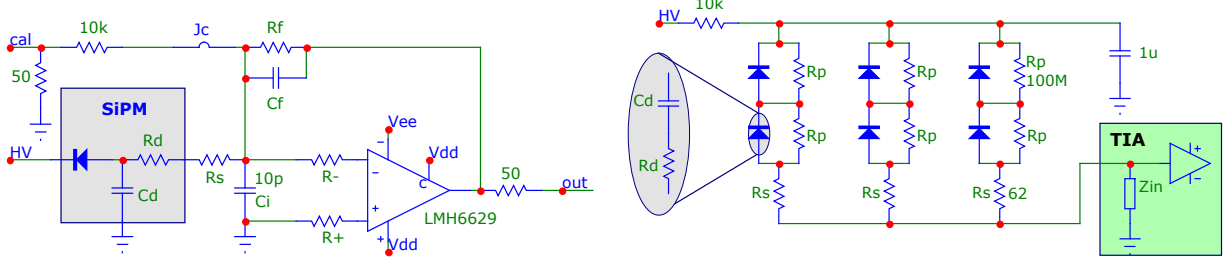


FIG. 6. **Left:** Schematic diagram of the transimpedance amplifier circuit developed to readout SiPMs. **Right:** Schematic diagram of the 2s3p readout scheme optimized for summing six SiPM signal together.

628 input. Four such readout quadrants are fit in a single PDM, with their output signals summed at
629 the transmission stage.

630

4.2. Signal Transmission

631 The signal transmission from the PDMs to the warm electronics is of primary importance for
632 the experiment. Given the high number of independent channels, cables would introduce a large
633 mass in the cryostat with the inherent problems of radio-purity and heat load. The delivery of the
634 PDM signals to the outside world through optical fibers will solve at once these two problems. For
635 this purpose an optical analog cryogenic transmitter has been developed. The prototype boards
636 of the opto-link system (optical driver and optical receiver board) have been recently produced.
637 The optical receiver board (32 channels) was successfully tested, while the optical driver board (25
638 channels) is at the moment undergoing testing.

639 The PDMs will be located above the anode and below the cathode, fully covering the top and
640 bottom faces of the LAr TPC active volume, to detect both the S1 and S2 signals with high
641 efficiency. The top and the bottom photon readout assemblies will consist of 4140 PDMs each.
642 Multiple PDMs are mounted to a single motherboard to form two larger basic mechanical units
643 called the square board (SQB) and the triangular board (TRB), described in Sec. 5.5.1 and shown
644 in Figure 12. The SQB and TRB have the same edge size of 25 cm. The SQB and TRB are then
645 used to form the full readout planes (shown in Figure 11). The total number of readout channels
646 (top and bottom) is 8280.

647

4.3. PDM Fabrication and Characterization

648 Following the successful construction of the first Photo-Detector Module (PDM) in March 2018,
649 the Photo-Electronics Working Group proceeded to the construction of the first Motherboard,
650 shown in Figure 5. The FBK company delivered two SiPM runs: the first one with standard doping
651 SiPMs (cell size $25 \times 25 \mu m^2$ and quenching resistor $10 M\Omega(77 K)$) and the second one with triple
652 doping SiPMs (cell size $30 \times 30 \mu m^2$ and quenching resistor $5 M\Omega(77 K)$). Since the latter SiPM type
653 is considered the best candidate for the DS-20k experiment, we decided to use the single doping
654 SiPMs for the first Motherboard construction, so that the triple doping type could be mounted
655 later, taking advantage of the experience gained with the mounting of the first Motherboard.

656 This SiPM run was characterized by a reasonable yield at $-40^\circ C$ of about 50 %. A detailed
657 inspection of the SiPM quenching resistor (R_q) showed good uniformity for most of the wafers,
658 while the first and the second wafers (W1,W2) had a 20 % larger R_q (see Figure 7). The optimal
659 working voltage of the SiPM is expected to change as a function of R_q , so in the forthcoming
660 mass production by the LFoundry company, where hundreds of 8 " SiPM wafers are scheduled,
661 this quenching resistor spread is not an issue since the SiPMs with similar R_q can be paired. In
662 this way, each Motherboard, with PDMs biased at the same voltage, will be made of devices with

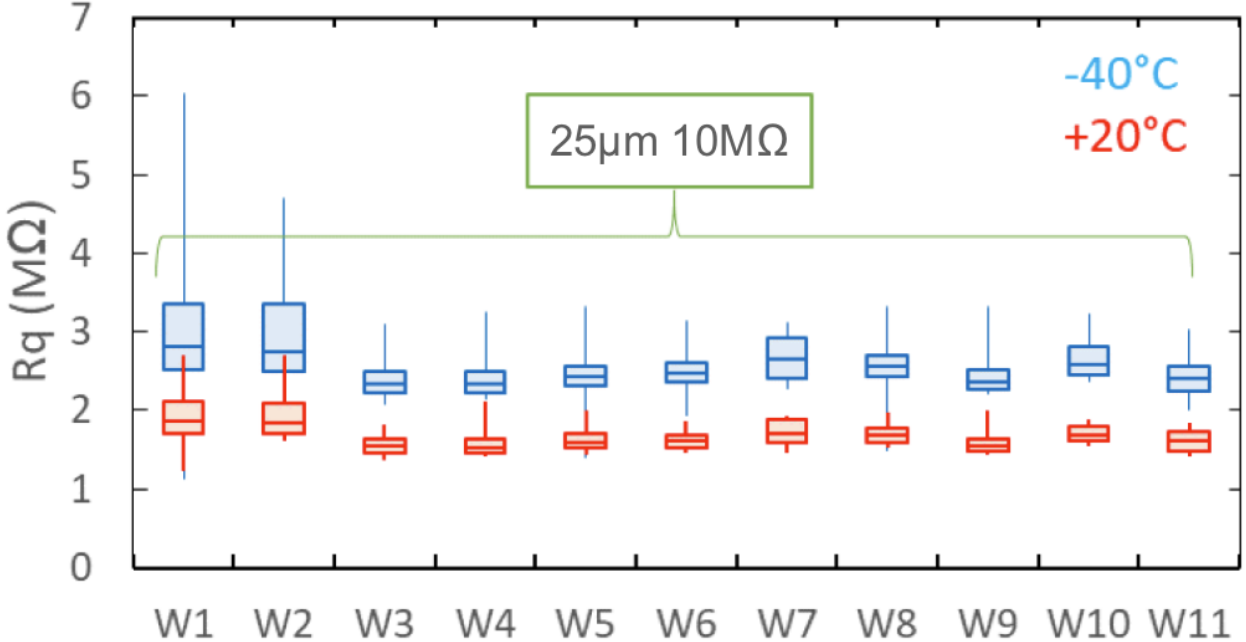


FIG. 7. Average SiPM quenching resistor value vs. wafer number measured at 20 °C and -40 °C.

similar R_q . Due to the limited SiPMs available in the present production we had to use all of them to make the first Motherboard, and thus all were biased with a common voltage despite the slight difference in R_q . As a consequence, the tiles made with SiPMs belonging to wafers 1 and 2 were fed with an overvoltage lower than the optimal one for some of the SiPMs, i.e. 5 V. It is worth noting that a dedicated facility for the Motherboard production is not available yet, and therefore the use of equipment through outsourcing and additional man power was therefore required.

The tile and the Front-End Board PCBs were made with an Arlon 55-NT substrate, following the experience gained during the first PDM construction. The electronic components were mounted with outsourced equipment, under the supervision of LNGS personnel. The tile PCBs were tested both at warm and at cryogenic temperatures to verify the correct circuit impedance. After the wafer dicing, the SiPMs were shipped from FBK to Princeton University, where the first Motherboard tiles were bonded by personnel from LNGS, Princeton University and TIFPA. A cryogenic epoxy for the SiPM back-side and a wire-bonding connection for the front-side was used. The 27 tiles, each made of 24 SiPMs, were then shipped to LNGS, using multipurpose acrylic boxes, designed by the Pisa group. This box allows for safe shipping of the tile, offering an adequate protection of the SiPM wire bonding and, at the same, time allows the tile characterization in liquid nitrogen by permitting the insertion of the Front End Board without removing the tile from the box. The tiles underwent a comprehensive test at LNGS both at warm temperature and in LN, including the reverse I-V curve measurement, the power spectrum and the charge spectra. We found just one tile out of the 27 with two SiPM branches (4 SiPMs) not working properly. Another tile showed a noise level higher than the average. These two tiles were therefore excluded from the list of the tiles selected to populate the first Motherboard.

As an example, the left side of Figure 8 shows the tile I-V curves taken at 77 K, indicating a homogeneous behavior.

The right panel of Figure 8 shows the signal to noise ratio (SNR) for the 27 tiles at their optimal voltage. It is worth noting that all of them have a SNR larger than the minimum SNR of 8, required by the DarkSide-20k experiment specifications. For each tile, the SNR was obtained relying on several different procedures and analysis methods. The bar length in the figure represents the spread of each measurement, depending on the method used. The signal-to-noise ratio (SNR) is defined as the ratio between the gain and the width of the baseline noise peak. The gain is measured by fitting the center values of the amplitude multiple peaks and evaluating the slope of a

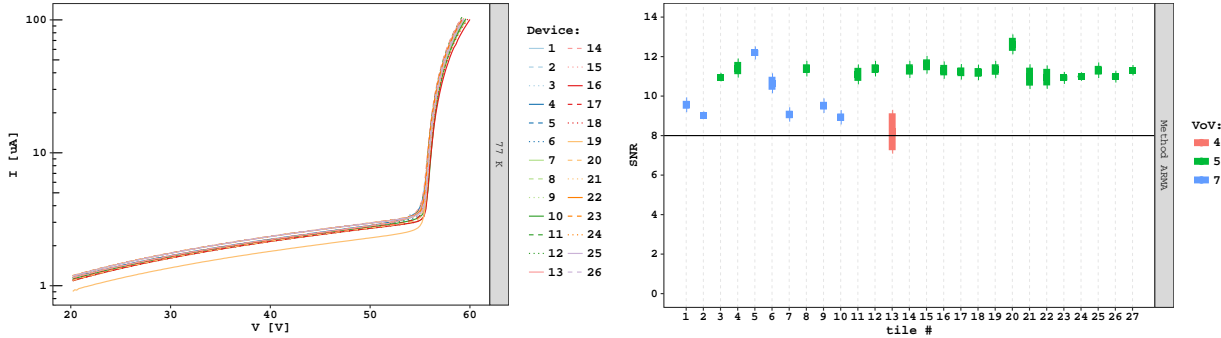


FIG. 8. **Left:** Reverse I-V curves for the SiPM tiles measured at 77K. **Right:** SNR of the 27 bonded SiPM tiles.

linear fit. The baseline noise is extracted from the average standard deviation of the waveform in a pre-pulse window, 500 ns long, using 500 samples. For most tiles, the distribution of the standard deviation is not symmetric around the peak. The most important contribution to the noise baseline is the presence of one or more photoelectrons not stimulated by the laser pulse. These can originate from a SiPM having an excess of dark-rate or more probably by an excess of after-pulsing.

Since the distribution is not symmetric, the estimate of the baseline noise is intrinsically biased and two options are possible, corresponding to the mean value or the most probable value (mode). Consequently the SNR is defined in a confidence interval between $\text{SNR}_{\min} = \text{gain}/\text{noise}_{\text{mean}}$ and $\text{SNR}_{\max} = \text{gain}/\text{noise}_{\text{mode}}$.

Figure 9 shows the SNR obtained with the common over-voltage of 5 V. Although a few tiles, as expected, manifest a SNR slightly below 8, the SNR is quite good for all tiles used in the assembly of the first Motherboard.

706

4.4. Motherboard Assembly

707 Before assembling the first Motherboard, a full mock-up made of an aluminum Motherboard
 708 structure, an FR4 Motherboard strip PCB, 25 dummy tiles and FEBs, and the PDM acrylic
 709 mechanics was mounted at Bologna. Each PCB had the same dimensions of the final one, while
 710 the HV/LV and signal layers were not included in the stack-up. The mounting required just a few
 711 hours and the overall procedure was validated, while the mechanics of the different components
 712 nicely merged, suggesting just a few minor mechanical improvements.

713 After these tests, the tiles were finally shipped to Pisa, while the PDM pillars and the copper
 714 Motherboard structure were milled at Bologna using 99.997% pure copper sold by the Luvata
 715 Company. The first Motherboard was equipped with a PCB strip connecting the PDMs, made of
 716 a thin stack-up (0.5 mm) based on a Pyralux substrate and shipped to Pisa to start the mounting
 717 of the 25 PDMs on the Motherboard.

718 The PDMs were assembled in the Pisa clean room, following the prescriptions used for the first
 719 PDM, assembled in March 2018. The mounting of the 25 PDMs on the Motherboard was finalized
 720 in few days. A picture of the first Motherboard, fully equipped with the first 25 PDMs is shown in
 721 the right panel of Figure 5.

722 In summary the construction of the first Motherboard required the production, testing, selection
 723 and bonding of more than 600 SiPMs. Although a cryogenic probe and an automatic bonder were
 724 not available yet, the Collaboration was able to increase the number of successfully built PDMs
 725 from 1 to 25, in just 6 months. The bonding yield exceeded 95% (just 1 tile out of the 27 showed
 726 problems with the SiPM bonding strategy), while the satisfactory PDM SNR demonstrated the
 727 validity of the full Motherboard construction process.

728 After the completion of the first motherboard, equipped with 25 PDMs each containing 24 single
 729 dose SiPM's, the collaboration moved to the construction of a second Motherboard, equipped with
 730 triple dose SiPMs. At the moment, half of the PDMs have already been assembled and mounted

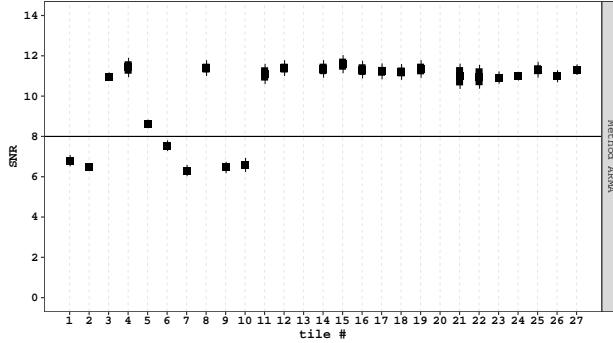


FIG. 9. SNR of the 25 SiPM tiles populating the first motherboard while. Data were recorded while operating the SiPM tiles at an over-voltage of 5 V.

731 in the copper structure. The remaining PDMs will be mounted within the summer of 2019. The
 732 FEBs were already successfully tested, while the SiPM tiles are currently undergoing testing in
 733 LN. The next step in the photo-electronics schedule is the production of about 400 PDMs for the
 734 DS-Proto detector. These SiPMs will be produced by the LFoundry Company in Avezzano, Italy.
 735 The first run is expected in the summer of 2019.

736

4.5. Mass Production

737 The first engineering run, finalized in September 2018 and tested shortly after, showed the
 738 capability of the silicon foundry to implement the FBK technology. The produced SiPMs showed
 739 good performance at both room temperature and in liquid nitrogen. A second LFoundry engineering
 740 run, presently ongoing, is devoted to the development of the through silicon vias (TSV). This post-
 741 production rework requires some delicate mechanical manipulation of the SiPM wafers.

742 The DS-20k SiPM packaging foresees the production of more than 10 000 PDMs in 2.5 yr. This
 743 remarkable effort requires a large clean room, relying on cutting edge technology equipment and
 744 trained personnel. The GADMC selected for the NOA DS-20k SiPM packaging facility a clean room
 745 at the *Tecnopolo dell'Aquila*, with surface exceeding 700 m². The clean room will be soon refurbished
 746 to comfortably host the needed equipment and personnel. This facility will be managed by GSSI,
 747 through an agreement with INFN that will soon be finalized. Concerning the procurement of the
 748 equipment for the DS-20k PDMs mass production, the cryogenic probe tender was just approved
 749 by the INFN Executive Board and the flip-chip bonder tender will follow in the weeks to come.

750

5. INNER DETECTOR AND CRYOGENICS SYSTEM

751

5.1. DS-20k LAr TPC

752 The DarkSide-20k LAr TPC is the dark matter detector and the central element of the experimen-
 753 t, with all auxiliary detectors and systems specified and designed in support of it. The DS-20k
 754 LAr TPC will use 50 t of LAr extracted from an underground source as the target material for
 755 WIMP detection. An ultra-pure acrylic vessel is used to contain the LAr. Features directly fabri-
 756 cated onto the inner surfaces of the acrylic vessel will form the TPC itself. These feature are the
 757 TPC field cage system, the anode and the cathode and are implemented on the acrylic panels with
 758 a commercial conductive polymer coating, called Clevios™. Use of this coating eliminates the use
 759 of metal conductive materials.

760 The same pure acrylic material, in the form of 4 mm thick sheets, is used to hold the Enhanced
 761 Specular Reflector (ESR) reflector foils installed to maximize light collection. The TPC is designed
 762 such that all the inner surfaces facing the active volume are coated with TPB, a wavelength shifter,

DS-20k TPC Dimensions	
TPC Drift Length	350 cm
Octagonal Inscribed Circle Diameter	355 cm
Total LAr Mass	51.1 t
Active LAr Mass	49.7 t
Fiducial Cut Distance (vertical)	70 cm
Fiducial Cut Distance (radial)	30 cm
Fiducial LAr Mass	20.2 t
Nominal TPC Fields and Settings	
Drift Field	200 V/cm
Extraction Field	2.8 kV/cm
Luminescence Field	4.2 kV/cm
Cathode Voltage	-73.8 kV
Extraction Grid Voltage	-3.8 kV
Anode Voltage	ground
Gas Pocket Thickness	7 mm
Grid Wire Spacing	3 mm
Grid Optical Transparency	97 %
SiPM PDM	
Number of PDM on TPC Top	4140
Number of PDM on TPC Bottom	4140
PDM Effective Area	50 × 50 mm ²

TABLE II. DS-20k LAr TPC detector parameters.

763 to ensure the complete conversion of the 128 nm argon scintillation light to 420 nm, where the
 764 SiPMs' peak in their PDE. Two identical photosensor arrays of 4140 channels each are placed on
 765 top and bottom of the TPC, but outside of the acrylic vessel. The TPC is mounted inside a neutron
 766 veto detector, whose most important component is a 10 cm thick, gadolinium loaded, acrylic shell
 767 that completely encapsulates the TPC. This plastic shell defines two 40 cm thick active volumes,
 768 respectively named the inner and outer buffer, filled with liquid AAr. The buffers are further
 769 segmented with ESR, also coated with TPB. The whole apparatus is placed inside a light and
 770 electromagnetic shield barrier, contained in the ProtoDUNE-like cryostat filled with AAr.

771 **Sealed PMMA Vessel:** An acrylic (PMMA) vessel will be used to confine the UAr rather than
 772 a metallic vessel, since PMMA is extremely radiopure, resulting in a residual neutron background
 773 estimated to be $<10^{-3}$ for the exposure of 200 t yr. As described above, the TPC active volume is
 774 confined in all directions by the sealed PMMA vessel that is formed by bonded plates or panels.
 775 In order to use the UAr more efficiently, all the UAr will be sealed in this PMMA vessel, so that
 776 no other external vessel will be required (as shown in Figure 10). The body of the PMMA vessel
 777 will be fused together by 5 cm thick acrylic plates, and then flanged and sealed with the top and
 778 the bottom lid, that serve as the anode plate and cathode plate of the TPC, respectively.

779 The ESR-acrylic reflector panels are located inside the acrylic vessel. The top and bottom PDM
 780 arrays are placed outside of the acrylic vessel, immersed in the AAr of the neutron veto detector.
 781 PDM arrays will be isolated from any light generated in the veto detector. In this way, 97.3 % of
 782 the total argon is active, resulting in the most efficient usage of UAr. All cables, HVFTs, and most
 783 mechanical structures are moved outside of the UAr volume as well, resulting in less outgassing
 784 and hence higher purity of the UAr.

785 The HV Cathode connection through the acrylic vessel is being studied and a new design will be
 786 tested to adapt the cable connection to the cathode itself. The acrylic vessel design integrates the
 787 HV connection so that the contact point is outside the vessel. In this case, both the HV cable and
 788 the HVFT are in the AAr volume. The HVFT will penetrate through the veto cryostat.

789 A commercial conductive and transparent Polymer coating, Clevios™, is found to be a very
 790 promising alternative to the traditionally used indium tin oxide (ITO) thin film coating. Clevios™
 791 is being used in industrial applications such as transparent electrodes for touch panels and printed
 792 electronics. The main advantage of Clevios™ is its composition. Being a water-based solution, the
 793 large-area coating needed for the anode and cathode will be easier to accomplish with respect to an

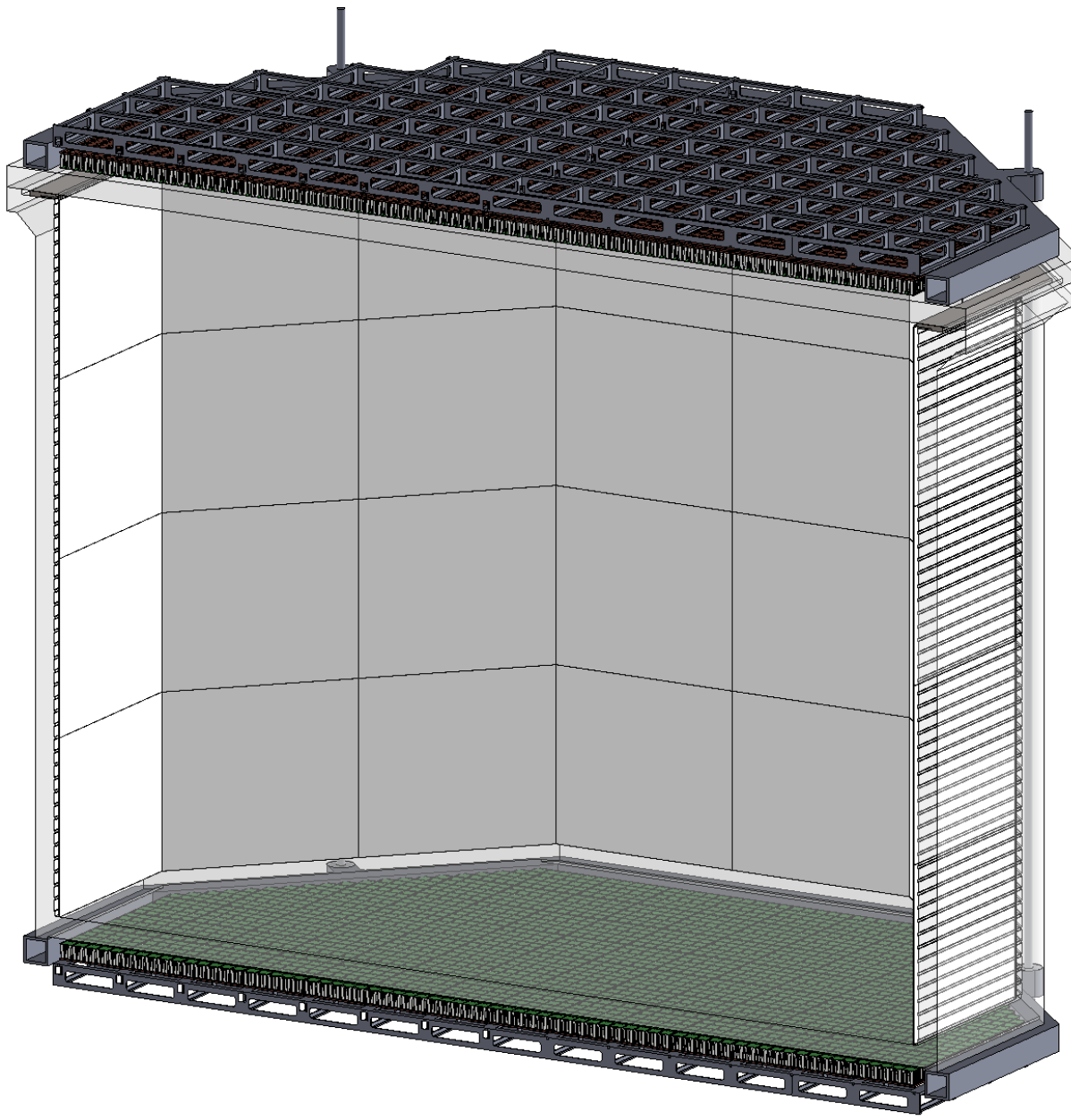


FIG. 10. Artist rendering of the PMMA vessel and the TPC.

794 ITO coating. A sample of 100 g has been procured for the radioactivity assay. The initial ICP-MS
 795 assay results from PNNL are encouraging, and further analysis of Rn emanation is scheduled at
 796 Krakow. In terms of the optics, three coating samples of CleviosTM on acrylic plates were provided
 797 by The Heraeus Company. The wet coating thickness of each sample is 4 μm , 8 μm and 12 μm ,
 798 respectively, and their transparency has been measured at Princeton University. A 1.5 % absorption
 799 at 420 nm was observed for a 4 μm thick CleviosTM layer, which is a good result comparable to
 800 the 98 % transparency of ITO measured in DS-50. Further studies, including coated thickness
 801 resistivity, TPB coating on CleviosTM, and durability in LAr are ongoing. Besides the anode and
 802 cathode, the new design replaces the bulky copper field shaping rings with CleviosTM conductive
 803 coatings. Consequently, the use of this polymer will reduce the expected background, as well as
 804 the total cost, and make the fabrication and installation of the TPC simpler.

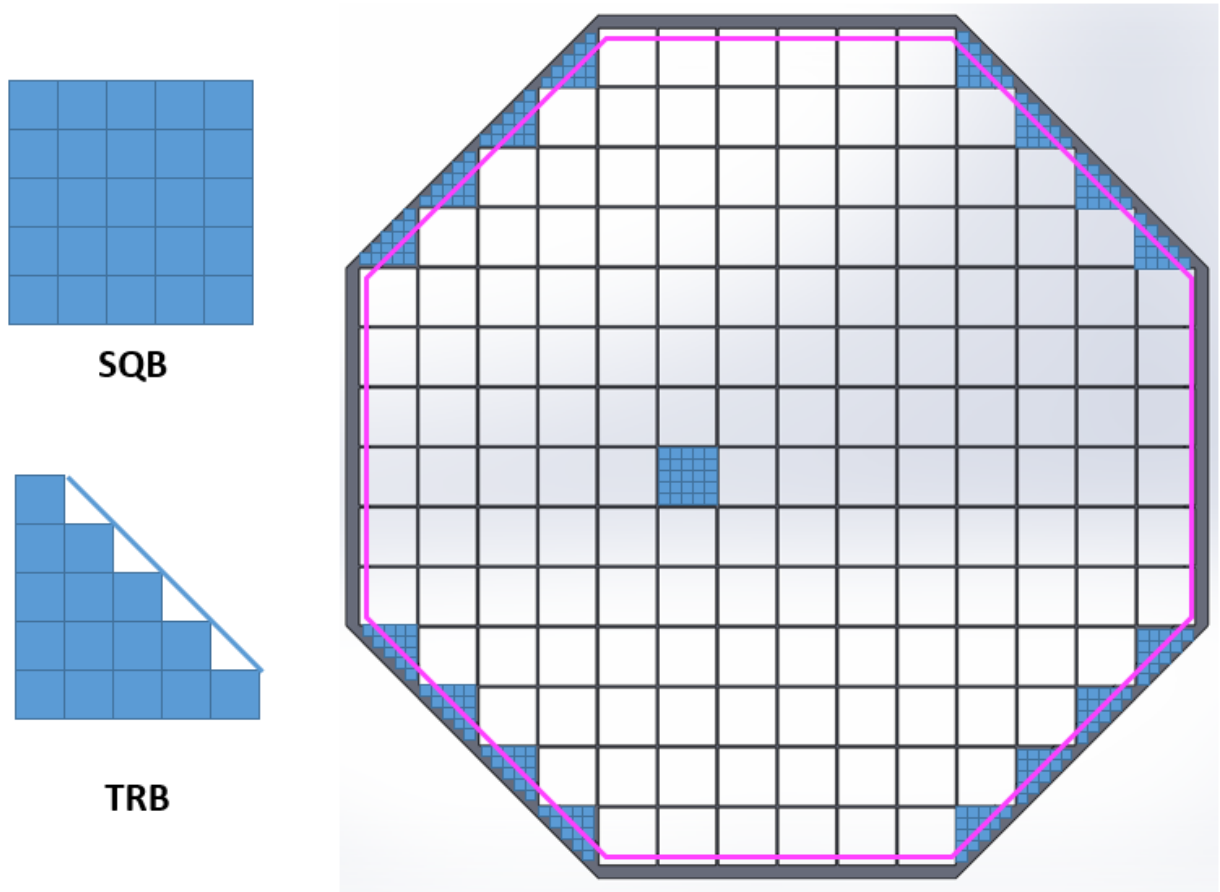


FIG. 11. Patterning scheme for the PDMs. Pink lines indicate the edges of the TPC active volume.

LArTPC Size Consideration: Since the SiPM tiles are all square shaped, the DS-20k TPC will be an octagonal shape to best fit the coverage of the PDM, while optimizing the fiducial mass. The size of the TPC is determined by the patterning strategy of the SiPMs, driven by the design size of the square and triangular motherboards (SQB and TRB, respectively). Figure 11 shows the current SiPM pattern strategy for both the top and bottom arrays. Each array consists of 156 SQBs and 16 TRBs. Each TRB contains 15 PDMs and each SQB contains 25 PDMs, as shown in Figure 12. Thus, the number of PDMs used in each array is 4140, while the total number envisioned in the TPC is 8280. Based upon this pattern strategy, and considering that the edge of the active volume of the TPC will shrink about 2.7 cm from the edge of the SiPM array, the distance from edge to edge of the octagonal active volume will be 355 cm. The height of the TPC will be 350 cm. With this design, the total mass of LAr in the active volume and fiducial volume (with 70 cm vertical and 30 cm lateral cuts) are 49.7 t and 20.2 t respectively.

Reflector Panel: In order to get rid of the conventional PTFE reflectors, which would be the predominant source of neutron background and Cherenkov background due to the enormous mass required for DS-20k, ESR foils will be used as the TPC reflector. The ESR is a thin layer foil which has reflectivity of 98 % for 420 nm light, with a thickness of only 50 μm . In order to hold the ESR foils in place and maintain their flatness during the operations, 4 mm thick UVT acrylic sheets will be used. The thickness of the backside acrylic sheet is chosen to be 4 mm, providing the panels with enough strength to maintain the flatness of the ESR foils. The surface of each ESR foil facing the active LAr volume will be coated with TPB.

The entire reflector panel of the TPC is shown in Figure 13. The ESR mountings are strategically arranged such that no gaps can develop during the cool down of the TPC, hence guaranteeing 100 %

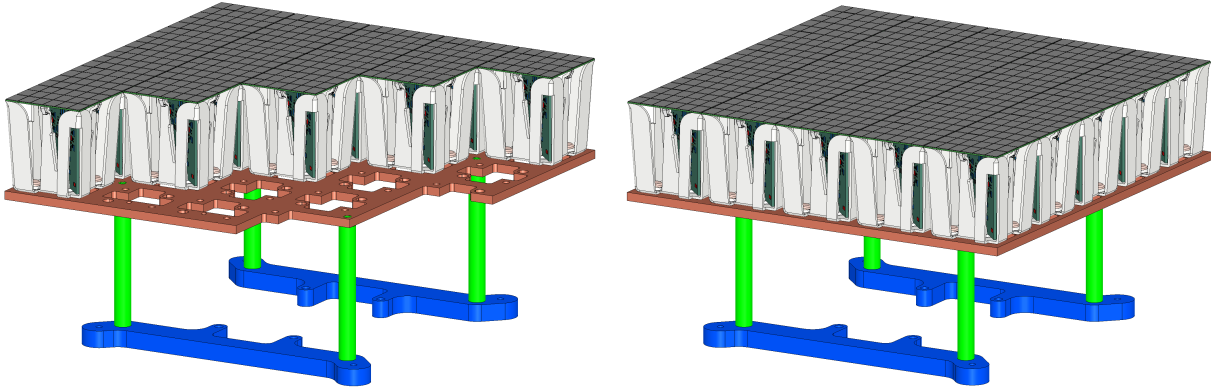


FIG. 12. Schematic drawings of the two types of DS-20k PDM motherboard arrangements. **Left:** triangular with 15 PDMs arranged for center and edge placement. **Right:** square with 25 PDMs.

TPB coverage. Each ESR-acrylic sub assembly will be fixed by several acrylic screws, with the screw heads facing the active volume. To avoid losing any light, each head of the screw will also be coated with TPB. By design, some space is left between the acrylic and the ESR to allow venting of any gas during the filling with LAr, but also to allow the LAr to fill the space between the back of the ESR and the acrylic panel. The flat and corner assemblies will be mounted on the field cage, which is attached to another set of acrylic structures by PTFE screws. The ESR holding panels are not connected at the corners in order to accommodate the shrinkage when the assemblies are cooled to LAr temperature. Overlaps between ESR foils at each joint are also designed for the same reason. A small mock-up to mimic the shrinkage has been built at UC Davis, whose results have confirmed the design concept. Repeated tests in liquid nitrogen showed that all parts moved in the desired way during cooling down and warming up, which proves the design idea.

Field Region: Within the sealed acrylic vessel, the electrode features of the TPC are realized using the CleviosTM conductive polymer coated directly onto the acrylic vessel. The inner surface of the acrylic vessel will be machined with grooves such that recessed areas have geometries similar to an electrode ring, and when coated with the CleviosTM comprise the TPC field-shaping rings that are highly uniform across the height of the TPC.

The relative permittivity of LAr and GAr are 1.54 and 1.03, respectively. By applying electric potentials of zero, -3.8 kV , and -73.8 kV to the anode, extraction grid and cathode, respectively, three different field regions are formed in the TPC:

- The uniform drift field of 200 V/cm in the liquid phase, formed by the geometry of the field cage. The drift distance between the cathode CleviosTM layer and the extraction grid is 350 cm ;
- The extraction field in the liquid phase above the grid is 2.8 kV/cm . The distance between the extraction grid and the surface of the LAr is 3 mm ;
- The electroluminescence field in the gas phase is 4.2 kV/cm . The gas gap between the surface of the LAr and the CleviosTM layer acting as the anode is 7 mm thick.

These values are based on the settings used for DS-50, while since the DS-20k gas pocket will be operating at a higher pressure, the extraction and luminescence fields will be scaled by the ratio of the electric field to the pressure of the gas pocket. The final values to be used will be confirmed with the DS-Proto detector that is designed to confirm final design choices for the DS-20k LAr TPC.

As the top boundary of the active volume, a 5 cm thick acrylic window serves as the diving bell to maintain a stable gas pocket. A thin layer of CleviosTM conductive polymer is coated on the inner surface to act as the anode and a layer of TPB coated onto the CleviosTM layer to shift the scintillation light wavelength. The CleviosTM layer coating geometry is optimized for gas pocket electroluminescence field uniformity, as shown in the left panel of Figure 14. Right below the liquid surface is the extraction grid, composed of stainless steel wires (not shown in figure) stretched in parallel with 3 mm spacing and held in place via small posts set into a stainless steel frame. Slots going in the radial direction and on the rim of the acrylic diving bell act as a concentric guide, to compensate the different thermal expansion coefficients between the acrylic and stainless steel

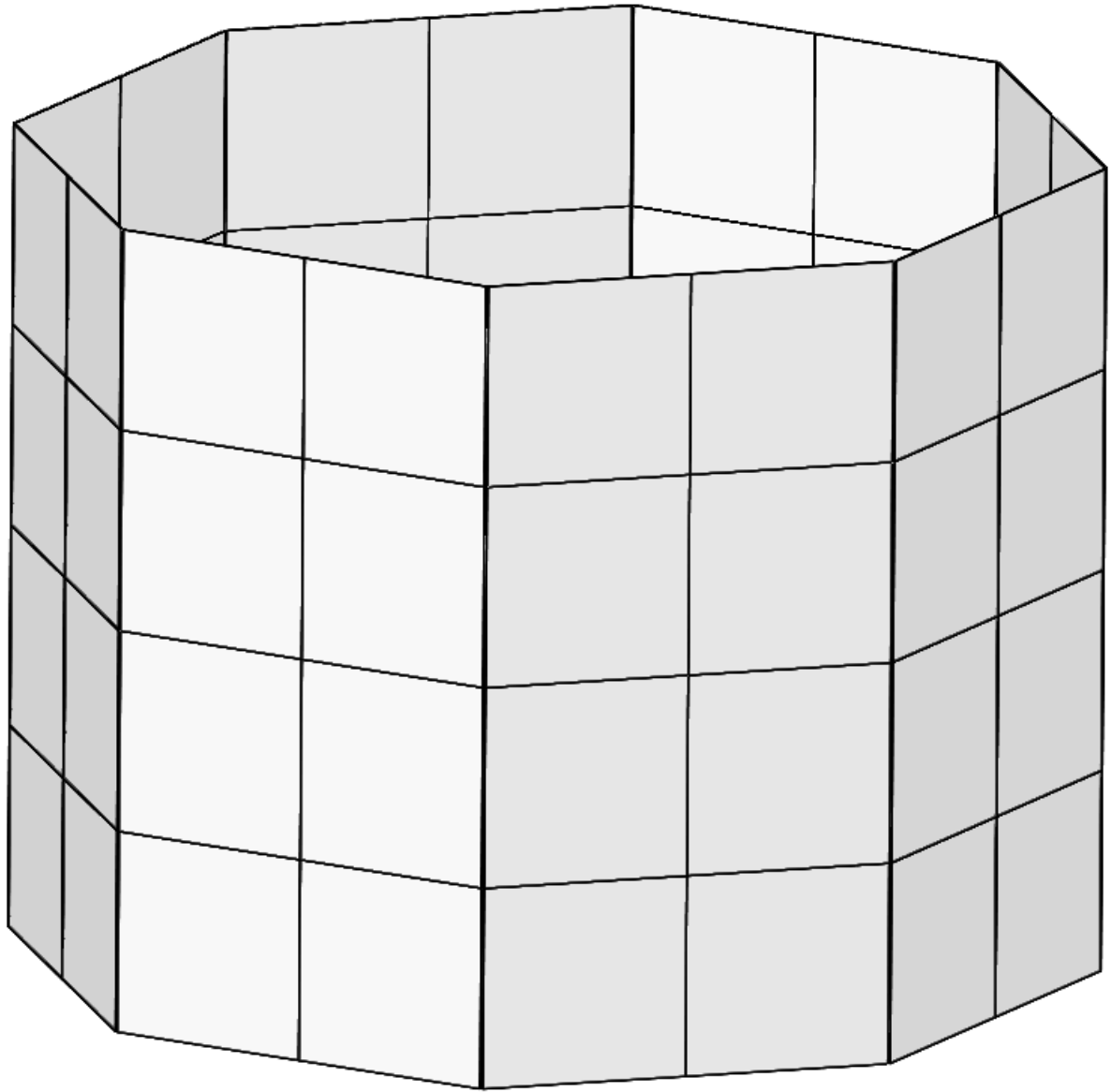


FIG. 13. 3D model of the full DS-20k LAr TPC reflector panels system.

865 while maintaining precise alignment. The LAr level will be maintained at the top surface of the grid
 866 frame. Suitable tensions will be pre-loaded on each of the grid wires to minimize the sagging, an
 867 effect that would distort the electroluminescence field. The frame must be stiff enough to sustain
 868 the total tension load of all wires, while having as little mass as possible. Both simulation studies
 869 and prototyping tests are well underway and have presented a feasible design for the extraction
 870 grid.

871 The bottom boundary of the active volume, shown in the right panel Figure 14, is a 5 cm thick
 872 acrylic window coated with a thin layer of CleviosTM on both sides. A layer of TPB will be coated
 873 on the top CleviosTM layer for wavelength shifting. The edge of the top CleviosTM layer is in
 874 contact with a C-profile feature on the walls of the acrylic vessel, which acts as a field shaping
 875 ring and smooths the electric field lines in the corner of the cathode region. Similarly, the bottom
 876 CleviosTM layer is in contact with a smoothing-profile solid guard copper ring to provide connection
 877 for the ground bias and electric field minimization. The 5 cm thick acrylic window can easily sustain

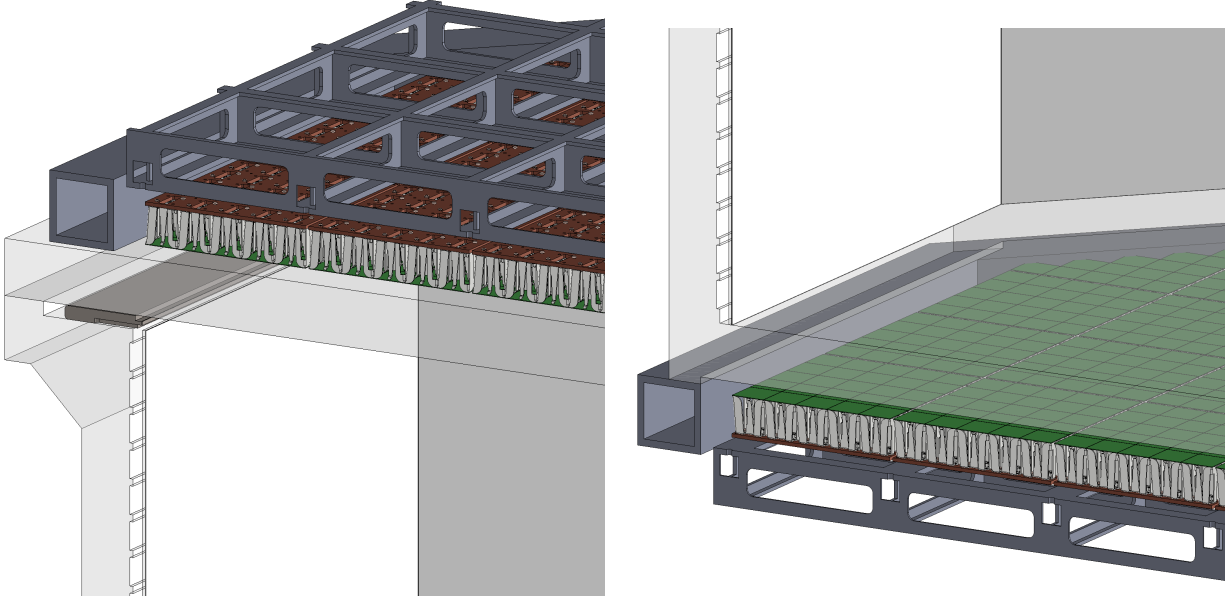


FIG. 14. **Left:** 3D model of the LAr TPC anode and extraction grid region. **Right:** 3D model of the LAr TPC cathode region.

878 the applied electric field with this design. Figure 15 shows the full field mapping modeled with
 879 the COMSOL Multiphysics software. Since the vessel is sealed, there is no path for HV to break
 880 through the acrylic at the cathode region. To confirm this, a full scale mock-up will be built to
 881 confirm the cathode HV delivery method around the acrylic vessel bottom. The bottom surface of
 882 the cathode acrylic window will have a convex shape to avoid bubble accumulation. Any bubbles
 883 generated by the bottom photon detector array, or any other parts, will be driven outwards and
 884 rise to the top of the AAr cryostat.

885 A one tonne-scale prototype with full features of the DarkSide-20k TPC will then be built to
 886 validate the design comprehensively. General considerations, such as the requirements of surface and
 887 bulk contamination, coating procedures, handling and bonding of acrylic, are based on knowledge
 888 available within the GADMC. Detailed plans and procedures are currently being developed. All
 889 mock-up designs and tests will use final DS-20k geometries and full size components in order to
 890 confirm the validity of the final DS-20k mechanical design and functional parameters. The DS-20k
 891 LAr TPC parameters are summarized in Table II.

892 5.2. Cryogenics

893 The main system parameters of the cryogenics system are given in Table III. The parameters
 894 that are listed in bold are considered to be system requirements, most often driven from experience
 895 gained during operations of the DS-50 cryogenics system.

896 The cryogenics system is derived from the successful scheme of the DS-50 cryogenics and gas
 897 handling system. Additional lab tests, already performed over the past 4 years, demonstrated
 898 individual or integrated features required for the performance of the control system and the safety
 899 of the large amount of UAr in the DarkSide-20k system. A full P&ID diagram is already developed
 900 as shown in Figure 16. There are two major linked systems: one for the AAr in the veto shield
 901 inside the ProtoDUNE cryostat and one for the UAr in the sealed acrylic vessel for the LAr TPC.
 902 The AAr cryogenics system can be the same as the demonstrated ProtoDUNE system already
 903 built at CERN, or an optimized version specific for the LNGS installation. The UAr cryogenics
 904 system for the TPC will be an upgraded system based on DS-50. The ProtoDUNE cryostat is a
 905 passively insulated system so that its thermal load is not subject to the availability of the electric

Parameter	Value
ProtoDUNE Cryostat parameters for AAr	
ProtoDUNE Cryostat inner width	8548 mm
ProtoDUNE Cryostat inner height	7900 mm
LAr height in ProtoDUNE Cryostat	7500 mm
Total AAr in ProtoDUNE Cryostat	700 t
ProtoDUNE Cryostat insulation per unit area	6.5 W/m ²
Thermal Heat Load of ProtoDUNE Cryostat	2.7 kW
TPC PDM Cold Electronics Power	1.5 kW
Veto PDM Cold Electronics Power	0.5 kW
AAr System Design Mass Circulation Speed	10 000 std L/min
Minimum heat recovery efficiency of AAr heat exchanger	>95 %
AAr Turn Over Time	30 d
Total Cooling Power Required	10 kW
LAr boiling threshold at 3 m depth	60 mW/cm ²
Minimum AAr condenser cooling power to hold LAr inventory	2.7 kW
ProtoDUNE AAr top pressure	1.075 bar
TPC Cryogenics Parameters for UAr	
Total UAr mass during normal operation	51.1 t
TPC UAr Cryogenics Design Mass Circulation Speed	1000 std L/min
Minimum heat recovery efficiency of UAr heat exchanger	>95 %
UAr Turn Over Time	20 d
Total Cooling Power Required for UAr	500 W
UAr Turn Over Time	20 d
UAr electron lifetime required for stable S2 generation	>5 ms (<0.01 ppb O ₂ equiv.)
Pressure stability achieved in DarkSide-50	0.023 psi (RMS)
Nominal flow rate of single DarkSide-20k GAr circulation pump	500 std L/min
Total mass of LN ₂ storage in cooling system	30 t
Efficiency of radon purification by activated charcoal trap	<2 μ Bq/kg after trap
Maximum required helium leak rate at all welds and joints	2×10^{-9} std cm ³ /s

TABLE III. DarkSide-20k cryogenics system parameters.

power. Liquid nitrogen is the primary cooling source of the entire cryogenics system. A minimum storage of the liquid nitrogen is maintained such that the system will be protected during power failure mode. A full scale version of the condenser box for the underground argon has already been designed and all parts procured. The cryogenics test of the condenser is planned at the CERN cryogenic division in summer 2019.

Heat exchangers are strategically placed throughout the system for LAr filling and LAr removal at the various required speeds for the different operational modes. The continuous argon circulation for purification is driven by a set of specialized gas argon pumps (developed within the collaboration). Combined with the integrated heat exchanger systems, the system can handle high circulation rates (10 000 std L/min AAr, and 1000 std L/min UAr) drawing either, or both, liquid and gas phase argon to effectively remove electronegative impurities. The designed P&ID system allows the use of SAES hot getter to effectively remove N₂, CO₂, and O₂. The total cooling power of the cryogenics system is designed to handle the total heat load from the power dissipated by the cold electronics operating inside the liquid argon volume.

The cryogenics system for the LAr TPC in DS-20k shares the same principle as that fully demonstrated in DS-50, which has been running smoothly for five years. The long-term TPC pressure stability, an essential parameter for S2 resolution, has been achieved with incredible success, quantified as 0.023 psi RMS. A drift electron lifetime of \geq 5 ms has been achieved, resulting in an oxygen contamination in LAr of less than 0.01 ppb, which is greatly beneficial to the low-mass dark matter search, as recently published in [7, 8]. The immunity to total power failure (including UPS system failure), as tested in the commissioning phase and verified by a recent accident of total LNGS blackout, secures the safety of the entire LAr TPC, especially the valuable UAr.

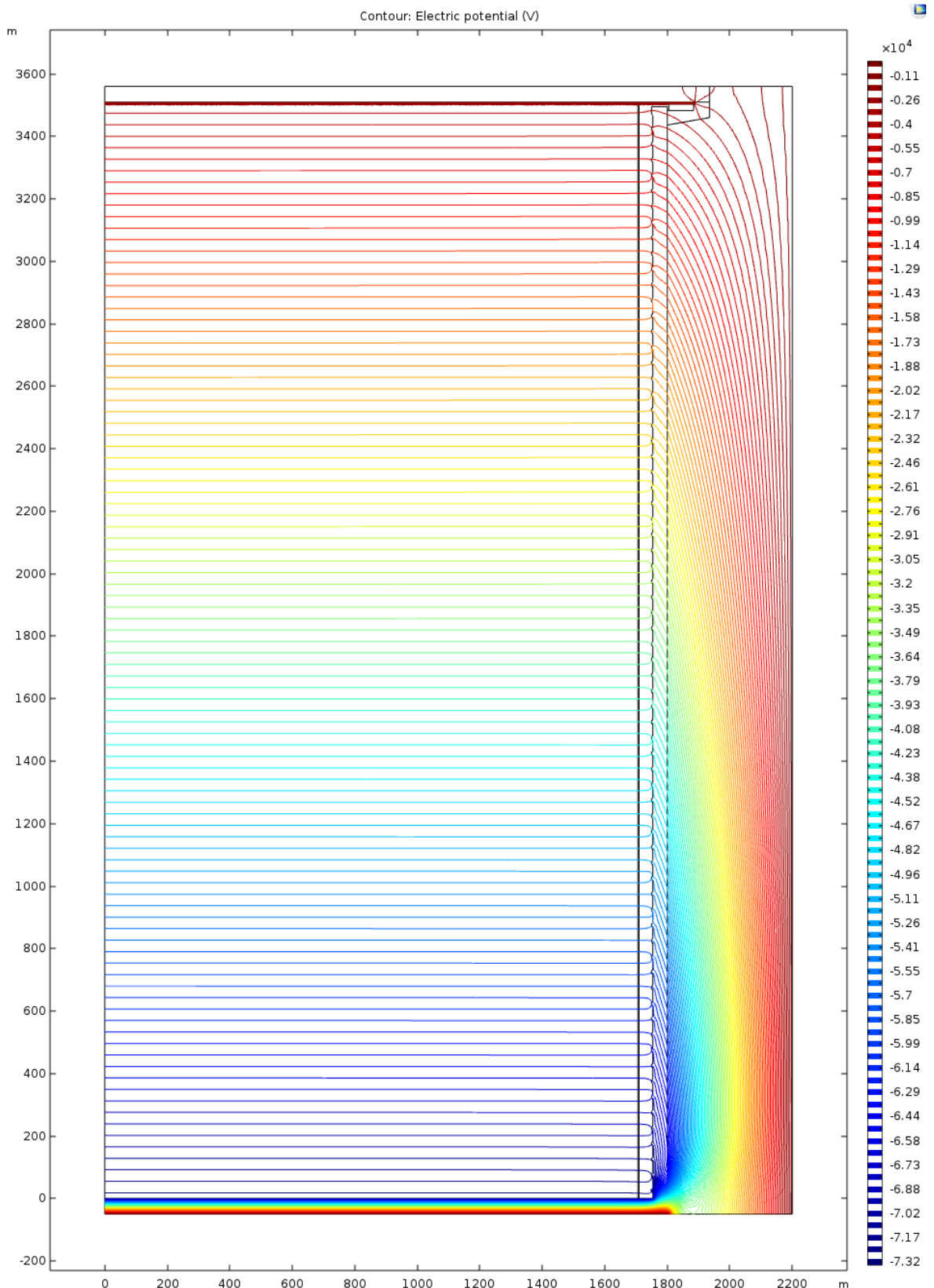


FIG. 15. Equipotential lines mapping in the DS-20k TPC showing an extremely uniform field distribution, modeled with the COMSOL Multiphysics program. Parameter settings for the calculation are those defined in Table II.

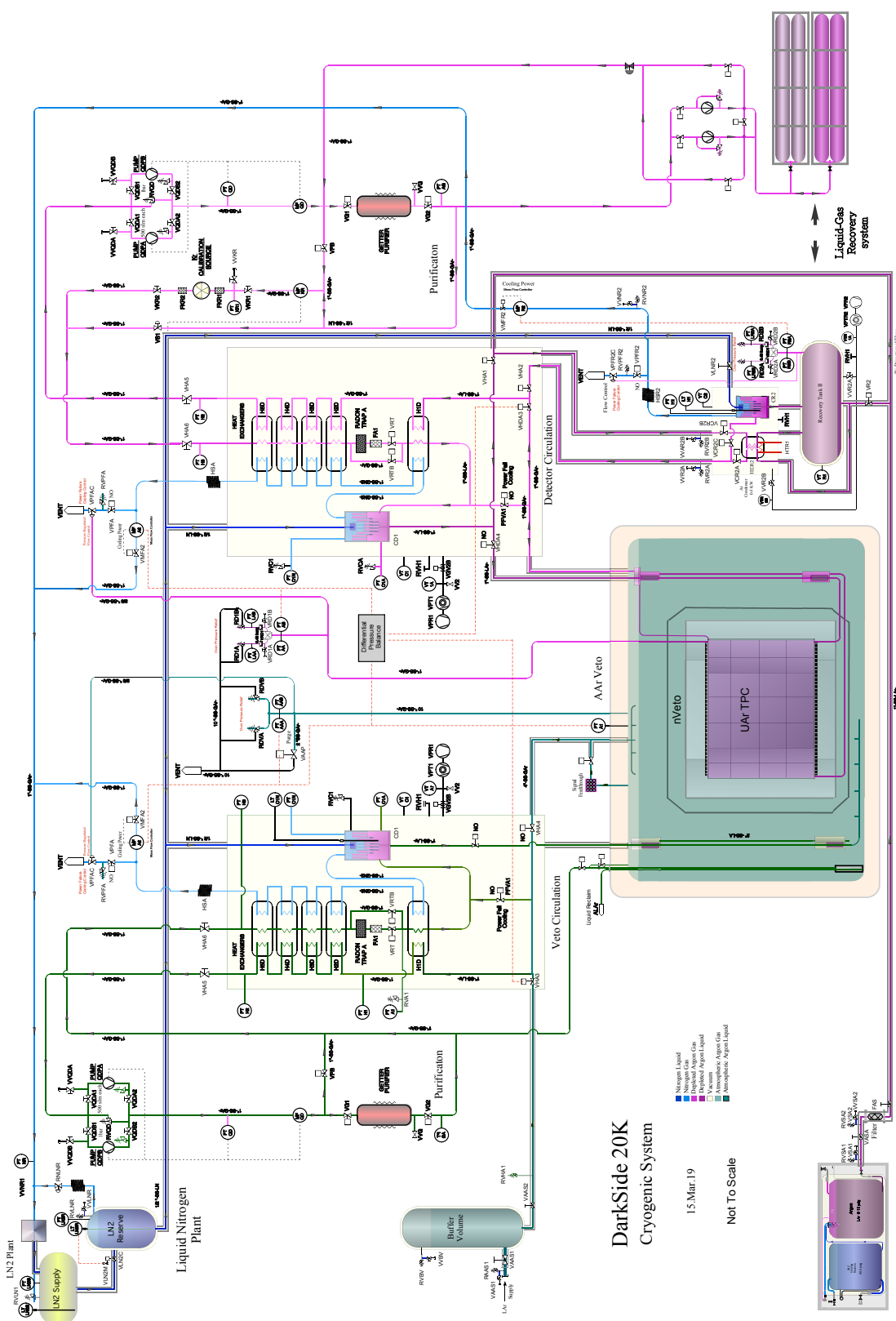


FIG. 16. DS-20k cryogenics system P&ID.

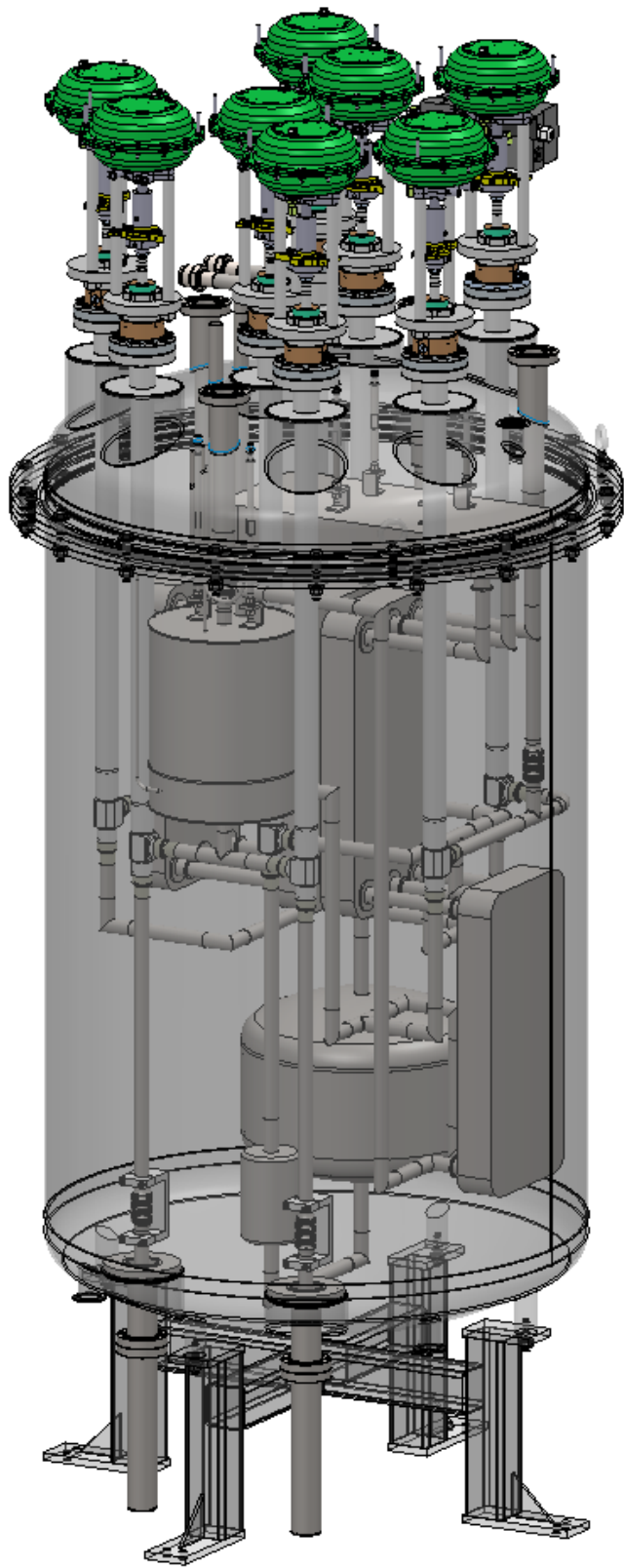


FIG. 17. DS-20k condenser box.

928 The features of the DS-50 cryogenics system are fully implemented into the DS-20k system, not
929 only by simply scaling up the argon volume, but also upgrades based on experience and lessons
930 learned. A major improvement is to increase the circulation speed to the required 1000 std L/min,
931 to initially reach the purity requirement of LAr in a couple of turn-over times of 20 d. Another
932 major improvement is to increase the cooling power needed to accommodate such a large circulation
933 speed. A full-size prototype LAr condenser, the core component in the cryogenics system, has been
934 built and tested at UCLA, and a cooling power of 2.2 kW (latent heat only) has been achieved,
935 nearly twice that needed for the DS-20k UAr cooling requirement. The main components of the
936 UAr cryogenics system condenser box have already arrived at CERN and are ready for welding and
937 the first test to follow in summer 2019.

938 The UAr cryogenics system is made up of several sub-systems (while the AAr system will be
939 similar except at larger scale in volume and power, but with lower requirements on purity): the
940 liquid argon handling system, the liquid nitrogen reserve system, the purification system, the cold
941 box, the gas circulation pump, the recovery and storage system, the integrated heat exchanger
942 system, and heat exchangers close to the TPC. The overall schematic is shown in Figure 16,
943 including the AAr cryogenics system for the veto detector, which employs the same principle. Two
944 cryogenics systems share the same liquid nitrogen reserve loop, but have separate argon loops of
945 UAr and AAr, respectively. Also shown in the figure is the condenser box integrated with the heat
946 exchangers and inline radon trap.

947 The LAr handling system delivers the clean radon-free UAr, which is initially stored in the
948 recovery storage system capable of storing the full target of UAr for DS-20k. Two options are
949 being considered, full liquid phase storage or gas phase high-pressure storage. The gas handling
950 system will be adopted to either solution in order to pre-purify the UAr before filling the TPC
951 volume. The system is also designed such that the UAr can be recuperated from the inner detector
952 to the recovery system, as needed, if an emergency occurs or at the end of the experiment.

953 The LN₂ reserve system is a closed loop with a LN₂ plant located outside of Hall C and a few
954 local liquid nitrogen dewars. The system delivers liquid nitrogen as the source of cooling power to
955 the condensers in the inner detector UAr cryogenics system, the AAr cryogenics system, and the
956 recovery system, if liquid phase storage is chosen, and recuperates the boiled-off nitrogen gas to
957 liquify it back into the LN₂ system. The UAr purification system purifies the argon in gas phase
958 during the circulation. A commercial SAES getter system has already been proven to work well in
959 DS-50 and an identified model with increased circulation capability will be used in DS-20k.

960 The cold box, as shown in Figure 17, is one of the key components of the DS-20k cryogenics
961 system, which contains all the major cryogenic handling components. Apart from the condenser,
962 the cold box contains five heat exchanger modules to efficiently pre-cool the argon gas by cold
963 nitrogen gas and cold outgoing argon gas. In this way the necessary cooling power is reduced
964 dramatically. The radon trap is placed between the coldest and the second coldest heat exchanger
965 modules to ensure that the argon passing through is still in its gas phase, while at its lowest
966 temperature, which maximizes the radon removal efficiency. Eight cryogenic valves and several
967 temperature and pressure sensors are also installed to control and monitor the system. Tubings
968 are chosen as 1" OD stainless steel, in order to accommodate the argon circulation speed up to
969 1000 std L/min.

970 The stainless steel LAr condenser contains 127 0.5" OD top-sealed tubes finely patterned on a
971 thick plate as the thermal exchanging part of the condenser. The condenser is therefore separated
972 into the nitrogen volume on the top and the argon volume on the bottom. A so-called *chicken*
973 *feeder* is mounted at the end of the liquid nitrogen delivery tube to maintain a continuous liquid
974 nitrogen dropping. The flow of the evaporated nitrogen gas is monitored by a mass flow meter
975 and adjusted by a control valve, both located at ambient temperature. The control valve uses
976 the LAr TPC pressure from both UAr and AAr as feedback signal to automatically adjust the
977 evaporated nitrogen gas flow rate, which is essentially the cooling power of the condenser, hence
978 in return maintains the LAr TPC pressure at the desired set point and balanced with AAr system
979 with an incredible stability, as demonstrated in DS-50.

980 Based on the successful demonstration of the gas circulation pump in DS-50, which provides a

981 speed up to 50 std L/min, the gas circulation pump of DS-20k uses the similar design, relying on two
982 components: linear motors and reed valves. The linear motors, consisting of a piston and cylinder
983 pair, can provide a continuously adjustable pumping power. The reed valves guide the gas flow
984 direction when the linear motors going back and forth. Two balanced linear motors will be placed
985 face to face, to counteract the vibration produced during the motor operation. The combination of
986 the linear motors and the reed valve allows the pump to work in a frictionless condition, resulting
987 in a long lifetime. The initial fast circulation requires a speed of 1000 std L/min to achieve a good
988 UAr purity level, and then the circulation speed can be decreased to only maintain the purity
989 and stability. This minimum flow could be very low since the UAr system essentially is embedded
990 in the AAr system while all cold electronics are outside the UAr volume so no cooling power is
991 required. To achieve such a high circulation speed, flexibility of operations, as well as the ease of
992 the pump development, two individual circulation pumps will be placed in parallel, each providing
993 a circulation rate up to 500 std L/min. A full-size prototype circulation pump has been fabricated
994 at UCLA and Princeton, and passed the initial tests. It was shipped to CERN and is being certified
995 for the EU safety requirement. Once fully tested, it will be integrated into the prototype cryogenics
996 system for the full-system test.

997 The heat exchangers close to the TPC are basically large heat exchangers using many tubes as
998 the thermal exchanging parts, similar to the concept of the LAr condenser described above, but
999 with a much increased thermal exchanging surface area. Outgoing LAr from the LAr TPC absorbs
1000 heat from the incoming liquid-gas mixture of purified argon here, boils off into gas phase, and then
1001 enters the circulation loop. This heat exchanger is located above the LAr TPC and ensures that all
1002 outgoing argon above it will be in gas phase, avoiding otherwise a large argon head height coming
1003 directly from the LAr TPC to the lowest heat exchanger modules in the cold box. This would
1004 result in an argon pressure below its triple point at some point in the argon loop and causing argon
1005 to freeze. Another set of near TPC heat exchangers are strategically placed close to bottom level
1006 of the UAr TPC for fast recovery during the draining stage. This lower level heat exchanger is
1007 completely passive during normal operations and only useful during the draining phase. The entire
1008 near TPC heat exchangers are immersed in LAr inside the ProtoDUNE cryostat, which serves as
1009 a thermal bath for them.

1010 The integration and tests of the full scale UAr cryogenics system at CERN is ongoing. The first
1011 pass FEA engineering has proven the design load is as anticipated and fabrication is officially ap-
1012 proved. All condenser box components, large pneumatic cryogenics valves and associated auxiliary
1013 components are on site at CERN for integration. The full scale cryogenics test of the DarkSide-20k
1014 UAr system will be performed over the summer of 2019.

1015

6. MATERIAL ASSAYS

1016 Trace radioactivity in detector materials can be a dominant background for the direct dark-
1017 matter searches. In addition to this bulk contamination, a major source of background can be
1018 caused by the cosmogenic activation of the materials and by the surface contamination (due to
1019 radon diffusion and plate out of the radon daughters produced in the surrounding air). Beta and
1020 alpha particles produced by the radionuclide decays can typically contribute to the background
1021 only if the atom is in contact with the LAr target, while gammas and neutrons, the last ones from
1022 spontaneous fission and (α, n) interactions, can produce background from more distant sites.

1023 A strategy for selecting the materials, as well as machining, storing, transporting and mounting
1024 the detector components, is mandatory in order to control the backgrounds and to maximize the
1025 physics reach of DS-20k. This will be accomplished by developing the “background budget” to
1026 identify materials’ purity requirements. In addition to the assays on the raw purchased materials,
1027 performed to identify the right technologies and compositions, we are developing cleaning and
1028 handling procedures to meet radiopurity standards, and performing assays to validate processes for
1029 the construction and commissioning of the detector and its components.

1030 In DS-20k this responsibility is delegated to the Materials and Assays Working Group (M&A WG),

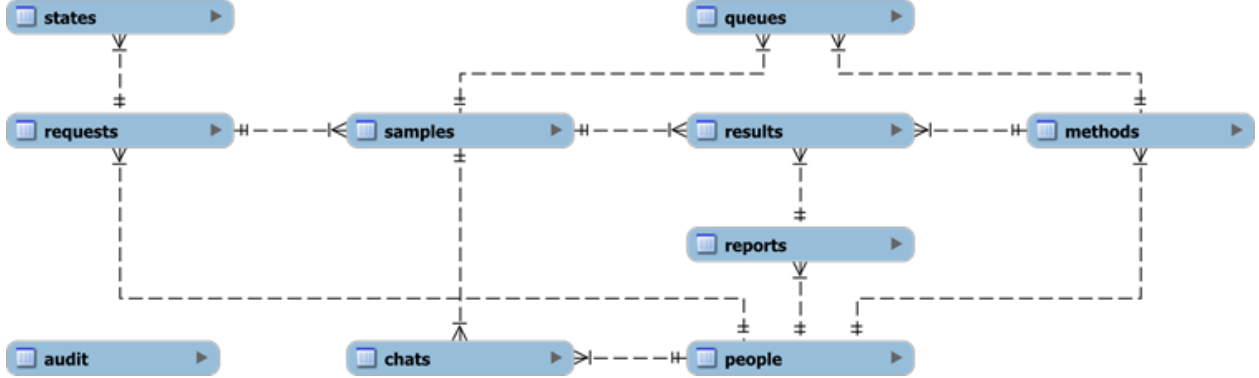


FIG. 18. A simplified DS-20k materials database structure. Information on each relevant aspect of the assay process is stored in the database, facilitating the management of the whole assay process.

1031 a single Working Group within the collaboration, comprised of experts in each of the assay methods
 1032 and representatives from each institution that hosts assay capabilities. The group coordinates and
 1033 schedules the assays according to the pre-evaluated radiopurity requirements, the urgency, the
 1034 capacity of the available assaying resources and their queue.

1035 The goal is to assay and approve *all* materials or items selected to reside within the cryostat,
 1036 particularly by scrutinizing the entire ^{232}Th and ^{238}U decay chains. This calls for multiple assays
 1037 with multiple techniques for each sample, as different techniques are applicable to different sub-
 1038 chains of the ^{232}Th and ^{238}U decay chains. These results are combined with the (α, n) cross-sections,
 1039 calculated according to the chemical composition of the material in order to extract the neutron
 1040 yield expected in the detector.

1041 6.1. Radio-purity database

1042 The need for fast access to, and exchange of data between different Working Groups (WG) is
 1043 addressed by the DarkSide Materials Database (MDB). Information on the radioactive content of
 1044 materials to be used for DS-20k construction is stored therein, and is crucial for the comprehensive
 1045 estimation of the background budget for the experiment. The MDB contains all the relevant
 1046 information about samples: chemical composition, origin (production batch), data-sheets, pictures,
 1047 part of the detector where it will be placed, history of assays etc. This information is included in
 1048 the total background budget estimation and carefully evaluated. Rules for handling and cleaning of
 1049 samples, developed and verified during the screening process, are also stored in the database. Later,
 1050 during the detector construction and integration, reproducible results of the estimated internal
 1051 background may be expected upon application of the provided handling and cleaning procedures.

1052 The database helps to systematize the radioactive background budget estimation, material se-
 1053 lection and tracking, assay prioritization, and cleaning and handling methods. Additionally, the
 1054 database is also used to balance the workload and assay resources between numerous institutions
 1055 involved in the task by coupling assay needs with assay capabilities of members of the Materials
 1056 WG.

1057 The MDB structure reflects the flow of the material assay process, aiding material selection
 1058 and application during the construction phase of the experiment. The database consists of several
 1059 cross-related tables, holding information on the status of the assay requests, screening methods,
 1060 samples, assay results and people (institutions) involved (see Fig. 18). It also keeps track of the
 1061 queues in different facilities, and the history and the current status of any assay performed within
 1062 the M&A WG. A convenient web-based interface is provided for the users (see Fig. 19), dedicated
 1063 to: ease submission of new assay requests from other Working Groups; browse and report of the
 1064 assay results (including uploading the results); and to manage the assay status of the samples and
 1065 queues at different facilities.

Sample name		Description		Batch		DS-20 reference		Search ▾							
Show 25 entries				Copy CSV Hide empty Show all Column visibility ▾				Search: capa							
ID	Report	Name	Reference	Method	Sample	Date	^{60}Co	^{137}Cs	K	^{40}K	^{234m}Pa	Pb	^{210}Pb	^{210}Po	^{226}Ra
1910	253	Capacitor 22pF	273 Non-satisfactory	PDM module	HPGe GeDSG (Matthias Laubenstein, LNGS, INFN),	complete	2018-12-13	<6 [mBq/kg] (3 sigma)	<6 [mBq/kg] (3 sigma)	1.5±0.7 [Bq/kg] (1 sigma)	<1 [Bq/kg] (3 sigma)				<1 [Bq/kg] (3 sigma)
36	5	Panasonic SMD capacitors	5 Decision pending	PDM module	HPGe GeCris (Matthias Laubenstein, LNGS, INFN),	complete	2017-12-14	<2 [mBq/kg]	<4 [mBq/kg]	<1 [Bq/kg]	<2 [Bq/kg]				<6 [mBq/kg]
1854	246	Panasonic capacitors	57 More assays needed	PDM module	HPGe BEGe (Matthias Laubenstein, LNGS, INFN),	complete	2018-08-30	<7 [mBq/kg]	<5 [mBq/kg]	<2 [Bq/kg]	<7 [Bq/kg]				<0.2 [Bq/kg]

FIG. 19. Interface web page, presenting a selection of assay results for various types of capacitors. The database is also used to manage the assay process of each sample.

Assay results obtained for the materials used for DS-50 were also imported to the new database. Currently the database stores almost 2000 assay results (more than 120 assays performed since 2017) of nearly 300 samples, and counts (see Tab. IV). The M&A WG has established protocols to efficiently handle the radioactive budget of the experiment.

6.2. Managing Assay Capabilities

To ensure the radiopurity of all detector materials to the levels defined by the background model, the M&A WG has developed a radiopurity assay program that takes advantage of facilities throughout the collaboration. Overall, it is anticipated that this program will span approximately three years and will involve around a thousand more assays, including searches for radiopure materials, development and validation of cleaning and handling procedures, and screening of all detector components. The collaboration has extensive and diverse assay capabilities that are sufficient to complete this program on schedule, with extra capacity to handle additional unforeseen assays. Estimates of the capacity available to DS-20k for each assay type are summarized in Tab. V. The assay challenges are organized into six focus areas: mass spectrometry (ICP-MS), radon emanation, direct gamma assay (HPGe), surface assays (alpha activity), cosmogenic activation and materials handling and process development.

6.3. Radioactive budget

The radioactive budget states the expected background of everything that goes into the detector, taking into account material's (element) radiopurity, mass, composition, shape and location. These parameters are the input of Monte Carlo simulations, performed using a Geant4-based package written within the collaboration and called G4DS. The result of the simulation is the efficiency of our detector for rejecting the background coming from different sources, either because of geometrical reasons or because of active tagging of undesired events. The neutron budget is calculated on a single-element basis, so the mentioned inputs (radiopurity, composition and the position in the detector) are needed for every component of the detector.

The most critical requirement in terms of radiopurity is given by the α activity, mainly caused by the naturally occurring radioactive chains of ^{232}Th and ^{238}U and potentially producing neutrons through (α, n) reactions. The cross section of this reaction is calculated using the *neucbot* program,

Assay Method	Number of assays
ICP-MS	50
Germanium spectroscopy	40
Chemical extraction of Po	20
Surface α 's counting	5
Radon emanation	5
Other	3

TABLE IV. Summary of the assays performed since 2017 in preparations of the DS-20k construction, with breakdown by assay method.

Assay Method	Capacity [assays per year]
ICP-MS	60
Germanium spectroscopy	35
Chemical extraction of Po	20
Surface α 's counting	10
Radon emanation	10

TABLE V. Summary of the assay capabilities available for DS-20k.

1094 where the energy spectrum of neutrons is generated as well. Hence, the (chemical) composition
 1095 and construction of each component needs to be known with sufficient detail in order to calculate
 1096 the interaction cross-sections correctly.

1097 Provided that some construction elements may be in similar locations, and that a component may
 1098 be used in different places, a cross-linked, multi-tab spreadsheet is used to calculate the expected
 1099 neutron budget. Propagation of any modifications or updates in a coherent way is easy to maintain.
 1100 A summary of background budget components is tabulated in a user-friendly form, collecting all the
 1101 relevant information structured following the same organization scheme as the Working Groups in
 1102 the collaboration (Veto, TPC, PhotoElectronics, etc). M&A WG is in close cooperation with other
 1103 WGs through dedicated group representatives, aiding selection of proper construction materials
 1104 at the early stages of the design. The background budget is constantly evolving and converging
 1105 as the material assay campaign progresses, such that more components' activities are determined.
 1106 It is estimated that over 1000 more assays will be performed until the completion of the detector
 1107 construction, for more than 150 expected material samples.

1108

7. CALIBRATION

1109 Calibrations for both the TPC and the Veto range from low-level detector issues, such as the
 1110 single-photoelectron response of individual photosensors, to high-level physics issues like the accep-
 1111 tance as a function of energy for nuclear recoils. The combination of radioactive sources, neutron
 1112 generators, and light sources ensures a robust calibration plan to reach ultimate science goals of
 1113 DS-20k.

1114

7.1. Distributed Gas Sources

1115 Full volume calibration of the TPC will be achieved with distributed gas sources: ^{83m}Kr and
 1116 ^{220}Rn . Gas sources are simple to implement, since they are added to the argon recirculation stream
 1117 and feature short halflives, quickly decaying out from the argon target volume. The monoenergetic
 1118 decays of ^{83m}Kr , distributed through the active volume of the TPC, can give a key calibration
 1119 point in the WIMP recoil energy region. The 3D reconstruction of events in the TPC allows a full
 1120 mapping of position-dependence of the light yield using the ^{83m}Kr source. This means that, while
 1121 broad dissemination through the active volume is important, a uniform distribution is not required.

1122 The ^{83m}Kr decays quickly ($\tau = 2.64$ h) to a stable nuclide and causes no long-term contamination
1123 or background to the WIMP search. The DS-20k ^{83m}Kr source is based on the source used
1124 successfully in DS-50. A tiny droplet of a solution of ^{83}Rb ($\tau=124.4$ d) is adsorbed into a piece
1125 of charcoal, which, after drying, is placed between two particulate filters in a branch of the argon
1126 recirculation system which is normally isolated by valves and can separately be pumped to vacuum.
1127 In DS-50, an initial 8.5 kBq of ^{83}Rb gave a ^{83m}Kr trigger rate of hundreds of Hz, even though the
1128 flow subsequently passed through a cooled radon trap. In DS-20k, the challenge will be to get the
1129 ^{83m}Kr broadly distributed in the 49.7 t active mass before it decays. To further this, LAr will be
1130 returned to the TPC after repurification via numerous tubes whose endpoints will be distributed
1131 over the surface area of the TPC side panels.

1132 ^{220}Rn and its short-lived daughters produce several γ -rays, β 's, and α 's of various energies,
1133 making it an attractive distributed calibration source that can be implemented in a similar manner
1134 as the ^{83m}Kr source, except fo the need to bypass the charcoal trap before insertion into the gas
1135 stream. The source of ^{220}Rn may be prepared as an electroplated ^{228}Th on stainless steel or copper.
1136 Enclosed in a small metal-sealed and vacuum-tight volume equipped with a VCR/CF port. The
1137 advantages of the ^{220}Rn source are the following:

- 1138 • ^{220}Rn and its daughters are short-lived, the longest half-life in the chain is 10.6 h for ^{212}Bi ,
1139 therefore the activity introduce into the detector will disappear after a few days;
- 1140 • The high energy alphas appearing in the chain (6.05 MeV, 6.09 MeV, 6.29 MeV, 6.78 MeV, and
1141 8.78 MeV);
- 1142 • The coincident ^{220}Rn - ^{216}Po and ^{212}Bi - ^{212}Po decays will allow to study the homogeneity of the
1143 distributed sources, and possible LAr flow patterns as well as potential “dead volumes” that are
1144 not affected by the LAr circulation;
- 1145 • Drift of the charged ions inside the LAr volume (interesting also with respect to Po isotopes from
1146 the ^{222}Rn chain);
- 1147 • Low-energy β 's appearing in the chain may be used for calibrations of the low-energy response
1148 of the detector.

1149 To avoid removal of the ^{220}Rn source by the charcoal trap it should be bypassed during the
1150 calibration run. Release of ^{220}Rn from the source should be done in a way that avoids contamination
1151 of the detector with residual ^{224}Ra (half-life 3.6 d) or ^{228}Th (half-life 1.9 yr). A similar risk exists
1152 for the ^{83m}Kr source, but has been thoroughly mitigated and never observed.

1153 7.2. Gamma Sources

1154 Three external γ -ray sources, ^{60}Co , ^{133}Ba , and ^{137}Cs , are planned for use in the TPC calibration.
1155 The combination of these sources in the absence of ^{39}Ar gives an excellent calibration of the electron
1156 recoil PSD band, energy scale and provide valuable data for tuning of the detector response in the
1157 Monte Carlo simulation. The γ -ray sources were chosen to span the energy range of interest in
1158 combination with the distributed ^{83m}Kr source: 41.5 keV for ^{83m}Kr , 122 keV for ^{60}Co , 356 keV for
1159 ^{133}Ba , and 662 keV for ^{137}Cs . Sources will be miniature in size to be inserted inside the source
1160 guide tube for TPC, the overall design of which is shown in Figure 20.

1161 7.3. Neutron Sources

1162 Neutron sources are of particular interest for calibration of the nuclear recoil PSD band and
1163 the efficiency of the neutron veto, a key feature of the DS-20k design. Small (α,n) sources such as
1164 $^{241}\text{AmBe}$ and ^{241}Am - ^{13}C will be fabricated for this purpose. $^{241}\text{AmBe}$ is utilized as a tagged neutron
1165 source utilizing 4.4 MeV gamma in 56 % cases. ^{241}Am - ^{13}C can serve as a gamma-free source for Veto
1166 neutron calibration, after slowing down alphas for (α,n) reaction to always produce daughters in
1167 the ground state. Sources will be small in size to be delivered with the source guide.

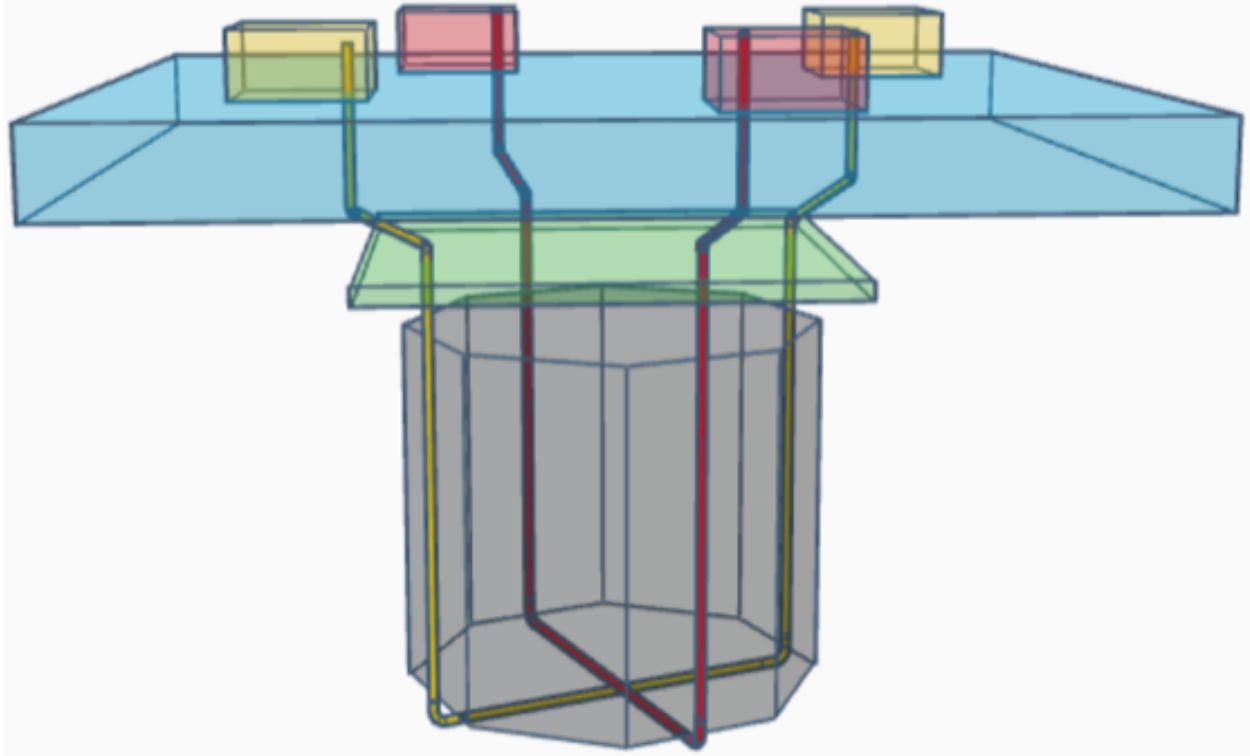


FIG. 20. Schematic representation of the system of guide tubes for insertion of sources.

While the $^{241}\text{Am}^{13}\text{C}$ source represents the best choice for calibration of the neutron detection efficiency, interactions in the source holder and materials between the source and the TPC produced significant electron recoil background in the DS-50 TPC, problematic for characterization of the nuclear recoils of argon nuclei. The $^{241}\text{AmBe}$ source was shown to be more suitable for this calibration. The 4.4 MeV γ -ray is promptly emitted in the $^9\text{Be}(\alpha, n)^{12}\text{C}$ nuclear reaction in about 56 % of cases. By tagging the 4.4 MeV γ -ray in the Veto in a very tightly constrained time interval prior to the signal in the TPC, a very pure sample of nuclear recoils is obtained. The $^{241}\text{AmBe}$ calibration in DS-50 provided the best available nuclear recoil calibration of the DS-50 TPC *in situ*, and was in excellent agreement with the nuclear recoil calibration from the stand-alone SCENE experiment [33].

The main novelty planned for the $^{241}\text{AmBe}$ calibration is a custom production of a miniature (a few mm) $^{241}\text{AmBe}$ source, since the typically available commercial sources cannot fit within the planned narrow guide tube system. The miniature $^{241}\text{AmBe}$ source will rely on the procedure developed by the neutrino group at the University of Alabama [58]. The group successfully fabricated an $^{241}\text{AmBe}$ source with an outer capsule dimension of just 2 mm in diameter and 7 mm long, with an activity of 50 neutrons per second using 1.9 MBq of ^{241}Am . Fig. 21 shows the outer and inner source capsules. The inner capsule is made of tungsten to efficiently suppress the 4 MeV gamma emission from the ^{241}Am . A very pure Be powder is mixed with ^{241}Am high purity powder in an alcohol solution in a miniature test tube with a special micropipette and then transferred into the tungsten capsule. After the alcohol evaporates, the procedure is repeated. In the end, the mixture of $^{241}\text{AmBe}$ is compressed with a wire for higher source activity. The wire is also used to seal the tungsten capsule. The tungsten capsule is placed inside the stainless steel capsule and welded shut. The source is then ready for certification and use. The outside capsule has a threaded part to attach the source to the rest of the calibration system.

Photoneutron sources such as YBe emit nearly monoenergetic 157 keV neutrons, suitable for the low energy end of the nuclear recoil band. However, such source requires 15 cm thick tungsten shield to block copious γ -rays present in the source. Thus, this source is very bulky and requires

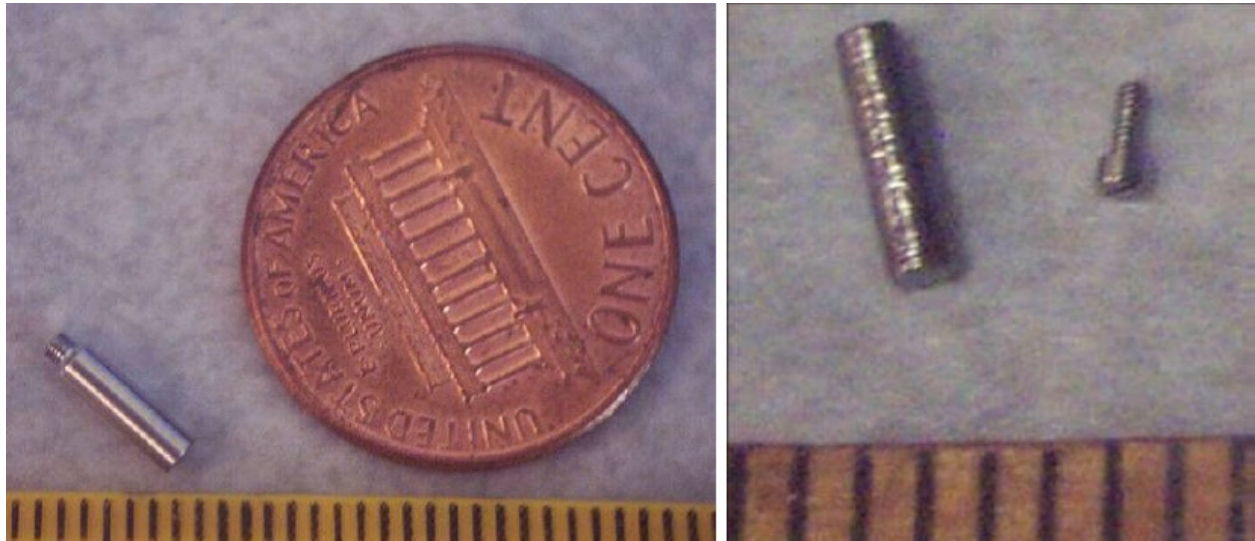


FIG. 21. **Left:** the outer capsule of the custom made $^{241}\text{AmBe}$ source from the Alabama group [58]. **Right:** the inner tungsten capsule of said $^{241}\text{AmBe}$ source.

1195 a separate deployment system. Deployments will be monitored via a camera system to avoid any
 1196 undesirable contact while operating in a delicate Veto.

1197

7.4. Guide Tube System

1198 Implementation of calibration sources is being finalized, following the completion of the designs of
 1199 the TPC the Veto, and the AAr cryostat. In parallel, plans are being developed for the calibration
 1200 needs of the DS-20k prototype detectors for x-y positioning, light yield and nuclear recoil calibration.
 1201 While work is still in progress, the overall schematic of how to guide radioactive sources from the
 1202 roof of the AAr cryostat, down around and inside of the Veto detector, and then back up to the
 1203 cryostat roof, is shown in Figure 20. The guide tube systems have been designed for simple, safe
 1204 and efficient calibration of the Veto and TPC using miniature radioactive sources. They will allow
 1205 deployment of the sources inside the Veto without direct contact with the argon, eliminating risks
 1206 associated with it.

1207 The guide tube system will bring radioactive sources from the top of the AAr cryostat, to
 1208 locations along the TPC exterior. The sources will be delivered through an enclosed stainless steel
 1209 tube coming vertically down from the top of the cryostat, passing by the TPC PMMA vessel and
 1210 around its bottom. The guide tubes will be 3 cm (1.18") in diameter to minimize shadowing, dead
 1211 space and radioactive background coming from the stainless steel. The stainless steel tube segments
 1212 will be connected with Swagelok connectors. In addition, relatively small tube diameter will help
 1213 for tighter control of the source location, especially important in the case of the gamma sources.

1214 The miniature sources will be attached to the stainless steel guide wire that will be pushed with
 1215 a wire driver powered by a stepper motor. A sleeve, made out of the PTFE tubing, will envelope
 1216 the guide wire and the source to significantly reduce friction while the source and its guide wire are
 1217 being pushed around. The wire driver will be equipped with a set of encoders and two sensor boxes
 1218 for accurate positioning of the source. A pair of ring type inductive proximity sensors placed inside
 1219 the sensor box will be used to reset the encoders when sources pass through a sensor at exactly
 1220 known locations. The system will be purged with a low pressure nitrogen to eliminate any residual
 1221 radioactivity that may have entered into the tubes.

1222 Except for the sensor box, all other parts of the guide tube system that require power, control
 1223 and nitrogen flow will be at the top of the AAr cryostat. An elaborate testing program must be
 1224 performed to ensure high quality and safety of the calibration when using the guide tube system.

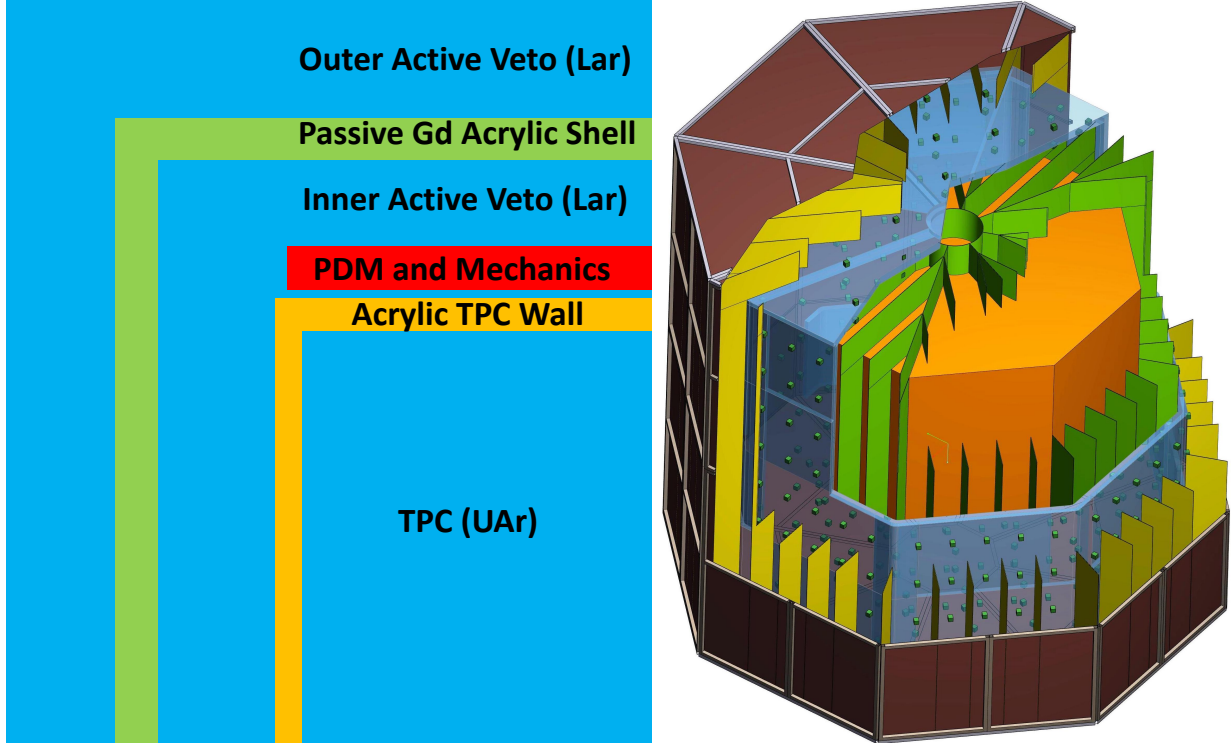


FIG. 22. **Left:** schematic conceptual view of the veto detector. **Right:** 3D cut-away view of the DS-20k veto detector.

1225 All parts will be radio-assayed and the entire system will be tested off-site for robustness, precision
 1226 and reliability. Dedicated survey is planned to record the exact guide tube path around the TPC
 1227 PMMA vessel.

1228

8. VETO DETECTOR

1229

8.1. Overall Design

1230 Benefiting from the implementation of a ProtoDUNE-like AAr cryostat, the Veto detector will
 1231 utilize AAr as the scintillation material. The Veto detector is composed of three separate volumes;
 1232 a passive octagonal acrylic shell loaded with gadolinium called the GdA and mounted around the
 1233 TPC and providing $4 - \pi$ coverage, a 40 cm thick inner volume of active liquid AAr called the Inner
 1234 Argon Buffer (IAB) and sandwiched between the TPC vessel and the GdA, a 40 cm thick outer
 1235 active volume of AAr called the Outer Argon Buffer (OAB) contained between the GdA and the
 1236 outer copper Faraday Cage. The Faraday Cage will contain the Veto and TPC and optically and
 1237 electrically isolate them from the remaining outermost AAr volume contained within the cryostat.
 1238 A schematic drawing of the Veto concept is shown in the left side of Figure 22, as well as a 3D
 1239 cut-away drawing which presents the preliminary design.

1240 The required thickness of both the IAB and OAB of about 40 cm has been determined by MC
 1241 simulation. The required thickness of the GdAS determined by the same simulation, is about 10 cm
 1242 with a required Gd loading of 1 to 2 % by weight. The GdAS moderates neutrons emitted from all
 1243 of the detector materials, particularly from the ones which make-up and surround the LAr TPC,
 1244 while also enhancing the neutron capture probability with the inclusion of the Gd. The capture of
 1245 the neutron on a Gd nucleus results in the emission of multiple γ -rays. These γ -rays interact in
 1246 the IAB and OAB, their detection efficiency setting the required GdAS thickness and Gd loading
 1247 fraction, as well as the minimum required IAB and OAB thickness. γ -rays are detected by use of

1248 scintillation light emitted by the liquefied AAr in both the IAB and OAB.

1249 Vertical segmentation of the IAB and OAB is foreseen to reduce the pile-up rate of ^{39}Ar events
1250 from the AAr. The concept of this is shown in the cut-away view of the detector in the right panel
1251 of Figure 22, while the exact details are still being optimized by use of the Monte Carlo simulation.
1252 SiPMs will be mounted on the sides of the GdAS such that they are facing both the IAB and OAB.
1253 The basic detector element is the same PDM used in the TPC, but with a different front-end board
1254 coupled to it that is optimized for the geometry of the Veto detector. Tests are in progress to
1255 investigate the possibility of using an integrated electronics readout design for the Veto detector.

1256 All of the inner surfaces of the Veto, including the external walls of the TPC and the walls of the
1257 vertical sectors, will be covered with reflector foils coated with wavelenght shifter (TPB), so that
1258 the VUV argon scintillation light is shifted to longer wavelengths where the LAr is very transparent.
1259 This light is then trapped within a segment of the Veto detector by multiple reflections until it
1260 reaches a SiPM. The optimal number of segments is being studied with the Monte Carlo simulation.
1261 We expect no more than 5 segments for each edge of the octagon. The segments are not liquid tight
1262 to allow flow of the argon through them, with a dedicated fluid-dynamics simulation planned to be
1263 performed to ensure that the LAr can be properly re-circulated throughout the proposed geometry.

1264 The overall Veto detector design and the Monte Carlo simulation results will be validated using
1265 smaller prototype setups. Due to the nested nature of the detector system, strategic planning for
1266 the detector integration is also a big part of the development planning.

1267 This conceptual design promises to achieve the most important criteria for the DS-20k detector,
1268 which is the efficient detection of neutrons such that no instrumental background interferes with
1269 the potential nuclear recoil signal from a WIMP scattering off of an argon nucleus. The design
1270 concept is scalable and lends well to serve as the basis for the future 400 t scale detector designed
1271 to collect an exposure of 1000 t yr in absence of instrumental background. The Veto design is based
1272 on elements which require no R&D and therefore can be built out of materials already available,
1273 with the only exception being the gadolinium loaded acrylic. We have established good contacts
1274 and an agreement with a company available to test in its laboratory techniques to mix gadolinium
1275 compounds with liquid MMA before starting the polymerization process. Taking into account that
1276 we do not need the final Gd-doped acrylic to be transparent to light (it acts only as passive neutron
1277 moderator), and that the homogeneity of the mixture is also not a critical parameter, several known
1278 difficulties related to metal loading into plastic scintillators are not an issue. After the success of
1279 the small scale laboratory test done in 2018, the company who will likely provide the high-quality
1280 acrylic for the JUNO experiment has agreed to produce samples of gadolinium loaded acrylic using
1281 their industrial production line. Radio-purity tests will be performed on these samples once they
1282 are available.

1283 8.2. Assembly

1284 The assembly sequence starts with the mounting of the bottom part of the GdAS along with its
1285 PDMs. This component will rest on a stainless steel support structure (Veto support structure)
1286 that is itself supported by the cryostat floor via temporary feet. The TPC is then lowered into its
1287 place above the bottom of the Veto detector. Once in place, the TPC is mechanically connected
1288 to the support structure of the Veto through mounting pillars. This choice has been driven by the
1289 aim of reducing the mass of the support structure of the TPC and avoiding relative movements
1290 between the TPC and the VETO during construction, commissioning and detector operation.

1291 Once the TPC is fixed to the Veto support structure, the lateral panels of the GdAS and their
1292 PDMs are mounted. The vertical thin panels that divide the IAB into segments are then installed.
1293 The top GdAS panels are assembled next. Once the construction of the IAB is completed, PDMs are
1294 installed on the external surfaces of the GdAS and the panels which divide the OAB into segments
1295 are integrated. Then the copper frames that are used as the main structure of the Faraday cage
1296 are installed in the outermost part of the Veto. Finally the Veto detector is hanged from the
1297 cryostat roof using a dedicated support structure and several Kevlar ropes. One the Veto detector

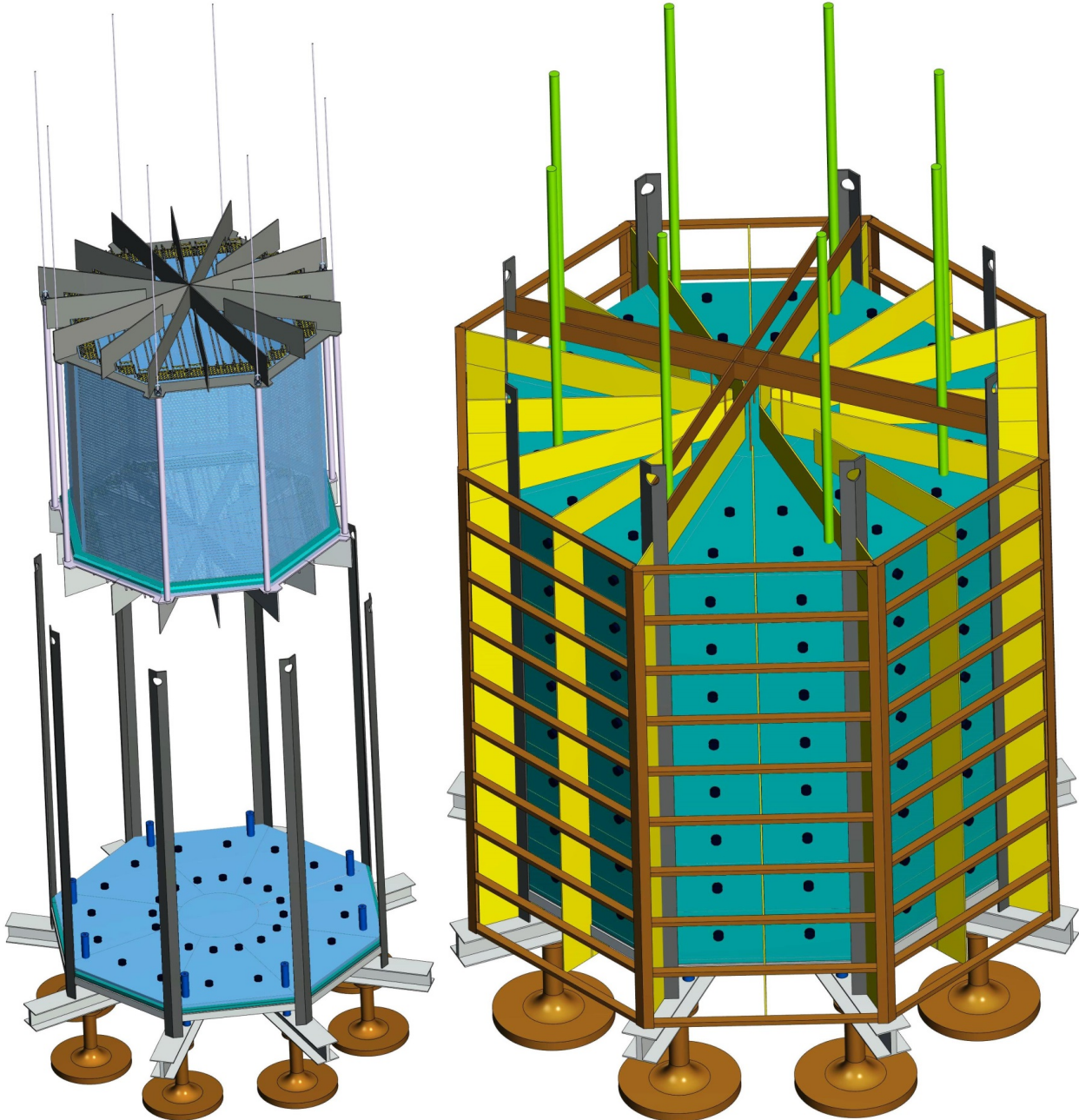


FIG. 23. **Right** Conceptual view of the placement of the TPC within the Veto support structure. **Left** 3D drawing of the DS-20k Veto detector, along with the temporary bottom support structure used for assembly and the Faraday cage.

1298 construction is completed, the temporary pillars used to support the Veto on the cryostat floor
 1299 during the construction are removed.

1300

8.3. Background Rejection

1301 The combination of the signals occurring inside the IAB and OAB, within a given time window,
 1302 is used to tag and reject neutron captures. If a neutron produces a signal in the TPC, it will mimic
 1303 that of a WIMP signal, meaning that it produces a single energy deposit with energy in the range

Material	Mass [tonne]	^{238}U [mBq/kg]	^{226}Ra [mBq/kg]	^{232}Th [mBq/kg]	Neutrons [10 yr] $^{-1}$	+TPC [200 t yr] $^{-1}$	+TPC+veto [200 t yr] $^{-1}$
TPC Vessel	2.7	1.2×10^{-2}	10	4.1×10^{-3}	1.1×10^3	0.17	1.7×10^{-2}
TPC SiPMs	0.12	-	-	-	1.1×10^4	0.16	1.6×10^{-2}
TPC Electronics	1.0	-	-	-	2.5×10^4	0.36	3.6×10^{-2}
TPC Mechanics	1.1	3.9	3.9	1.9	1.8×10^3	1.8×10^{-2}	2.0×10^{-3}
Veto SiPMs+elec.	0.40	-	-	-	1.3×10^4	0.10	1.0×10^{-2}
Veto Acrylic	13	1.2×10^{-2}	10	4.1×10^{-3}	5.2×10^3	4.2×10^{-2}	4.0×10^{-3}
Veto Reflectors	1.0	1.2×10^{-2}	1.0	4.1×10^{-3}	4.0×10^2	2.4×10^{-2}	2.0×10^{-3}
Veto Steel	1.1	3.9	3.9	1.9	1.8×10^3	1.4×10^{-2}	1.0×10^{-3}
$\text{Gd}_2(\text{SO}_4)_3$ α 's on self	0.26	7.0	7.0	0.2	2.1×10^2	2.0×10^{-3}	$<1.0 \times 10^{-3}$
$\text{Gd}_2(\text{SO}_4)_3$ α 's on PMMA	0.26	7.0	7.0	0.2	7.2×10^2	6.0×10^{-3}	1.0×10^{-3}
Copper Cage	1.0	0.30	0.30	2.0×10^{-2}	1.2×10^1	$<1.0 \times 10^{-3}$	$<1.0 \times 10^{-3}$
Cryostat Steel	250	50	1.0×10^3	3.9	1.0×10^6	-	$<1.0 \times 10^{-3}$
Cryostat Insulation	40	3×10^3	8.0×10^3	3.0×10^3	8.0×10^7	-	$<1.0 \times 10^{-3}$
Total						0.9	0.09

TABLE VI. Radiogenic neutrons sourced by the LAr TPC construction materials, veto and cryostat materials, with details of expected contamination levels, background after TPC cuts, and residual background after combined TPC and veto cuts, all relative to the full 10 yr run time and the full fiducial 200 t yr exposure. The number of expected neutrons is calculated from the expected contamination levels and material composition. Note that no specific activity is reported for the TPC SiPMs and associated electronics: in this case the predicted neutron yield is the results of an extremely detailed calculation, accounting for the cumulative contribution of several tens of components, individually assayed. The same consideration holds for the veto SiPMs and electronics, which contribution is reported in combination. For neutrons due to (α, n) reactions resulting from α 's originating from impurities in $\text{Gd}_2(\text{SO}_4)_3$, the contribution is broken down between those due to reactions on Gd sulfate itself and those due to reactions in the PMMA matrix containing the Gd sulfate; the mass fraction of Gd in the GdAS 1%, for the anticipated 2% concentration by mass of $\text{Gd}_2(\text{SO}_4)_3$. (For ease of conversion: 1 ppt(^{238}U) $\simeq 1.2 \times 10^{-2}$ mBq/kg; 1 ppt(^{232}Th) $\simeq 4.1 \times 10^{-3}$ mBq/kg.)

1304 30 keV_{nr} to 200 keV_{nr}. This also includes fiducial volume cuts which exclude events occurring at a
 1305 distance from the TPC walls less than 30 cm in the radial direction and less than 70 cm from the
 1306 top and bottom. For events that pass this fiducialization, the Veto is then searched within a time
 1307 window of 800 μs around the TPC trigger time. To minimize dead time losses due to β -decay from
 1308 ^{39}Ar in the veto filled with AAr, a 800 keV threshold is set for each of the two parts of the Veto
 1309 detector, while a lower 100 keV threshold is set for events with coincidence signals in both parts of
 1310 the Veto detector.

1311 The design of the Veto and the choice of all the materials used to build the entire detector are
 1312 set by the requirement of having less than <0.1 events untagged neutrons during the total exposure
 1313 of 200 t yr. The radioactive contamination of the materials used to build the Veto is therefore also
 1314 considered and limits are set by requiring that the corresponding neutron background induced in
 1315 the TPC, after the implementation of all analysis cuts, is well below the above mentioned threshold
 1316 of <0.1 events in 200 t yr.

1317 DS-20k is designed to operate with zero backgrounds, meaning that all sources of instrumental
 1318 background are reduced to <0.1 events over a 200 t yr exposure. All background from minimum-
 1319 ionizing radiation sources will be completely removed thanks to the combined action of PSD of
 1320 the primary scintillation pulse and comparison of the primary and secondary scintillation (see the
 1321 “Project Narrative” for details on the suppression of background from pp scatters on electrons and
 1322 Ref. [24] for that from ^{222}Rn , ^{220}Rn , and progenies).

1323 We focus here on the leading source of background, that is neutrons from the LAr TPC con-
 1324 struction materials. We simulated the response of the LAr TPC, IAB, and OAB to (α, n) , which is
 1325 expected to be the dominant contribution to the instrumental background budget. The geometry
 1326 of the LAr TPC is that described in the rest of the document. The LAr TPC vessel is made of
 1327 5 cm-thick PMMA, which helps to mitigate backgrounds by moderating the neutrons coming from
 1328 the detector’s construction materials. For the PMMA, we assume the purity achieved in Ref. [42],
 1329 while for the Gd-loaded acrylic, we assume the purity of the scintillator of Ref. [59].

1330 The results of the Monte Carlo simulation are summarized in Table VI, where it is seen that the
1331 final results meet the goal of <0.1 events in the full 200 t yr exposure. The two main sources of
1332 contamination are the electronics of the SiPMs and the insulation of the cryostat. The collaboration
1333 is now working to further improve the materials selection, which could reduce the expected neutron
1334 flux coming from those components.

1335 The only remaining background for WIMP searches will be the signal from the coherent scattering
1336 of atmospheric neutrinos on argon nuclei, with an expected 3.2 events over the 200 t yr exposure.
1337 DS-20k will thus be the first experiment in a position to detect this important signal.

1338 Surface contamination due to plate-out of radon on the surfaces is an additional source of back-
1339 ground that can not be neglected. Radon is present in the outdoor air with a concentration of few
1340 to 10 Bq/m³, while inside buildings and in underground laboratories the concentration is typically
1341 higher (up to 120-150 Bq/m³). ²¹⁰Pb atoms accumulate on every surface of materials exposed
1342 to air and decay to ²¹⁰Bi that produces ²¹⁰Po. This is the potentially dangerous isotope because
1343 the α originating in its decay could produce neutrons. We estimate the concentration of ²¹⁰Pb
1344 adsorbed on an acrylic surface using data measured for polyethylene exposed to the SNOLAB air.
1345 We roughly expect a few tens of neutrons (before the analysis cuts) per day during the time which
1346 the entire surface of the acrylic is exposed to atmospheric air. This sets specific requirements for
1347 the cleanliness of the acrylic surfaces and on the mounting procedures of the Veto, which must be
1348 done in a radon free environment.

1349 9. DATA ACQUISITION

1350 The current design for the DS-20k electronics and its data acquisition system (DAQ) accommo-
1351 dates both the large number of sensors and the long drift-time (expected maximum electron drift
1352 time is 4 ms) of the LAr TPC, as well as the readout of the Veto detector. The trigger rate during
1353 normal dark matter search data taking has three major contributions: background events from de-
1354 tector materials, background events from ³⁹Ar, and random triggers. In order to estimate the first
1355 term, the event rate measured in the UAr exposures of DS-50 is taken, excluding the contribution
1356 from the PMTs and from the remaining ³⁹Ar in DS-50. This is scaled by the ratio of surface areas
1357 of DS-20k and DS-50, a factor of 55, obtaining an expected rate of 27 Hz. It is noted that these
1358 events will be concentrated at the surfaces of the active volume.

1359 By using UAr and making the assumption of an ³⁹Ar reduction factor of 1400 with respect to
1360 AAr, there will still be an additional rate of about 16 Hz generated by ³⁹Ar decays, uniformly
1361 distributed throughout the active volume. In summary, events with correlated S1 and S2 signals
1362 are expected in DS-20k at a rate of about 50 Hz. On the other hand, the average singles rate per
1363 channel is dominated by the dark count rate (DCR) of the SiPMs. With the required 0.08 Hz/mm²
1364 specification, this will imply a singles rate per PDM of about 200 Hz. The event rate in the Veto
1365 detector, instead, will be dominated by ³⁹Ar decays in the instrumented AAr buffers.

1366 9.1. General DAQ scheme

1367 The baseline scheme for the TPC and Veto detector DAQ electronics hardware foresees an optical
1368 signal receiver feeding a differential signal to a flash ADC digitizer board that is connected to a large
1369 Field Programmable Gate Array (FPGA). The digital filtering capability within the digitizer board
1370 would allow the discrimination of single photoelectron signals and the determination of the time
1371 and charge of the individual channel pulses. For large and slow signals, such as the S2 ionization-
1372 born pulses in the TPC, the digitizer board would provide a downsampled waveform matching the
1373 expected signal bandwidth of a few MHz.

1374 The combination of the data processing will provide the needed data reduction to allow trigger-
1375 less operation of the readout for the TPC. Data from the Veto and TPC detectors will be transferred
1376 to the front-end data processing units where further data reduction will be performed. Finally the

1377 data will be passed to an online event building processor that will select interesting events and
1378 write them to permanent storage.

1379 In normal data taking mode, an event could be identified by a coincidence of hits in the TPC
1380 within a specified time window. A coincidence of 7 hits in 200 ns would result in a random trigger
1381 rate well below 0.1 Hz. Nuclear recoil events at the trigger threshold, producing about 15 PE in
1382 5 μ s, would result in the collection of 6 PE to 8 PE within the first 200 ns. Thus, the trigger would
1383 be 100 % efficient for the WIMP-like signals of interest.

1384 The event building and software trigger stage is realized with modern commodity CPUs and
1385 connected through fast ethernet with the front-end DAQ processors. Given the low expected rate,
1386 the trigger-less option is foreseen to be feasible to implement. The expected combined event size
1387 for the TPC and Veto detectors is projected to be well below 1 MB.

1388 Synchronization between the TPC and Veto DAQ is fundamental for the effectiveness of the
1389 design, and will be provided and maintained during the data taking. The clock source of the TPC
1390 DAQ will be used as reference and digital signals (like GPS time stamps or trigger IDs) will be
1391 generated to uniquely identify each event regardless of the trigger origin or the detector. A pulsed
1392 signal distributed to all the modules will be used to check and correct the alignment of each channel
1393 among the TPC and Veto detectors.

1394 The DAQ system will be located in an electronics room which will be placed on the roof of the
1395 AAr cryostat. The environment will allow personnel access while minimizing the length of the
1396 optical fibers used to transmit the data from the TPC to the signal receivers.

1397 9.2. Digitizers

1398 The basic readout element of the proposed DS-20k DAQ system is a multi-channel board hosting
1399 several fast ADCs linked to a large FPGA for digital signal processing. This will be connected
1400 to a host CPU for control, monitoring and data formatting using as an output channel through
1401 a 1 Gbit/s to 10 Gbit/s ethernet connection to an external computer. The ADC will have 14 bits
1402 resolution and 125 MHz sampling speed. The board will accommodate one octal fADC chip for
1403 each of the 8 mezzanine boards, allowing if to handle 64 channels in total with a single board with
1404 a VME64 6U form factor. Data from the ADCs will be sent using high bandwidth JESD interface
1405 directly to a large FPGA. The board will host a Xilinx made Zync Ultrascale+ with a quad-core
1406 ARM Cortex A53 processor. Recent progress on this development includes the full implementation
1407 of the JESD interface and the ability to output data at the maximum specified speed. Specialized
1408 firmware is to be provided by the collaboration for noise filtering, basic data formatting and zero
1409 suppression to be implemented in the FPGA.

1410 The development of this electronics board is an ongoing partnership between the CAEN Company
1411 from Viareggio, Italy, which was selected as the provider of the electronics by the INFN, and the
1412 collaboration. The basic layout of the boards and the components that will comprise them have
1413 been selected and the first prototype will be available for testing in the summer of 2019. In the
1414 meantime, work in close cooperation between the GADMC and the CAEN firmware experts is
1415 ongoing to implement the needed signal filtering algorithms. In parallel, a DAQ system for the
1416 initial prototype TPC tests has been deployed at CERN in order to acquire data from up to two
1417 PDM Motherboards, amounting to 50 PDM channels.

1418 9.3. DAQ software

1419 The Maximum Integrated Data Acquisition System (MIDAS) has been chosen as a framework
1420 for developing the DAQ readout and related online control software for the DS-20k detector. The
1421 MIDAS DAQ package has been used extensively within the DEAP-3600 experiment, and together
1422 with the CAEN hardware provides a nice baseline for the digitization and recording of the raw data.
1423 A collaboration between the MIDAS and CAEN developers has been established to ensure that the

1424 interfacing of the front-end hardware is compatible with the back-end hardware and software that
1425 will ultimately compile and write the data to permanent storage.

1426 MIDAS is also well suited for handling the DAQ of the DS-Proto, for which, at least in the first
1427 stage, has a readout strategy and hardware implementation similar to those used in the DEAP-3600
1428 experiment. The DEAP-3600 hardware is mainly composed of 32xVME-V1720 and 4xVME-V1740
1429 using the proprietary CAEN CONET2 optical link to 5 different computers, providing optimum
1430 individual link data throughput using the A3818C PCIe interface. The DS-Proto readout will be,
1431 in the first phase, based on 5 CAEN VME-V1725 and a custom trigger module developed by the
1432 TRIUMF group. This system has been already installed at CERN in the first part of 2019 in order
1433 to provide the DAQ system for the first 50 channels (2 motherboards) of DS-Proto. In a later
1434 stage, the readout for DS-Proto will be based on the new digitizer boards from CAEN, previously
1435 described. Work has started toward designing an evolution of the MIDAS software to accommodate
1436 the new hardware boards and provide the needed event building and software trigger capability.

1437 10. COMPUTING

1438 The data storage and offline processing system must support transfer, storage, and analysis of
1439 the data recorded by the DAQ system, for the entire lifespan of the experiment. It must provide for
1440 production and distribution of simulated data, access to conditions and calibration information and
1441 other non-event data, and provide resources for the physics analysis activities of the collaboration.
1442 Necessary components for data storage and offline systems are the software framework and services,
1443 as well as the data management system, user-support services, and the world-wide data access and
1444 analysis job-submission system. The design of the system is built upon the knowledge acquired in
1445 the construction and operations of the DS-50 detector.

1446 The large number of channels in the LAr TPC makes it impractical to digitize and save the full
1447 waveform of each channel, as done in DS-50. Nevertheless, the charge and hit time information
1448 that will be saved will preserve all the necessary details about the amplitude and time evolution
1449 of the signals generated in the target. With appropriate filtering and compression, in addition
1450 to the expected background reduction described elsewhere in this document, the amount of data
1451 selected for recording in DS-20k is expected to be only a few times that of DS-50. The DS-50
1452 experiment typically collects about 9×10^5 events/d, of which 8×10^5 events/d come from laser
1453 calibrations, with the remaining 1×10^5 events/d from the dark matter search. The size of a DS-50
1454 laser calibration event is about 0.1 MB, while the size of a dark matter search data event is about
1455 2.6 MB. This is expected to decrease by a factor of 3 to 4 in DS-20k, despite the much larger number
1456 of channels. Taking into account the event size and data rate, the improved background rejection
1457 and data filtering, and using the experience from DS-50, the short-term storage required at the
1458 experimental site is expected to be 20 TB. The total storage inventory required for the experiment
1459 is expected to be more than 20 PB, including the storage needed for simulated and reconstructed
1460 events.

1461 10.1. Computing systems and data workflow

1462 The primary event processing will occur at the experimental site in the software trigger farm.
1463 Pre-processed data is archived on the temporary storage at the experimental site and copied to
1464 central computing centers (Tier-1/Tier-2). These facilities archive the pre-processed data, provide
1465 the reprocessing capacity, provide access to the various processed versions, and allow analysis of
1466 the processed data. Derived datasets produced in the physics analyses are also copied to the
1467 Tier-1/Tier-2 facilities for further analysis and long-term storage. The Tier-1/Tier-2 facilities also
1468 provide the simulation capacity for the DS-20k experiment.

1469 Bulk data processing is expected to be performed using low cost commodity cluster computing
1470 based on commercial CPUs. Final data analysis will be performed either directly at the Tier-1/Tier-

1471 2 centers or on commercial CPUs hosted at institutes participating in the experiment. There is
1472 also the option of using the considerable free resources available on the Open Source Grid, which
1473 many experiments are currently using to run their reconstruction and analysis jobs.

1474 The amount of short term storage currently available at LNGS for DS-50 consist of 7 TB of
1475 front-end storage used as temporary buffer and located in the underground laboratory, plus 710 TB
1476 of disk space in the above ground computing center for short- and long-term storage of DS-50 data.
1477 From there, raw data are copied to CNAF and Fermilab for reprocessing and analysis. CNAF is
1478 making available 1 PB of disk storage and 300 TB of tape storage. At Fermilab, there is 50 TB
1479 of fault-tolerant disk storage and about 620 TB on the dCache-based tape system for long-term
1480 storage. It is expected that much of this inventory will be recycled for the DS-20k experiment,
1481 aside from what is necessary for ongoing storage of DS-50 raw data. Any necessary additional
1482 tape storage will be purchased and installed. The total amount of storage for the ten years of
1483 data-taking, including calibration and simulated data, is 20 PB of disk storage and 20 PB of tape
1484 storage. The processing power currently used for reprocessing and analysis of DarkSide-50 data
1485 includes a farm of 400 cores at LNGS for production and validation, plus 400 job queues at CNAF
1486 and 25 guaranteed batch slots (soon to increase to 60 guaranteed batch slots) on the Fermilab grid
1487 system.

1488 Currently, a single DS-50 event takes about a half of a second to reconstruct on a typical 2.8 GHz
1489 processor, meaning that 100 dedicated cores can maintain reconstruction in realtime for an event
1490 rate up to 200 Hz. Assuming a factor two increase in the cpu time needed to reconstruct an event,
1491 a factor ten to simulate a full event, a real data plus calibration event rate of 100 Hz, and a sample
1492 of simulated events of the same dimension of the real-data one, DS-20k needs 100 dedicated cores
1493 to maintain reconstruction in realtime of the collected real data + calibration events, and 1000
1494 dedicated cores to produce the simulated samples. Moreover, 2000 physical cores are sufficient to
1495 reprocess all physics events collected in one year in a three month time period.

1496 10.2. Software Environment

1497 DS-20k will adopt an object-oriented approach to software, based primarily on the C++ pro-
1498 gramming language, with some components implemented using other high level languages (Python
1499 etc.). A software framework has been built up during the DS-50 experiment which provides flexi-
1500 bility in meeting the basic processing needs of the experiment, as well as in responding to changing
1501 requirements. In order to support code reuse, build a system optimized for both the offline and
1502 software trigger environment, and provide common user access to low-level algorithms used for I/O
1503 and data persistency, the C++ code will make heavy use of object oriented abstract interfaces
1504 techniques.

1505 The reconstruction combines information from the TPC and the veto detectors. A typical recon-
1506 struction algorithm takes one or more collections of information from the event data model (EDM)
1507 raw data stream as input, calls a set of modular tools, and outputs one or more collections of recon-
1508 structed objects. Common tools are shared between reconstruction algorithms, exploiting abstract
1509 interfaces to reduce dependencies. Analysis of calibration data will also be performed within the
1510 reconstruction and simulation software environment.

1511 DS-20k will produce roughly 2 PB of data annually, combining the data processing, simulation,
1512 calibration, and distributed analysis activities. A data storage and management infrastructure is
1513 necessary to allow efficient storage and access to all this data. Two types of data storage are
1514 foreseen. The first is a file-based data and the second is relational-database-resident data. File
1515 storage is used for bulky items such as event data (physics data, calibration data and simulation
1516 data). Database storage is used for other types of information, including technical data like detector
1517 production, installation, survey and geometry data, online/TDAQ databases, conditions databases
1518 (online and offline), offline processing configuration and bookkeeping information, and to support
1519 distributed data and database management services. File-based storage of C++ objects will be
1520 implemented through the use of ROOT I/O, which provides high performance and highly scalable

1521 object serialization to random-access files. Database storage will be based on SQL-based relational
1522 databases (MySQL and SQLite). All these technologies are widely used and well tested in HEP
1523 experiments.

1524 Computing resources will be accessed through Grid middleware components and services. These
1525 provide services for software installation and publication, production operations, and data access
1526 for analysis through a uniform security and authorization infrastructure, as well as interfaces for
1527 remote job submission and data retrieval, and job scheduling tools designed to optimize utilization
1528 of computing resources. The Grid infrastructure will be based on the infrastructure and the software
1529 tools and services developed for the LHC Computing Grid (LCG) project.

1530 The High-Level Software Trigger (HLST) provides the online event selection. The trigger is
1531 based on an online version of the DS-50 reconstruction software, which has been optimized and
1532 tailored for the DS-20k online environment running on farms of Linux PCs and/or GPUs farms.
1533 Overall, the HLST has to provide the required rate reduction and pre-processing of raw data,
1534 including the production of global event records in analysis EDM format. The HLST will use
1535 the offline computing environment, allowing DS-20k considerable commonality in the design and
1536 management of the selection software itself. This also allows the HLST to use various offline
1537 software components, like detector description, calibrations, EDM, and reconstruction algorithms.
1538 The same infrastructure can be used for data monitoring by simply replacing or augmenting the
1539 selection algorithms with those for monitoring.

1540 10.3. Simulation

1541 G4DS is a Geant4-based simulation toolkit specifically developed for DarkSide. The modular
1542 architecture of the code was developed in order to describe the energy and time responses of
1543 all the detectors belonging to the DarkSide program, namely DS-10, DS-50, and DS-20k, but
1544 other variations of the geometries as well. For each of them, G4DS provides a rich set of particle
1545 generators, detailed geometries, real data tuned physical processes, and the full optical propagation
1546 of the photons produced by scintillation in liquid argon and by electroluminescence in gaseous argon.
1547 The main goals of G4DS are to accurately describe the light response, calibrate the energy responses
1548 in S1 and S2 and the time response expressed by the f_{90} variable, tuning of the analysis cuts and
1549 their efficiency estimation, prediction of the electron and nuclear recoil backgrounds, and definition
1550 of the signal acceptance band.

1551 G4DS tracks photons up to their conversion to photoelectrons, which occurs when a photon
1552 reaches the active region of a photosensor and survives according to the quantum efficiency. The
1553 conversion of the photoelectron into a charge signal is handled by the electronic simulation, an
1554 independent, custom-made C++ code. The electronic simulation embeds all the effects induced
1555 by the photosensors (e.g. after-pulse and cross talk) and by the electronics itself (e.g. saturation).
1556 The electronic simulation also has the option to overlap simulated events and real data baselines
1557 in order to provide more realistic simulations. As output, it produces waveforms for each channel
1558 with the same data format of the real data, in order to be processed by the same reconstruction
1559 code.

1560 G4DS can also track events generated by FLUKA and TALYS simulation codes, previously
1561 developed within the collaboration. The FLUKA simulation is mostly used to study cosmogenic
1562 neutrons and isotope productions, while TALYS is used for (α, n) reactions, both providing
1563 input for the prediction of the nuclear recoil background.

1564 11. THE ReD EXPERIMENT

1565 The ReD project aims to characterize the light and charge response of the LAr TPC to neutron-
1566 induced nuclear recoils, especially at low energy, and to explore for the possible directional de-
1567 pendence suggested by the SCENE experiment [33, 34]. ReD encompasses the irradiation of a

1568 miniaturized LAr TPC with a neutron beam at the INFN, Laboratori Nazionali del Sud (LNS),
1569 Catania. Neutrons are produced via the reaction p(^7Li , ^7Be) from a primary ^7Li beam delivered
1570 by the TANDEM accelerator of LNS. A $\Delta E/E$ telescope, made by two Si detectors, identifies
1571 the charged particles (^7Be) which accompany the neutrons emitted towards the TPC. Neutrons
1572 scattered from the TPC are detected by using an array of nine 3" liquid scintillator (LSci) detec-
1573 tors, using EJ309 liquid scintillator coupled to ET 9821B PMTs. The Si telescope and the TPC
1574 are not at the same height: this is mandatory in order to tag neutron scatterings (n,n') from a
1575 non-horizontal interaction plane. All LSci are placed such to tag recoils having the same energy,
1576 i.e. the same scattering angle with respect to the incident neutron, but different angle with re-
1577 spect to the drift field of the LAr TPC, thus allowing to search for a possible directional response.
1578 Thanks to the support provided by INFN CSN2, the entire set-up has been procured, integrated,
1579 commissioned and deployed to the "80 deg" beamline of LNS. The first beam run test took place
1580 in June-July, 2018.

1581 The core detector of ReD is a custom-made TPC designed by UCLA, which is a miniaturized
1582 version of the LAr TPC for DS-20k. The TPC is a cube with size of about 50 mm. An acrylic vessel
1583 defines the active volume, with the top and bottom acrylic windows ITO coated to allow for the
1584 application of the electric field, and the side ESR-acrylic sandwich reflection panels to maximize
1585 the reflectivity of the chamber. All of the internal surfaces are coated with TPB to wavelength
1586 shift the argon scintillation light. The drift field is kept uniform along the drift coordinate by
1587 means of the field shaping rings, deposited by thin-coating the walls of the acrylic vessel with
1588 ITO. The drift length, extraction length and electroluminescence length of the ReD TPC are
1589 5 cm, 3 mm and 7 mm, respectively. The ReD TPC uses all the innovative features of the DS-20k
1590 design, in particular the optoelectronic readout based on SiPM developed by FBK and the cryogenic
1591 electronics. Two 5x5 cm² tiles are available from FBK, each made by 24 rectangular SiPMs. The
1592 tile on the top of the LAr TPC has a 24-channel readout, in order to improve the (x, y) sensitivity,
1593 while the bottom tile has a standard 4-channel readout. A dedicated 24-channel Front End Board
1594 (FEB) has been designed and produced by INFN-Na in collaboration with INFN-Bo and LNGS.

1595 The LAr TPC is contained in a new cryogenic system. The commissioning of the system was
1596 carried out in Naples. Starting from April 2018, the new TPC and cryogenic system were operated
1597 and tested. Measurements were taken with lasers, low-energy γ sources and neutrons from a
1598 DD generator. This allowed for the first characterization of the LAr TPC and for an integrated
1599 test of: operating procedures, photosensors, DAQ, slow control, data handling and reconstruction
1600 algorithms. The system was successfully operated in single and double phase modes, with a light
1601 yield of about 10 phe/keV at null field. The new LabVIEW-based slow control developed by INFN-
1602 Genova was also integrated and commissioned. The set-up was irradiated in Naples with the DD
1603 neutron gun from the Temple University, such to assess the PSD performance of the LAr TPC.
1604 The run also included one LSci, allowing for the first test of the DAQ for a system made by two
1605 different types of detectors. All nine LSci detectors had been previously tested and characterized
1606 at INFN-Roma1.

1607 The commissioning and the characterization of the system in Naples opened the way for the
1608 deployment of the system at the beamline of LNS. The entire set-up (TPC with cryogenic system,
1609 liquid scintillators with their PMTs and the mechanical support structure) was shipped and re-
1610 assembled in Catania in June 2018. Meanwhile, the beamline had been refurbished on the basis of
1611 the experimental design, optimized with dedicated Monte Carlo simulations, and the mechanical
1612 clearance requirements. The configuration was conceived to allow the tagging of nuclear recoils
1613 between 20 and 100 keV traveling in the parallel and orthogonal directions with respect to the
1614 TPC drift field, by varying the primary beam energy only. Furthermore, having a dedicated liquid
1615 scintillator at small scattering angles opens the possibility to study the response of the TPC to very
1616 low-energy nuclear recoils, O(1 keV). A new scattering chamber was installed with a new beam
1617 pipe. The $\Delta E/E$ telescope was installed inside the vacuum scattering chamber, commissioned and
1618 consists of two Si detector (20 μm and 200 μm thickness, respectively) by ORTEC.

1619 Initially, the cryostat and the liquid scintillators had to be mechanically aligned with respect to
1620 the target with a precision of the order of a few mm. The alignment was performed by following a

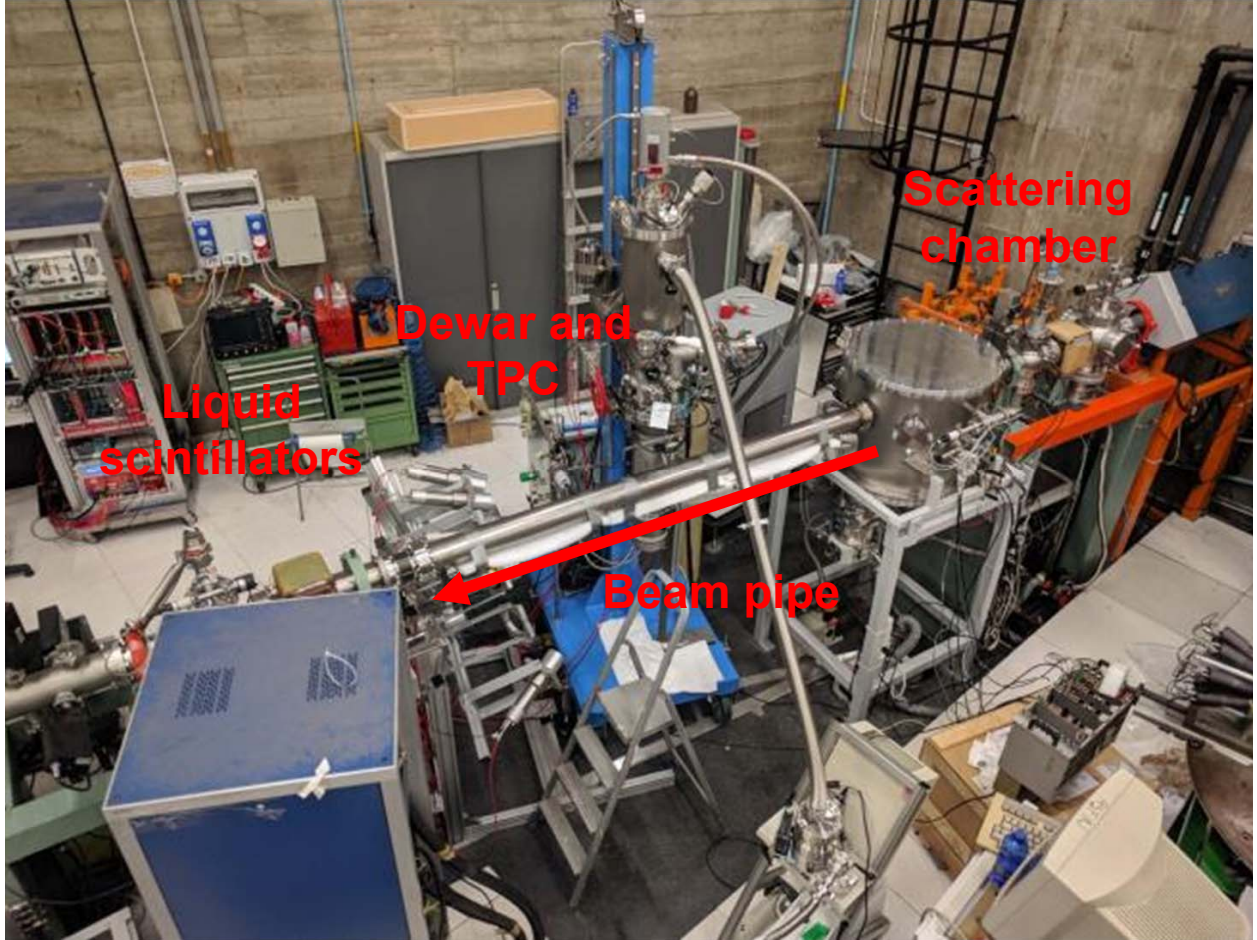


FIG. 24. Photo of the “80 deg” beamline at LNS, after the deployment and alignment of ReD. The targets and the Si telescope are hosted inside the vacuum scattering chamber.

detailed procedure worked out in advance. The ReD set up in Catania is displayed in Fig. 24.

After the scientific approval of the project by the Scientific Committee (PAC) of LNS, a test beam run was scheduled in June-July 2018, meant for technical tests and commissioning. The individual detectors were first commissioned and tested individually, by using the laser and radioactive sources. Light yield and timing were checked by using ^{241}Am and ^{22}Na , respectively. A ^{252}Cf fission neutron source was used to characterize the pulse shape discrimination performance of both the LAr TPC and the LSci detectors. The light yield of the TPC was measured to be about 8.5 phe/keV, while the electron drift lifetime about $250\ \mu\text{s}$, i.e. much longer than the total drift time (about $40\ \mu\text{s}$ at the operational field of $0.2\ \text{V/cm}$), with no hints of degradation in time. The calibration of the LSci detectors indicated a 50 % trigger efficiency at $20\ \text{keV}_{ee}$ and a time resolution of 1.2 ns (rms), which is sufficient for the measurement of the time-of-flight.

The integration of the three detector systems was done with the TANDEM beam. Neutrons were produced by sending a ^7Li 28 MeV beam onto a set of CH_2 targets having thickness between 150 and $250\ \mu\text{g/cm}^2$. The intensity of the beam impinging on the target after the collimator, measured by the Faraday Cup installed at the far end of the beam pipe, ranged between 0.5 and 7 nA. The DAQ software handled 41 readout channels from three FADC boards (CAEN V1730), at 500 MHz sampling rate. A data-to-disk rate of 40 MB/s has been achieved. The Si telescope was placed at 5 deg with respect to the beam. The scattering kinematics allows for two solutions with ^7Be in this direction, one having an associated 7.5 MeV neutron at 22.5 deg, the other with a 2 MeV neutron at 45 deg. The LAr TPC is at 22.5 deg from the target, i.e. it is hit by 7.5 MeV neutrons, produced in association with the ^7Be detected by the Si telescope. The beam energy and the scattering angles

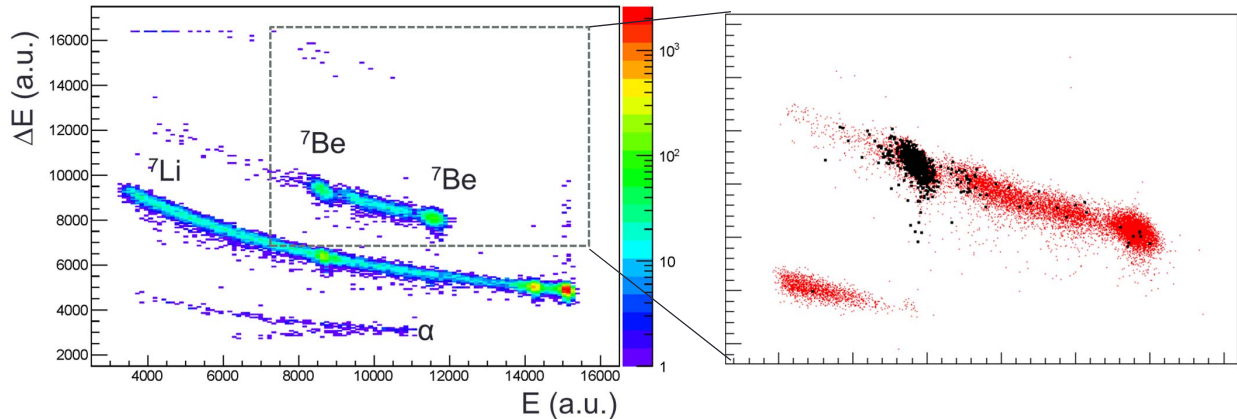


FIG. 25. **Left:** scatter plot of the amplitudes of the ΔE and E Si detectors, placed at 5 deg with respect to the beam axis. **Right:** zoom of the previous scatter plot in the region of the ${}^7\text{Be}$ loci; the black markers are events having a coincident signal in the TPC.

cause the experiment to select nuclear recoils in the TPC of approximately 70 keV.

About 24 hours of data have been taken in the best operating conditions. Data has been taken in both single and double phase modes and with two different trigger schemes, i.e. “Si and TPC”, “Si and any PMT”. The latter scheme yields a large fraction of accidentals, due to the large singles rate of the PMTs (kHz), but it gives potential access to low-energy recoil in the TPC, which would fail to trigger the TPC (low S1, or S2 only). Those events can later be searched for offline in the data analysis. Typical trigger rates were between 0.1 and 0.7 Hz. Events were observed with the proper signature, i.e. a ${}^7\text{Be}$ nucleus detected by the telescope, a nuclear recoil in the LAr TPC and a neutron scattering in the liquid scintillators. Neutron-induced recoils events in the TPC and in the LSci detectors are clearly separated from γ signals, either physical or accidental, by means of pulse shape analysis. As expected, the time difference Δt between the pairs of detectors features a peak of physical coincidences, sitting on a plateau of accidentals. The scatter plot of the amplitudes of the ΔE and E Si detectors is displayed in the left side of Figure 25. It shows the ability of the telescope to discriminate the charged products of the beam-target reactions, i.e. the main ${}^7\text{Li}$ band due to elastic scattering and the two ${}^7\text{Be}$ loci corresponding to the two solutions allowed by kinematics. The right side of Figure 25 shows the same distribution (zoomed), with the black markers referring to the events having a coincident signals in the TPC. As expected, coincident events between Si and TPC are mostly associated to ${}^7\text{Be}$ locus from the “correct” kinematical solution.

After another LNS test beam in September 2018, the ReD TPC has been transported back to Naples, to complete the characterization and re-commissioning in the lab there. Tests have been performed to characterize the basic TPC performance in terms of light yield, uniformity, electric field configuration and S2/S1 ratio in double phase. The system was calibrated with ordinary γ -sources and with an internal ${}^{83m}\text{Kr}$ source, which generates a uniform distribution of mono-energetic events. Activities are still ongoing to characterize the extraction and multiplication fields. A campaign was also carried out at LNS to measure the neutron detection efficiency of the liquid scintillators, using a fission ${}^{252}\text{Cf}$ source. A test beam for the characterization of the neutron beam is going to be performed at LNS in June 2019 and for this run only the Si detectors and the LSci detectors will be deployed.

The ReD project has received scientific approval by the Scientific Committee of LNS (PAC) for a five-week beam allocation that is granted for 2019. Upon completion, the ReD LAr TPC will be transported back to Catania and a new beam run with the full setup will be scheduled.

1673

12. DARKSIDE-PROTO

1674

12.1. Prototype Overview and Status

1675 The objective of the DS-Proto experiment is the construction and operation of a prototype de-
 1676 tector of intermediate size (~ 1 t), to fully validate the new DS-20k technologies for their integrity in
 1677 both the mechanical and functional aspects. The prototype will be constructed using the materials
 1678 planned before screening, in order to speed up the mechanical validation, and will therefore not
 1679 necessarily be a physics-results oriented detector. This may evolve over time to include elements
 1680 of the detectors as materials are screened and made available, and eventually all parts could be
 1681 replaced with radio pure materials to form the basis of another experiment with high-sensitivity to
 1682 low-mass WIMPs. Thus, DS-Proto is not intended to replace validation and tests made in labora-
 1683 tories, but rather complement them with the integration with the rest of the detector. The prompt
 1684 execution of DS-Proto is crucial to fulfill the overall schedule of DS-20k. DS-Proto is on the critical
 1685 path of the project.

1686 The program for DS-Proto is expected to span over three different phases:

- 1687 1. Design, construction and assembly at test site of the LAr TPC, with the size available for two
 motherboards integration;
- 1688 2. Integration of 50 preproduction PDMs to the LAr TPC; assembly, commissioning, and operation
 of full read-out and DAQ for 50 PDMs; The xy resolution and S2 gas pocket optimization will
 be done during this phase.
- 1689 3. Assembly and commissioning of full system, including 370 first production PDMs; full readout
 and DAQ operational; evolution towards final configuration.

1690 The plan for DS-Proto was reviewed, approved, and funded by the CNS2 of INFN. Funding has
 1691 already been secured from the NSF for the development and fabrication of multiple components for
 1692 the TPC, the cryogenics system and resources for kick-starting the UAr extraction site preparations.
 1693 Requests for funding from other participating groups are being evaluated or will be submitted in
 1694 the near future.

1695 In August 2017 the collaboration and LNGS reached and finalized an agreement [60] with the
 1696 Accelerator & Technology Sector of CERN and its Technical Division to construct and commis-
 1697 sion the DS-20k cryogenics at CERN, with support from the Cryogenics Group and the Vacuum,
 1698 Surfaces and Coatings Group (both groups are part of CERN's Technical Division). The extension
 1699 of this program to carry out the first surface operation of DS-Proto at CERN before moving the
 1700 detector to LNGS was agreed by the CERN Accelerator & Technology Sector via an Addendum
 1701 to the above agreement. The necessary space and facilities are the same as for the test on the
 1702 DarkSide-20k cryogenics and are already allocated.

1703 A cryostat for DS-Proto has been built by Tecno Alarm, s.r.l., Roma, and delivered to CERN in
 1704 August 2018 (see Figure 26). The 1 mBq/kg U/Th AISI 304 L Stainless Steel was procured from
 1705 NIRONIT Edelstahlhandel GmbH & Co and it is good enough to be used for a possible physics
 1706 run in LNGS.

1707 Assembly and test of the DS-20k cryogenics will take place at CERN, during the summer and
 1708 last quarter of 2019. Construction of DS-Proto is expected at the end of 2019 or early 2020. The
 1709 first test operation with a reduced number of photosensors is expected by summer 2019, followed
 1710 by a second operation with a full complement of PDMs by early 2020. Full characterization of the
 1711 prototype performance and physics runs will be performed after installation at LNGS. The detailed
 1712 program of the activities to be carried out underground is under study.

1713 We anticipate that, since the DS-Proto will be a stand alone system, sharing the DS-20k cryo-
 1714 genics system at LNGS will not be possible. However over the past few years of R&D for the
 1715 DS-20k cryogenics, we have realized and tested several key components which will be more than
 1716 capable of handling the prototype system. These parts can be used for DS-Proto with minor system
 1717 integration together with most of the DS-50 and existing R&D devices.



FIG. 26. The DS-Proto cryostat and components delivered at CERN.

1722

12.2. The DS-Proto TPC

1723 The DS-Proto TPC mechanics, including the structural elements, the field cage, the reflector cage,
 1724 the transparent cathode, the transparent anode (also serving as a diving bell for the containment
 1725 of the gaseous phase), the SiPM PDM assemblies, the high-voltage feed through system, will all be
 1726 built utilizing, on a scaled down overall dimension, the same design and construction techniques
 1727 foreseen for the baseline of DS-20k (see Figure 27).

1728 The photodetector modules will be arranged to cover the top and bottom of the TPC. Both top
 1729 and bottom planes consist of 185 photodetector modules assembled into 5 SQBs and 4 TRBs. As
 1730 described in section 9, the readout chain will employ commercial components used during the first
 1731 phase, allowing for full digitization of the signals. The final electronics components that will be
 1732 used in DS-20k will be used as they become available at each stage of the development. It is also
 1733 foreseen that the optical signal transmission will be tested on a significant number of channels with
 1734 this detector.

1735 The DS-Proto photosensors are contained in 18 Motherboards made of one set of 5 (SQB) and 4
 1736 (TRB) PDMs on top, and another identical set on bottom. With both planes, the DS-Proto TPC
 1737 requires 370 PDM to be fully covered. Bonding \sim 9000 SiPMs in a few months is one of the most
 1738 critical tasks of this detector, to maintain the overall project schedule. The construction strategy
 1739 relies on two bonding facilities, the first one located at Princeton University and the second one
 1740 at LNGS. According to the experience gained in the past months, a bonding rate of 3 tiles /d is
 1741 feasible. We therefore need 60 d to bond the 370 tiles across the two facilities.

1742 The man power at LNGS can be provided by the NOA contracts, while finding man power at

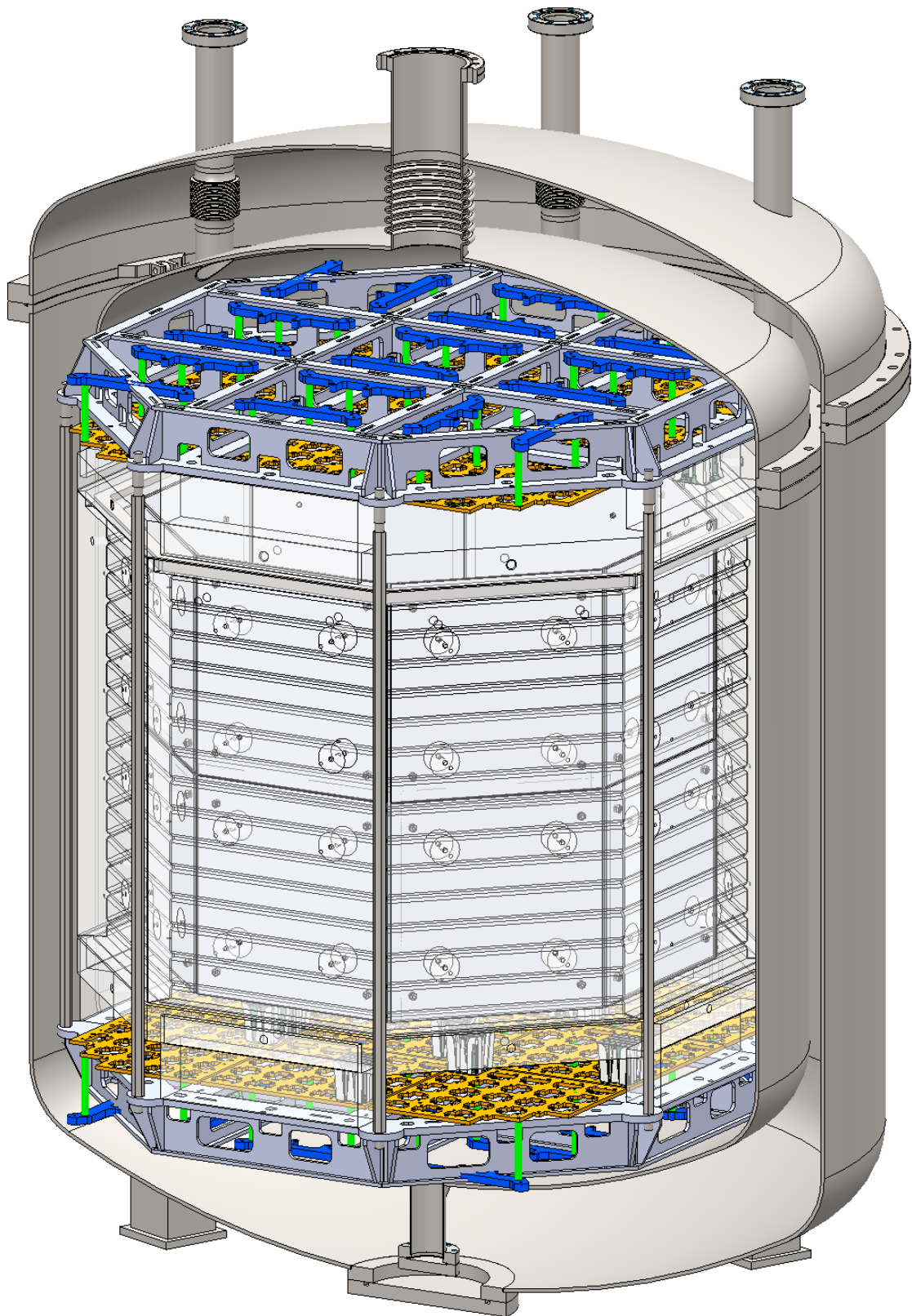


FIG. 27. Conceptual Design of the DS-Proto detector. The cryostat has already been built and delivered at CERN, see Fig. 26.

1743 Princeton University is more challenging. Different options were evaluated, and others are under
1744 consideration. The University of Manchester (UK) has identified a candidate who will spend a
1745 significant amount of time in the course of the next year to be trained, and then do the work. A
1746 tight connection between the two production sites has to be provided, to include the harmonization
1747 of the procedures and quality assurance test. A person to provide this interface is being identified.
1748 LNGS requires a significant increase of man power since after the bonding the tiles will be equipped
1749 with a Front End Board (FEB), and then mounted and tested at LNGS. After the assembly, the
1750 tiles and the FEB will be tested in LN₂. The first Motherboard, made of 25 PDMs, was just
1751 assembled. The Motherboard will be shipped to Napoli, where a comprehensive test at cryogenic
1752 temperature is scheduled.

1753 A powerful test facility has to be prepared at Napoli, requiring extra man power. The procedures
1754 and the tools to ship the Motherboard from Pisa to Napoli and from Napoli to CERN have to be
1755 carefully planned and made available.

1756 12.3. Materials for DarkSide-Proto

1757 Since DS-Proto is a test bench of DS-20k, it won't be used to demonstrate the material radio-
1758 purity requirements of DS-20k, however, it will be built with the goal of achieving the best radio-
1759 purity conceivable at the time of the construction, based on the current results of materials assay
1760 campaign. Additionally, DS-Proto can be used to assess the possible contamination related to the
1761 detector construction procedures (TPC and PE), evidencing material cleaning/handling issues.

1762 The assessment of the DS-Proto radioactive budget will be obtained through the material assay
1763 campaign and the Monte Carlo simulation. The validation of the predictions concerning the neu-
1764 tron/gamma originated by the material contamination will be only possible through data taken
1765 underground with the DS-Proto deployed in a properly shielded environment. A physics run, fo-
1766 cused on the low-mass WIMP search, will be eventually possible with the S2-only analysis in the
1767 keV region. In this context, the minimization of the low-energy gamma background of the prototype
1768 will be extremely important to employ as early as possible.

1769 12.4. Validation tests and operation

1770 Upon successful completion of the test phase of the different parts, we plan to measure the overall
1771 performance of the DS-Proto through some key parameters, such as the S1 light yield, the electron
1772 drift time, electro-luminescence field and gas pocket thickness uniformity for high resolution of S2
1773 signals and the *xy* position reconstruction. For the purpose of optimizing the S2 signals, the first
1774 two Motherboards will be assembled into a small TPC with reduced size drift length (12 cm) to
1775 avoid pile-up (see Figure 28). Full test of the S1 response and therefore of the SiPM readout chain
1776 can be obtained at the surface by switching off the electroluminescence field. The configuration of
1777 the gas pocket (geometry and field) can be varied by changing the distance between the anode and
1778 the wire grid, the width of the gas pocket, as well as the electro-luminescence field. The S2 pulse
1779 shape can be precisely studied along with different gas pocket configurations, aiming to provide
1780 us the best solution for the future LAr TPC design. This set-up will also allow for early studies
1781 of the S2 formation and readout, to be carried out while the pre-production of the remaining
1782 Motherboards of the prototype is ongoing.

1783 13. AAR CRYOSTAT

1784 Figure 1 shows the DarkSide-20k system conceptual sketch, including the copper electromagnetic
1785 and light shield, the Veto detector and the LAr TPC, all contained within the large AAr cryostat.
1786 A ProtoDUNE-like cryostat will be employed to house the LAr bath which the TPC is immersed

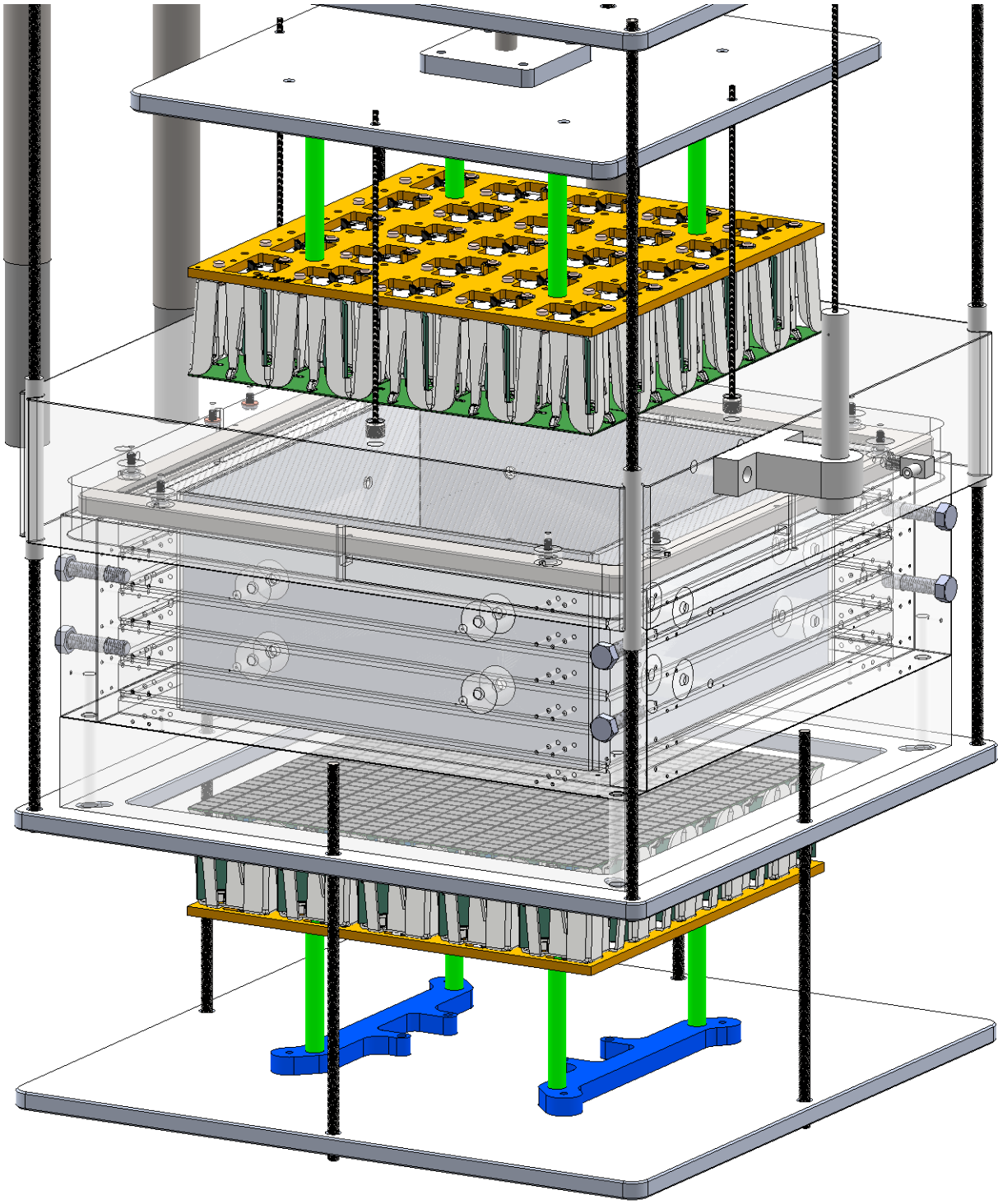


FIG. 28. Schematics of the setup for the optimization of the S2 signals.

in and also acts as the main component of the Veto detector. This allows to minimize the material of the TPC vessel and therefore to limit the possible radio-contaminations very close to the active volume.

Figure 29 shows the finished ProtoDUNE cryostat internal view while being cleaned, as well as the layout of passive thermal insulation materials that were used to construct the cryostat. The design concept for the DS-20k cryostat is based on the experience matured with the construction

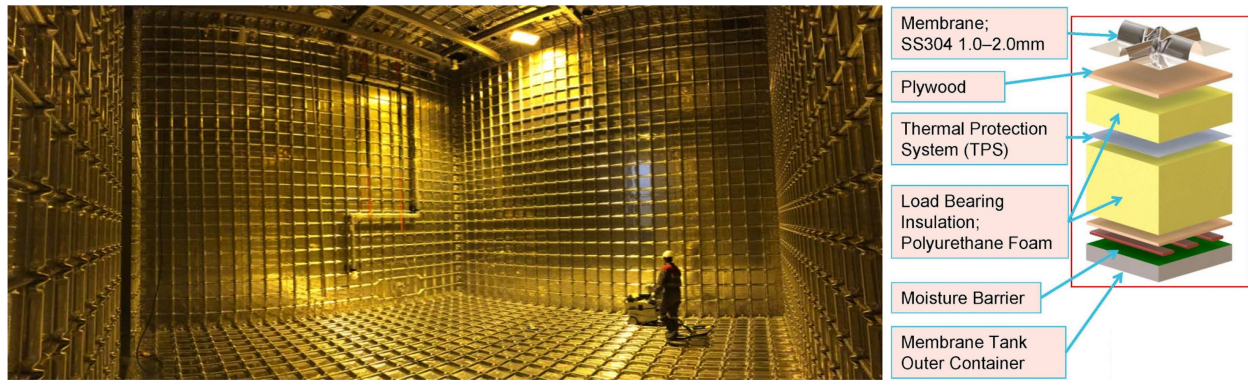


FIG. 29. **Left** Interior view of the ProtoDUNE cryostat used for the single phase LAr TPC test at CERN. **Right** Cryostat insulation construction details from GTT.

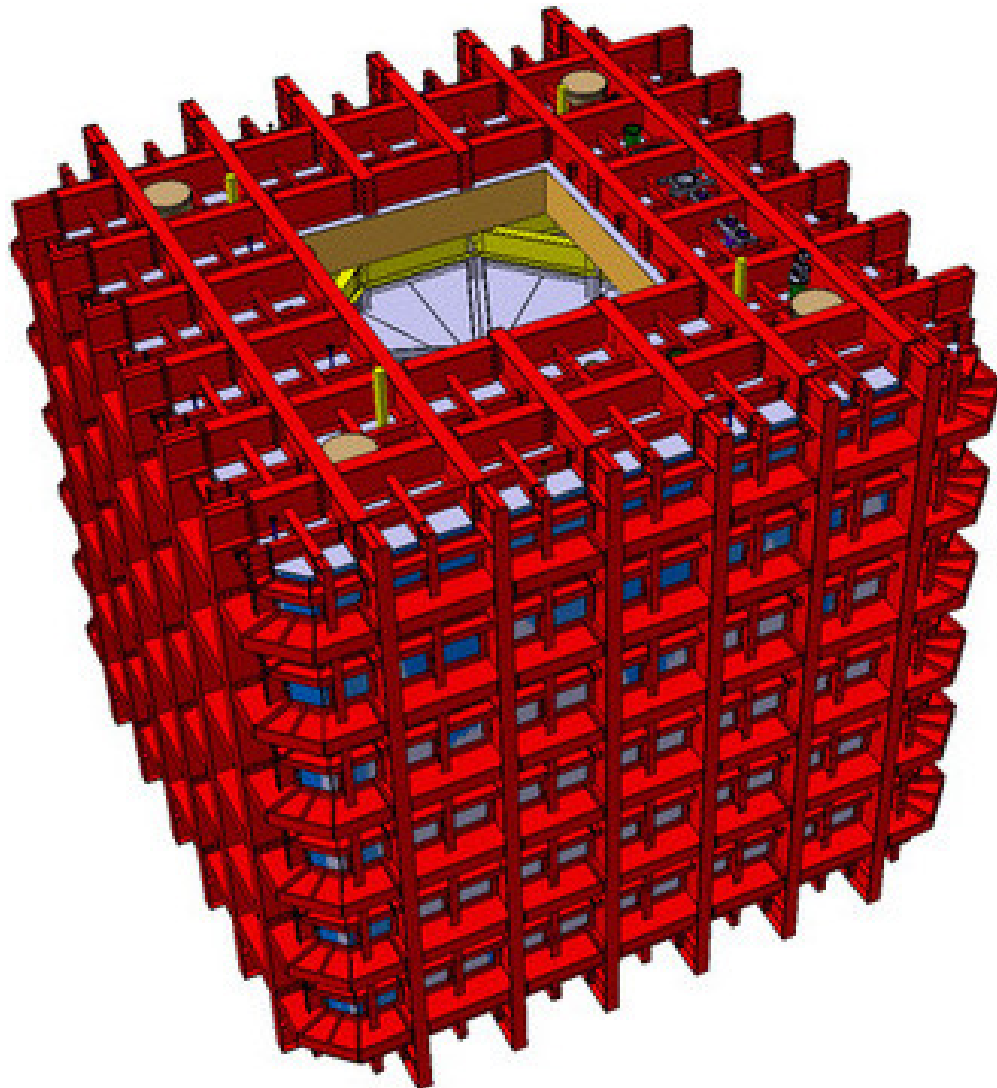


FIG. 30. 3D conceptual external view of the DS-20k AAr cryostat.

¹⁷⁹³ of ProtoDUNE cryostat. The technique is adopted from the LNG (Liquified Natural Gas) carriers
¹⁷⁹⁴ and vessels, which has proven over many years its solidity and reliability.

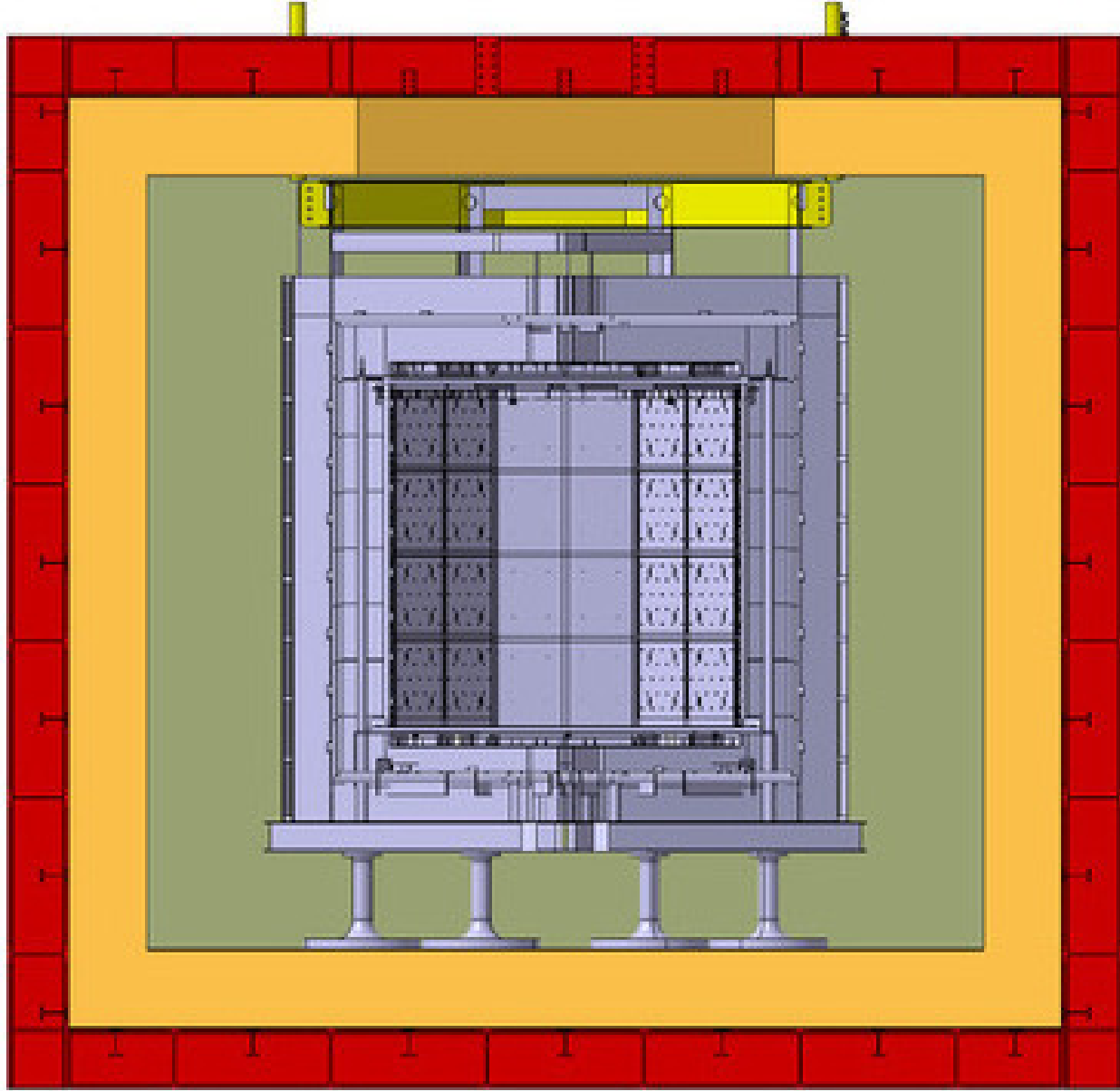


FIG. 31. Cross-sectional view of the large AAr cryostat containing the LAr TPC and Veto detectors and showing the top-cap concept.

Two cryostats of the same size as the one proposed here have been constructed at CERN and one of them has been brought into operation in the second half of 2018. The experience gained there in the design, construction and operation will be fully translated to the DS-20k project, through the involvement of the CERN group that was responsible for the construction and operations of the ProtoDUNE cryostat. For that reason, the same mechanical constraints, dimension and thermal properties have been kept. The DS-20k cryostat is an improved version based on the experiences gained during the construction of the two ProtoDUNE cryostats, namely optimized fabrication and construction and access specific for DS-20k project. A 3D conceptual view of the external part of the cryostat being planned for DS-20k is shown in Figure 30.

To make it as easy as possible for the access and support of the sub-systems of the TPC and the Veto detectors, all components will now be inserted from the roof of the cryostat, with a “closing cap” concept being implemented. This has been previously deployed by the CERN team during other large-dual phase TPC R&D experiments and tested with the construction and operation of

Element	Inlet Purity [ppm]
CH ₄	<0.25
CO	<0.1
CO ₂	<0.1
H ₂	<1
H ₂ O	<1
N ₂	<1
O ₂	<1

TABLE VII. Inlet argon purity required for operation of the DarkSide-20k getter.

the first demonstrator for the ProtoDUNE project. A cross-sectional view of the concept is shown in the right side of Figure 31. The plan is to assemble the bottom and sides of the Veto detector using a temporary support frame underneath the Veto detector, and then lower the TPC down into the Veto detector while it is attached to the closing cap, see Figure 23. Once in place, the remaining parts of the Veto detector could be assembled, the entire detector system support transferred to the detector support system of the cryostat, and finally the temporary supports of the Veto detector that we required during construction removed. At this point, the two detector volumes, that of the TPC and that of the Veto, would be filled simultaneously such that the LAr height in both volumes is equal at all times in order to reduce the mechanical stress on all of the detector components.

As mentioned in Sec. 5, the AAr cryogenics system will be built based on the combined experiences of the ProtoDUNE cryogenics and the DS-50 cryogenics. The final optimization decision will be made taking into account that the different requirements of the AAr cryostat for DS-20k compared to those for ProtoDUNE, and the available space in Hall C of LNGS. Penetrations on the roof of the cryostat are being finalized such to meet the requirements of the other sub-systems, as well as to provide the mechanical stability of the cryostat ceiling. The design and development plan will follow the successful experience of ProtoDUNE, with expert engineering assistance provided by the CERN group, while already a firm baseline design is in place and schematically shown in the left side of Figure 16, along with the rest of the DS-20k cryogenics system.

14. ARGON PROCUREMENT AND PURIFICATION

A broad strategy has been developed to increase the production of UAr to procure the target required for DarkSide-20k. The Urania project will extract and purify the UAr from the CO₂ wells at the Kinder Morgan Doe Canyon Facility located in Cortez, CO, at a production rate of 250 kg/d. It will be necessary to make a final chemical purification of the UAr before deployment into the LAr TPC (driven by the filtration capacity of the getter purification unit), bringing the chemical impurity levels to those shown in Table VII. Additionally, it would be beneficial to further deplete the UAr of ³⁹Ar, giving extended sensitivity to DarkSide-20k and producing argon with a level of ³⁹Ar that is acceptable to be used in an experiment such as Argo. The Aria project will serve to chemically purify the UAr to better than the levels shown in Table VII using a cryogenic distillation column called Seruci-I. The ultimate goal of the Aria project is to process argon through Seruci-I to achieve an additional depletion factor between 10 and 100 (on top of the reduction of ³⁹Ar already seen in the UAr).

The procurement of the UAr for DarkSide-20k is broken into two main operations, extraction of the UAr by Urania and then chemical purification by Aria using Seruci-I.

14.1. Urania

The Urania project will extract at least 60 t of low-radioactivity UAr, providing the required 51.1 t of UAr to fill DarkSide-20k. The Urania project will also lay the groundwork for UAr procurement for future, larger argon-based detectors such as Argo. The goal of the Urania project is to build a

1845 plant capable of extracting and purifying UAr at a rate of 250 kg/d, from the same source of UAr
1846 that was used for the DarkSide-50 detector.

1847 The opportunity to build Urania has grown from the strong relationship between the DarkSide
1848 Collaboration and the Kinder Morgan Corporation. Based on gas analysis of the Cortez stream
1849 provided to Kinder Morgan by the DarkSide Collaboration during the extraction of the DarkSide-50
1850 UAr target, a major industrial partnership between Kinder Morgan and Air Products was estab-
1851 lished in order to extract helium from the CO₂ at Kinder Morgan's Doe Canyon facility. The Air
1852 Products helium plant began operation in July 2015 and presently supplies 15 % of the production
1853 rate to the National Helium Reserve.

1854 The DarkSide Collaboration reached an agreement with Kinder Morgan to feed the Urania plant
1855 with a small fraction (15 %) of the gas stream returned to Kinder Morgan by Air Products after
1856 helium extraction. This gas stream holds two significant advantages over the gas stream used to
1857 extract the UAr for DarkSide-50: it is completely dehydrated, and it contains only trace amounts
1858 of helium. These features greatly simplify the process for UAr extraction by the Urania plant,
1859 while ensuring the same radioactivity levels, or better. Argon from the active CO₂ wells in south-
1860 western Colorado have been found to contain very low levels of the radioactive isotope ³⁹Ar, with
1861 the concentration shown to be a factor of $(1.4 \pm 0.2) \times 10^3$ below that of argon derived from the
1862 atmosphere [5]. In an effort lasting more than 5 years, DarkSide-50 collaborators at Princeton
1863 and Fermi National Accelerator Laboratory (Fermilab) extracted and purified (156 ± 1) kg of UAr,
1864 slightly more than the (153 ± 1) kg needed for the target material in the DarkSide-50 detector.

1865 The Urania feed gas stream is $\sim 95\%$ CO₂, plus a few percent of N₂, one percent CH₄, 430 ppm
1866 of UAr, and traces of higher hydrocarbons. The processing scheme of the UAr extraction plant is
1867 optimized for this feed composition in order to achieve an UAr purity of better than 99.9 %. A
1868 modular plant consisting of skid-mounted units deployable on concrete platforms is being designed
1869 to carry out the processing.

1870 The UAr extraction plant will consist of three gas-processing units, as shown in Fig. 32, followed
1871 by a cryogenic distillation unit. The gas-processing units are two CO₂ liquefier/strippers followed
1872 by a pressure swing adsorption unit (PSA). The first liquefier accepts gas at (49 ± 1) bar, with
1873 a flow rate of 16 250 std m³/h and a temperature of 5 °C. At these conditions, the CO₂ partially
1874 condenses and the stream is separated into 2-phases (gas/liquid) as it goes to the first stripper.
1875 In the column a controlled quantity of heat is given by a hot fluid working between the chiller
1876 condenser and the column reboilers. The light products are vaporized and recovered from the top
1877 of the column in gas phase. The heavy products (mainly CO₂) are collected from the bottom,
1878 compressed to 120 bar and returned to Kinder Morgan as a liquid. The light products coming
1879 from the column head are cooled down in the second step to approximately -50 °C and sent to the
1880 second stripper. The first column produces 1300 std m³/h of product flow, a factor of 5 reduction
1881 in the amount of gas to be processed by the more complex downstream units.

1882 The second liquefaction and stripping unit further reduces the CO₂ content, in a similar process
1883 as the first stripping unit. The separated CO₂ is joined with that from the first unit and returned
1884 to Kinder Morgan. The product gas from the second stripper is re-heated in a heat exchanger
1885 and delivered to the PSA unit, which separates the light fractions, including the argon, from the
1886 remaining CO₂. The PSA is composed of four adsorption beds to allow continuous operation with
1887 short time adsorption cycles. The desorption of CO₂ is made by decreasing the pressure on the bed.
1888 To optimize the performances, the operation of the adsorbers are combined by coupling the purge
1889 and pressure swing phases. At the outlet of the PSA adsorption tanks, one buffer tank is provided
1890 in order to dampen process fluctuations and allow for continuous operations of the final distillation
1891 process. The PSA off-gas is delivered to a recycle compressor and sent back to the second CO₂
1892 stripper inlet for reprocessing.

1893 The PSA is the most critical unit of the entire process since the dynamic adsorption conditions
1894 are the most difficult to simulate and predict. Optimization of the sorbent and other operational
1895 parameters is being done via a small scale lab setup in which breakthrough tests are being performed
1896 for a variety of gas species. A picture of the test setup being used is shown in Fig. 33. Sorbent
1897 screening relies on measurements of the breakthrough curves of the different gas species for the

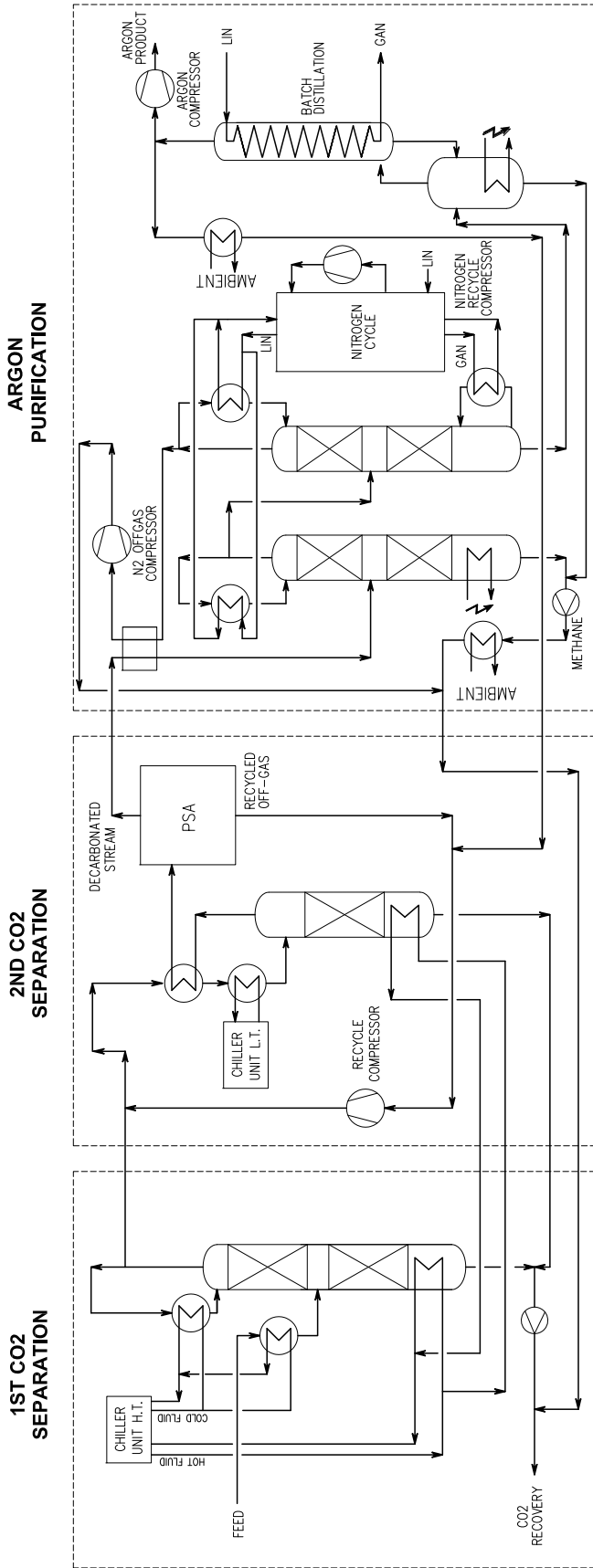


FIG. 32. Process Flow Diagram (PFD) for the Urania UAr extraction plant.



FIG. 33. Test plant in use at Università degli Studi di Napoli “Federico II” for the characterization and selection of sorbents for the PSA unit of Urania.

1898 candidate sorbents. A selection of sorbents which could work for the PSA unit have already been
 1899 identified, while the final selection of the exact sorbent to be used in the UAr extraction plant will
 1900 be determined by the test results and consultation with the contracted company who will build the
 1901 plant.

1902 The final unit of the UAr extraction plant consists of three cryogenic distillation columns. The
 1903 CO₂-free product coming from the PSA plant is pre-cooled and sent to the first column, which
 1904 works at a lower pressure (~9 barg) for the removal of CH₄. The second column is used to remove
 1905 the remaining light fractions from the resulting N₂-rich stream, and the third to perform the final
 1906 purification of the UAr using a batch distillation process. In addition to removing the CH₄ and N₂
 1907 at this point, any ⁸⁵Kr present in the stream will also be removed by the series of three cryogenic
 1908 distillation columns. The CH₄-rich and N₂-rich distillation wastes are returned to Kinder Morgan
 1909 along with the CO₂. The final product, 99.9 % pure UAr, will be taken in liquid form from the
 1910 top of the last column and a small portion collected into a tank to check the quality of the argon.
 1911 The majority of the liquid UAr will be sent to the appropriate cryogenic vessels for shipment to
 1912 Sardinia, where it will undergo final chemical purification by the Seruci-I column.

1913 The Urania project has recently made significant strides, most importantly with the opening
 1914 of the tender for the construction and shipment of the argon extraction plant by the INFN. The
 1915 opening of the tender has officially marked the start date for the progression of the sub-project
 1916 schedule, and the timeline for the extraction of the 60 t of UAr required for the DS-20k experiment
 1917 has now been set and has been integrated with the overall project schedule. It is now expected
 1918 that the tender process will close at the beginning of the fourth quarter in the 2019 calendar year,
 1919 and at that point a contract will be executed for the construction and delivery of the plant to the
 1920 extraction site in Colorado, USA.

1921 The tender for the construction of the argon extraction plant has been opened and the winner
 1922 will be selected and contract signed by the end of October, 2019. The plant will be delivered to the
 1923 Kinder Morgan Doe Canyon Facility by the end of 2020 calendar year. The current plan is to install
 1924 and commission the plant in the first three quarters of 2021 calendar year, allowing for extraction

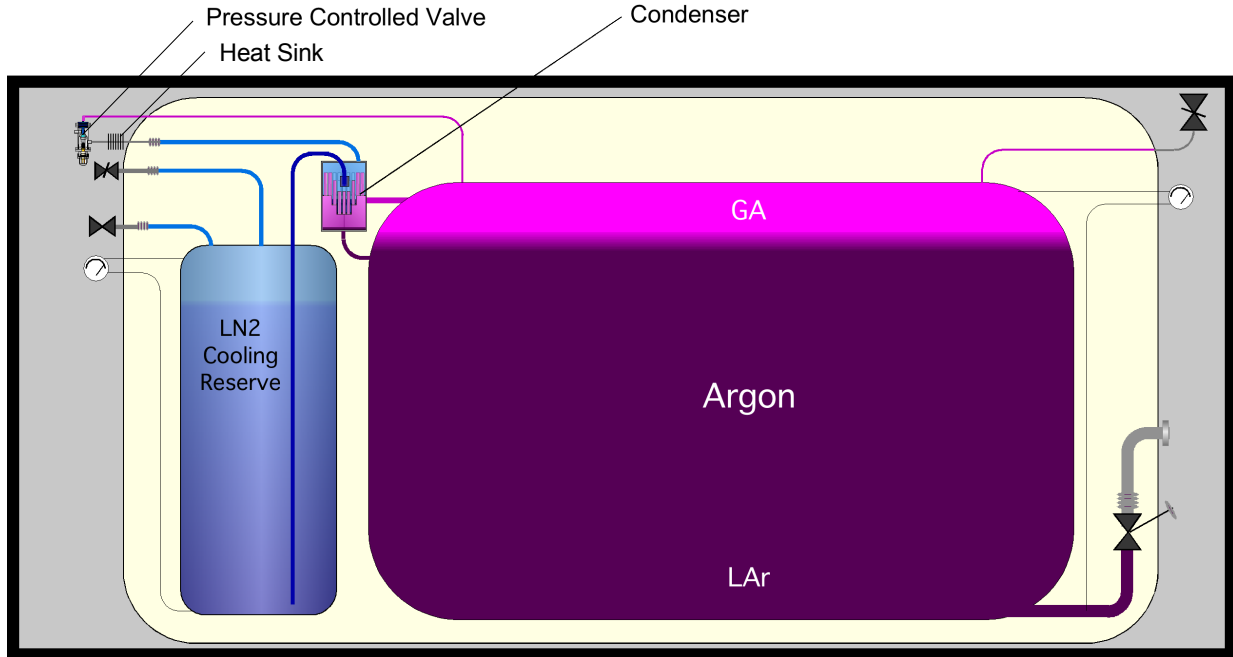


FIG. 34. Schematic view of the cryogenic shipping vessel design, one of the two options for argon shipment from Colorado to Sardinia.

1925 of the 60 t of UAr by the middle of the 2022 calendar year, in order to meet the DarkSide-20k
 1926 schedule. The preparation of the extraction site is being planned now and will be managed by the
 1927 collaboration with help from the Kinder Morgan CO2 Company and the contractors hired to carry
 1928 out the work. Site preparations for developing the facility before the arrival and installation of the
 1929 plant will begin as soon as the necessary land development permits have been secured and the RFQ
 1930 process has been completed.

1931 The shipment from Colorado to Sardinia will be done by boat in order to minimize the cosmic
 1932 activation of the argon. For the shipment of the UAr from Colorado, two options are under
 1933 investigation. The first option, which was determined to be the baseline method, is to ship the
 1934 UAr in liquid phase using custom built cryogenic vessels. This is a more efficient and cost effective
 1935 method, compared to shipping the UAr in gas phase. The custom built cryogenic vessels will have
 1936 a double wall structure, there will be two inner volumes with the larger one containing the UAr and
 1937 the smaller containing LN₂. The outer volume would be at ultra-high vacuum to thermally insulate
 1938 the two inner volumes from the atmosphere at ambient temperature. During the transport, a LN₂
 1939 fed condenser would slowly re-liquify the UAr as it evaporated away, ensuring that none of the UAr
 1940 would be lost during the trip. A schematic view of the cryogenic vessel design is shown in Fig. 34.
 1941 A minimum of five cryogenic vessels is foreseen enabling one for Urania production, one for Aria
 1942 feed, one for Aria production, and two traveling between Sardinia and LNGS for delivery and then
 1943 LNGS and Sardinia for further production of UAr, at all times.

1944 In the case of cryogenic shipping, the extracted UAr will be shipped to Sardinia in batches of
 1945 11 t (roughly every 100 days) in liquid phase, also eliminating the need to liquify the UAr to be
 1946 reprocessed by the Aria column. After chemical purification in Aria, the UAr will then be shipped
 1947 to LNGS, also in batches of 11 t, and stored in the argon recovery system. In order to minimize
 1948 the exposure to cosmic rays, the argon will be stored underground at Seruci and/or LNGS for any
 1949 necessary long durations.

1950 The second option that is now being investigate as an alternative, is to ship the UAr in high-
 1951 pressure gas cylinder placed in trailers which can be hauled by trucks. This option is made possible
 1952 by special cylinders which allow for the storage of argon at pressures up to 400 bar. With pressures
 1953 of this magnitude, and cylinders that are able to be the size of large trailers, the number of trailers

1954 that would be required for the total DS-20k detector target is something that is manageable, on the
1955 order of 10 to 20 depending on the storage pressure. The overall benefit of moving to this option,
1956 instead of going with the cryogenic vessel option, is that the gas can be maintained in the cylinders
1957 for years without the need of any type of consumable to prevent the loss of the argon. This would
1958 basically eliminate the risk of losing any of the UAr during the transport and storage, other than
1959 potential loss of the shipment.

1960 The Urania project team is now collecting all of the information that is required to make the
1961 technical and economic assessment of the two options. Based on the technical risks and the economic
1962 impact on the project, the option that is best for the overall project will be chosen.

1963

14.2. Aria

1964 The aim of Aria is to perform chemical purification of the UAr extracted by Urania. Aria will also
1965 be the test bench to develop active depletion of ^{39}Ar from the UAr to possibly provide DAr targets
1966 for future larger-scale LAr detectors. Aria consists of a 350 m tall distillation column, Seruci-I,
1967 capable of separating isotopes with cryogenic distillation, a process that exploits the tiny difference
1968 in volatility due to the difference in isotopic mass [61–66].

1969 The design of the plant started in April 2015 with seed funding from the US NSF through
1970 PHY-1314507. Aria is to be installed in a underground vertical shaft of 5 m diameter and 350 m
1971 depth, located at the Seruci mine campus of CarboSulcis, a mining company owned by the Regione
1972 Autonoma della Sardegna (RAS). In February 2015 a proposal was submitted to the Italian INFN
1973 and RAS, and the funding for the Seruci-I column was approved on July 24, 2015. Construction
1974 of Seruci-I modules started in September 2015 in a Italian company.

1975 The measurements of the relative volatility of argon isotopes [67–69] and their theoretical inter-
1976 pretation [70–72] marked the birth of the Italian school of condensed matter in Genoa and Milan.
1977 The study of the relative volatility of argon isotopes was recently revisited [73, 74] and shows a
1978 promising path for the separation of ^{39}Ar from ^{40}Ar . Following these studies, DarkSide collabora-
1979 tors developed the framework for comparing ^{39}Ar to ^{40}Ar . Algorithms developed to calculate the
1980 relative volatility of argon isotopes, based on the extensive and detailed models available in the
1981 literature, predict that the volatility of ^{39}Ar relative to ^{40}Ar is 1.0015 ± 0.0001 , and that it stays
1982 constant within theoretical uncertainties in the range of temperatures practical for the distillation
1983 of argon (84 K to 100 K). The small volatility difference can be used to achieve active isotopic
1984 separation by using a cryogenic distillation system with thousands of equilibrium stages.

1985 Design of the Aria plant was optimized on the basis of high-precision numerical methods for
1986 estimating the isotopic separation of ^{39}Ar from ^{40}Ar . DarkSide Collaborators developed two in-
1987 dependent numerical codes, one based on the McCabe-Thiele method [75], and a second based on
1988 the Fenske-Underwood-Gilliland (FUG) method and its derivative, the Wynn-Underwood-Gilliland
1989 (WUG) method [76–78]. Calculations for the isotopic separation power of ^{39}Ar from ^{40}Ar and of the
1990 processing rate were performed with the custom codes, as well as with software routines supported
1991 by commercial chemical engineering CAD programs, such as Aspen [79].

1992 Fig. 35 illustrates the core of the process for isotopically separating ^{39}Ar from ^{40}Ar . The process
1993 consists mainly of two loops: the process loop where the argon is distilled and the ^{39}Ar is separated
1994 from the ^{40}Ar , and the refrigeration loop where nitrogen gas and liquid is used to evaporate and
1995 to condense the argon. Most of the heat is recovered, thanks to the compressor that pumps the
1996 nitrogen gas evaporated in the condenser to the reboiler and to the pumps that move the liquid
1997 nitrogen produced in the reboiler to the condenser, making the system as efficient as possible. In
1998 Fig. 35 all the sub-parts of the plant are represented:

- 1999 • Feed station, to filter and regulate the feed to the column;
2000 • Compressor station, to bottle the distillate at the bottom;
2001 • Vacuum system, to keep a good vacuum in the cold-box, in order to minimize the heat losses;
2002 • LN₂ storage;

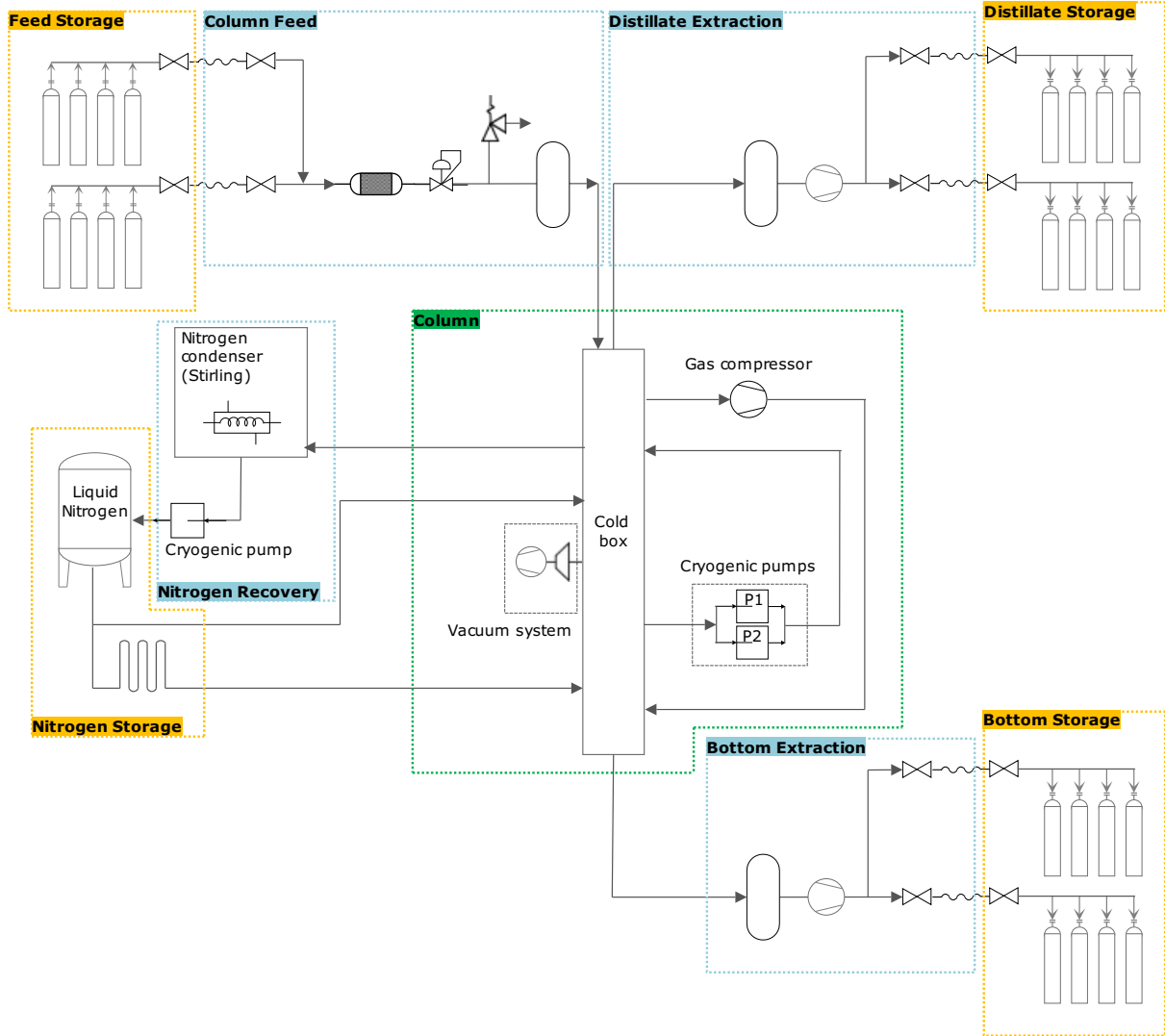


FIG. 35. Block diagram of the cryogenic system of the Aria plant.

- 2003 • Nitrogen condenser system, consisting of 4 Stirling cryo-refrigerators needed to re-condense the
2004 nitrogen, used in a closed loop.

2005 Seruci-I will consist of 28 modules of 12 m height, plus a top module (condenser) and a bottom
2006 module (reboiler).

2007 Calculations indicate that Seruci-I will be able to process UAr at a rate of $O(1 \text{ t/d})$ removing all
2008 chemical impurities (including traces of N_2 , O_2 , and Kr) with a separation power better than 10^3
2009 per pass. Additionally, Seruci-I can be used in a different mode of operations to test the isotopic
2010 separation of the argon, in order to further reduce the ^{39}Ar content in the UAr. The same models
2011 which have been used to calculate the chemical purification rate, have also been used to show that
2012 Seruci-I would be able to isotopically separate the UAr at a rate of 10 kg/d , while obtaining an
2013 ^{39}Ar depletion factor of 10 per pass.

2014 All modules for Seruci-I have already been built and passed a series of quality assurance checks.
2015 During the first check, the process column and all the service pipes were individually checked for
2016 leaks at room temperature. Then, the pipes were wrapped with super-insulation and everything
2017 was assembled into the cold box. The second check was a full module check, with an additional
2018 check done on the bottom reboiler module at 77K. To date, all modules have passed both checks

2019 at room temperature and the bottom module has passed the final cold temperature check.
2020 Seruci-0 is a test column that is made with the Seruci-I top and bottom modules and a single cen-
2021 tral module. The goal of Seruci-0 is to confirm the proper operation of the three main components
2022 of the Seruci-I column, as well as to gain experience in operating the column on a smaller scale
2023 and to put in place the standard operating procedures. The three modules have been completely
2024 installed in a outdoor assembly hall at Nuraxi Figus, Italy, seen in Figure 36. During the last
2025 months, all the leak-check tests have been performed in order to guarantee the design tightness.
2026 Moreover, most of the plants have been installed and assembled in the area surrounding the column
2027 itself. Moreover, two concrete platforms were built: they currently host the liquid nitrogen dewar
2028 and the accessory plants, the cooling machine (chiller) and a control room to host people on shift
2029 and to organize the slow control. Test operations of Seruci-0 will start in summer of 2019.

2030 Concerning the installation of Seruci-I, all the documents needed for the authorization request
2031 for installation were submitted in May 2018 to the competent authorities. During the first half
2032 of 2019, several meetings have been held, both with the fire brigade and with other local and
2033 county offices, entities and authorities. The authorization were eventually obtained. During 2018 a
2034 complete cleaning and preparation of the well at the Seruci site has been performed. A well-defined
2035 coring procedure was concluded in 2018. After the examination of the rocks samples, the design for
2036 the Seruci-I supporting structure was detailed. The tender was completed in Autumn 2018, and
2037 at the beginning of 2019 a carbon steel sample platform was delivered to the mine and installed in
2038 the Seruci well. The test was successful and was very useful in order to define all installation steps.
2039 The goal is to receive all of the platforms by the end of May 2019 and to install them inside the
2040 well by the end of 2019.

2041 14.3. DArT

2042 The DArT experiment will re-use the ArDM infrastructure with minimal modifications made
2043 and will consists of a radio-pure single-phase LAr detector with about one liter contained inside of
2044 its active volume. The DArT detector itself will be placed inside the middle of the ArDM vessel.
2045 DArT will be filled with argon to be tested in order to measure the content of ^{39}Ar . The detector
2046 will be readout by two cryogenic SiPMs each with a surface area of 1 cm^2 . The SiPMs and the
2047 readout electronics will come from the DS-20k production chain.

2048 The ArDM detector will act as an active veto against internal and external radiation. For this
2049 purpose, we are building a dedicated single phase setup with a new set of low-radioactive photo-
2050 multipliers (PMT). However, we will also retain the entire present double phase setup for later use,
2051 e.g. for measurements of large quantities of depleted argon.

2052 Extensive GEANT4-based simulations were performed using the Monte Carlo simulation package
2053 inherited from the DarkSide-50. These simulations show that DArT will achieve a sub-% measure-
2054 ment when operated inside the ArDM detector, for ^{39}Ar concentrations a factor of ten smaller
2055 than those of AAr, and in about a week of running. A 2% measurement could be made for ^{39}Ar
2056 concentrations as low as two orders of magnitude (statistical uncertainty only) smaller than those
2057 in AAr. This setup will also be useful to characterize the performance of Aria, which is expected
2058 to suppress the ^{39}Ar content by a factor of 10 per pass.

2059 A very important addition to the setup described above will consist of adding a 6 t lead belt
2060 about 140 cm tall around the ArDM vessel, at the mid-height position. This will suppress the
2061 impact of external photons that dominate the background budget and allow for the measurement
2062 of even larger ^{39}Ar depletion factors, corresponding to that of the UAr. If the depletion levels are
2063 those already measured in the past (i.e. of 1400), it will be possible, according to our simulations,
2064 to measure them with a 7% uncertainty in about a week of running. Upper limits can be set on
2065 depletion factors of order 25 200 (statistical uncertainty only), i.e. UAr with one distillation pass
2066 in Aria.

2067 The argon from Urania is expected to be available only after mid-2021. However, it is planned
2068 that after the run of DS-50 at LNGS, presumably at the end of 2019, its argon will be measured with

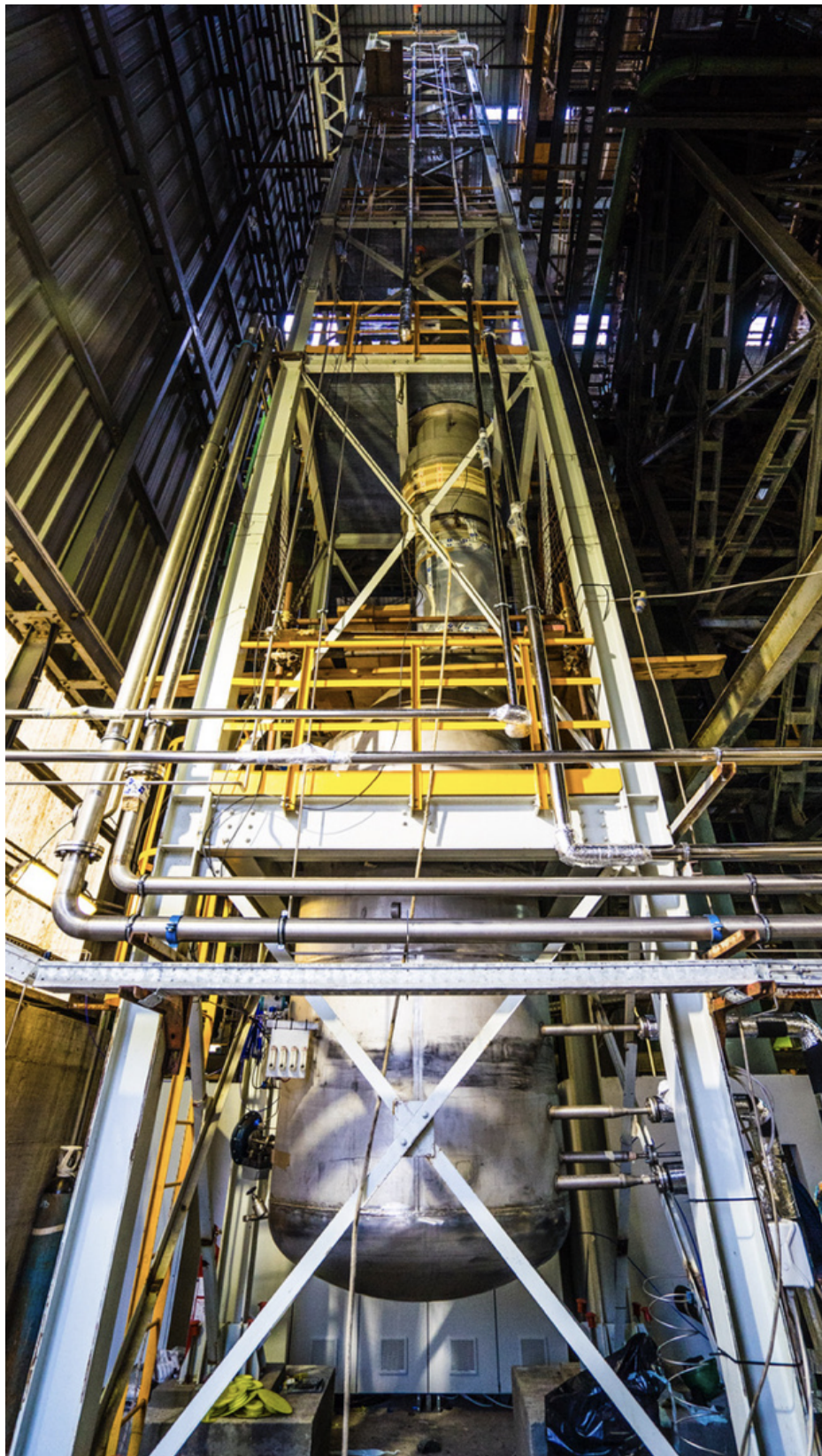


FIG. 36. The Seruci-0 cryogenic distillation column, installed in the *Laveria* building of Carbosulcis in Nuraxi Figus, Sardinia, Italy.

2069 DArT to cross-check the original measurement taken with DS-50 and to test the new setup. This
2070 DArT experiment is expected to become a useful facility within LSC for the years to come, since
2071 it will be needed to measure samples of the extracted argon from Urania over time. An Expression
2072 of Interest and a TDR were recently submitted to the LSC Directorate. Detector construction in
2073 all collaborating institutions has already started.

- 2074 [1] CERN, *CERN Yell. Rep. Mon.* (2017).
- 2075 [2] P. A. Amaudruz et al. (The DEAP-3600 Collaboration), *Phys. Rev. Lett.* **121**, 071801 (2018).
- 2076 [3] R. Ajaj et al., *arXiv:1902.04048v1* (2019).
- 2077 [4] P. Agnes et al. (The DarkSide Collaboration), *Phys. Lett. B* **743**, 456 (2015).
- 2078 [5] P. Agnes et al. (The DarkSide Collaboration), *Phys. Rev. D* **93**, 081101 (2016).
- 2079 [6] P. Agnes et al. (The DarkSide Collaboration), *Phys. Rev. D* **98**, 102006 (2018).
- 2080 [7] P. Agnes et al. (The DarkSide Collaboration), *Phys. Rev. Lett.* **121**, 081307 (2018).
- 2081 [8] P. Agnes et al. (The DarkSide Collaboration), *Phys. Rev. Lett.* **121**, 111303 (2018).
- 2082 [9] B. Abi et al. (The DUNE Collaboration), *arXiv:1706.07081v2* (2017).
- 2083 [10] R. Acciarri et al. (The DUNE Collaboration), *arXiv:1601.05471v1* (2016).
- 2084 [11] Heraeus Deutschland GmbH & CO. Kg, *CLEVIOS™ PEDOT* (2019).
- 2085 [12] G. Angloher et al. (The CRESST Collaboration), *Eur. Phys. J. C* **72**, 1971 (2012).
- 2086 [13] D. S. Akerib et al. (The LUX Collaboration), *Phys. Rev. Lett.* **118**, 021303 (2017).
- 2087 [14] X. Cui et al. (The PandaX-II Collaboration), *Phys. Rev. Lett.* **119**, 181302 (2017).
- 2088 [15] E. Aprile et al. (The XENON Collaboration), *Phys. Rev. Lett.* **121**, 111302 (2018).
- 2089 [16] T. A. Collaboration, *CERN Doc. Serv.* (2018).
- 2090 [17] H. Nelson (For The LZ Collaboration), Presentation at DM 2014 (2014).
- 2091 [18] V. A. Kudryavtsev (The LZ Collaboration), *AIP Conf. Proc.* **1672**, 060003 (2015).
- 2092 [19] E. Aprile (For The XENON Collaboration), Presentation at LNGS Sci. Comm. Apr. 2015 (2015).
- 2093 [20] M. G. Boulay (For the DarkSide Collaboration), Presentation at New Ideas DM 2017 (2017).
- 2094 [21] R. Agnese et al. (The SuperCDMS Collaboration), *Phys. Rev. D* **95**, 215 (2017).
- 2095 [22] J. Billard, E. Figueroa-Feliciano, and L. Strigari, *Phys. Rev. D* **89**, 023524 (2014).
- 2096 [23] D. Abercrombie et al., *arXiv:1507.00966v1* (2015).
- 2097 [24] C. E. Aalseth et al. (The DarkSide Collaboration), *Eur. Phys. J. Plus* **133**, 131 (2018).
- 2098 [25] M. D'Incecco et al., *IEEE Trans. Nucl. Sci.* **65**, 1005 (2018).
- 2099 [26] M. D'Incecco et al., *IEEE Trans. Nucl. Sci.* **65**, 591 (2018).
- 2100 [27] D. Franco et al., *JCAP* **2016**, 017 (2016).
- 2101 [28] J. Evans et al., *Phys. Rev. D* **95**, 1180 (2017).
- 2102 [29] M. Honda, T. Kajita, K. Kasahara, and S. Midorikawa, *Phys. Rev. D* **83**, 123001 (2011).
- 2103 [30] G. D. Barr, S. Robbins, T. K. Gaisser, and T. Stanev, *Phys. Rev. D* **74**, 323 (2006).
- 2104 [31] R. Tayloe, *JINST* **13**, C04005 (2018).
- 2105 [32] D. Akimov et al. (The COHERENT Collaboration), *Science* **357**, 1123 (2017).
- 2106 [33] H. Cao et al. (The SCENE Collaboration), *Phys. Rev. D* **91**, 092007 (2015).
- 2107 [34] T. Alexander et al. (The SCENE Collaboration), *Phys. Rev. D* **88**, 092006 (2013).
- 2108 [35] P. Agnes et al. (The ARIS Collaboration), *Phys. Rev. D* **97**, 10 (2018).
- 2109 [36] J. Dobson (For the LZ Collaboration), Presentation at DM 2018 (2018).
- 2110 [37] I. Ostrovskiy et al., *IEEE Trans. Nucl. Sci.* **62**, 1825 (2015).
- 2111 [38] S. Cebrián et al. (The NEXT Collaboration), *JINST* **12**, T08003 (2017).
- 2112 [39] J. J. Gómez Cadenas, J. M. Benlloch-Rodríguez, and P. Ferrario, *Spectrochim. Acta B* **118**, 6 (2016).
- 2113 [40] S. Cebrián et al., *JINST* **10**, P05006 (2015).
- 2114 [41] M. G. Boulay (For The DEAP Collaboration), *J. Phys. Conf. Ser.* **375**, 012027 (2012).
- 2115 [42] C. M. Nantais, B. T. Cleveland, and M. G. Boulay, *AIP Conf. Proc.* pp. 185–188 (2013).
- 2116 [43] P. Agnes et al. (The DarkSide Collaboration), *JINST* **11**, P12007 (2016).
- 2117 [44] P. Agnes et al. (The DarkSide collaboration), *JINST* **11**, P03016 (2016).
- 2118 [45] P. Agnes (Université Paris Diderot), Ph.D. thesis, Université Paris Diderot (2016), URL <https://tel.archives-ouvertes.fr/tel-01497505v1>.
- 2119 [46] P. Agnes et al. (The DarkSide Collaboration), *JINST* **12**, P12011 (2017).
- 2120 [47] P. Agnes et al. (The DarkSide Collaboration), *JINST* **12**, P01021 (2017).
- 2121 [48] P. Agnes et al. (The DarkSide Collaboration), *JINST* **12**, P10015 (2017).
- 2122 [49] P. Agnes et al. (The DarkSide Collaboration), *JINST* **12**, T12004 (2017).

- 2124 [50] P. Agnes et al. (The DarkSide Collaboration), *Nucl. Inst. Meth. A* **904**, 23 (2018).
- 2125 [51] W. J. Willis and V. Radeka, *Nucl. Inst. Meth.* **120**, 221 (1974).
- 2126 [52] V. Radeka, *IEEE Trans. Nucl. Sci.* **21**, 51 (1974).
- 2127 [53] V. Radeka and S. Rescia, *Nucl. Inst. Meth. A* **265**, 228 (1988).
- 2128 [54] R. L. Chase, C. de La Taille, S. Rescia, and N. Seguin, *Nucl. Inst. Meth. A* **330**, 228 (1993).
- 2129 [55] R. L. Chase and S. Rescia, *IEEE Trans. Nucl. Sci.* **44**, 1028 (1997).
- 2130 [56] W. Ootani, *Nucl. Inst. Meth. A* **732**, 146 (2013).
- 2131 [57] P. W. Cattaneo et al., *Nucl. Inst. Meth. A* **828**, 191 (2016).
- 2132 [58] I. Ostrovskiy (The University of Alabama), (2012).
- 2133 [59] A. S. Barabash et al., *Nucl. Inst. Meth. A* **868**, 98 (2017).
- 2134 [60] L. Mapelli et al., *CERN EDMS* **1837551** (2017).
- 2135 [61] F. A. Lindemann, *Phil. Mag.* **38**, 173 (1919).
- 2136 [62] H. C. Urey, F. G. Brickwedde, and G. M. Murphy, *Phys. Rev.* **40**, 1 (1932).
- 2137 [63] J. de Boer and R. J. Lunbeck, *Physica* **14**, 520 (1948).
- 2138 [64] J. de Boer, *Physica* **14**, 139 (1948).
- 2139 [65] J. de Boer and A. Michels, *Physica* **6**, 97 (1939).
- 2140 [66] J. Bigeleisen, *J. Chem. Phys.* **34**, 1485 (1961).
- 2141 [67] G. Boato, G. Scoles, and M. E. Vallauri, *Nuovo Cim.* **23**, 1041 (1962).
- 2142 [68] G. Boato, G. Casanova, G. Scoles, and M. E. Vallauri, *Nuovo Cim.* **20**, 87 (1961).
- 2143 [69] G. Boato, G. Scoles, and M. E. Vallauri, *Nuovo Cim.* **14**, 735 (1959).
- 2144 [70] G. Casanova, A. Levi, and N. Terzi, *Physica* **30**, 937 (1964).
- 2145 [71] C. Casanova, R. Fieschi, and N. Terzi, *Nuovo Cim.* **18**, 837 (1960).
- 2146 [72] R. Fieschi and N. Terzi, *Physica* **27**, 453 (1961).
- 2147 [73] J. N. Canongia Lopes, A. A. H. Pádua, L. P. N. Rebelo, and J. Bigeleisen, *J. Chem. Phys.* **118**, 5028 (2003).
- 2148 [74] J. C. G. Calado, F. A. Dias, J. N. C. Lopes, and L. P. N. Rebelo, *J. Phys. Chem. B* **104**, 8735 (2000).
- 2149 [75] W. L. McCabe and E. W. Thiele, *Ind. Eng. Chem.* **17**, 605 (1925).
- 2150 [76] A. J. V. Underwood, *Ind. Eng. Chem.* **41**, 2844 (1949).
- 2151 [77] E. R. Gilliland, *Ind. Eng. Chem.* **32**, 1220 (1940).
- 2152 [78] M. R. Fenske, *Ind. Eng. Chem.* **24**, 482 (1932).
- 2153 [79] Aspen Technology, Inc., *Aspen Plus®* (2015).